NUREG/CR–6849
ERI/NRC-04-201

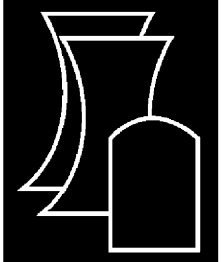

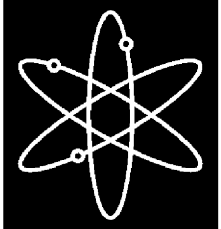

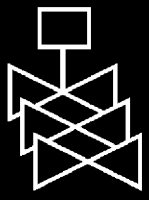

Analysis of In-Vessel Retention and Ex-Vessel Fuel Coolant Interaction for AP1000

Energy Research, Inc.

U.S. Nuclear Regulatory Commission
Office of Nuclear Regulatory Research
Washington, DC 20555-0001

AVAILABILITY OF REFERENCE MATERIALS IN NRC PUBLICATIONS

NRC Reference Material

As of November 1999, you may electronically access NUREG-series publications and other NRC records at NRC's Public Electronic Reading Room at http://www.nrc.gov/reading-rm.html. Publicly released records include, to name a few, NUREG-series publications; *Federal Register* notices; applicant, licensee, and vendor documents and correspondence; NRC correspondence and internal memoranda; bulletins and information notices; inspection and investigative reports; licensee event reports; and Commission papers and their attachments.

NRC publications in the NUREG series, NRC regulations, and *Title 10, Energy*, in the Code of *Federal Regulations* may also be purchased from one of these two sources.

1. The Superintendent of Documents
   U.S. Government Printing Office
   Mail Stop SSOP
   Washington, DC 20402–0001
   Internet: bookstore.gpo.gov
   Telephone: 202-512-1800
   Fax: 202-512-2250
2. The National Technical Information Service
   Springfield, VA 22161–0002
   www.ntis.gov
   1–800–553–6847 or, locally, 703–605–6000

A single copy of each NRC draft report for comment is available free, to the extent of supply, upon written request as follows:

Address: Office of the Chief Information Officer,
Reproduction and Distribution
Services Section
U.S. Nuclear Regulatory Commission
Washington, DC 20555-0001
E-mail: DISTRIBUTION@nrc.gov
Facsimile: 301–415–2289

Some publications in the NUREG series that are posted at NRC's Web site address http://www.nrc.gov/reading-rm/doc-collections/nuregs are updated periodically and may differ from the last printed version. Although references to material found on a Web site bear the date the material was accessed, the material available on the date cited may subsequently be removed from the site.

Non-NRC Reference Material

Documents available from public and special technical libraries include all open literature items, such as books, journal articles, and transactions, *Federal Register* notices, Federal and State legislation, and congressional reports. Such documents as theses, dissertations, foreign reports and translations, and non-NRC conference proceedings may be purchased from their sponsoring organization.

Copies of industry codes and standards used in a substantive manner in the NRC regulatory process are maintained at—

The NRC Technical Library
Two White Flint North
11545 Rockville Pike
Rockville, MD 20852–2738

These standards are available in the library for reference use by the public. Codes and standards are usually copyrighted and may be purchased from the originating organization or, if they are American National Standards, from—

American National Standards Institute
11 West 42nd Street
New York, NY 10036–8002
www.ansi.org
212–642–4900

Legally binding regulatory requirements are stated only in laws; NRC regulations; licenses, including technical specifications; or orders, not in NUREG-series publications. The views expressed in contractor-prepared publications in this series are not necessarily those of the NRC.

The NUREG series comprises (1) technical and administrative reports and books prepared by the staff (NUREG–XXXX) or agency contractors (NUREG/CR–XXXX), (2) proceedings of conferences (NUREG/CP–XXXX), (3) reports resulting from international agreements (NUREG/IA–XXXX), (4) brochures (NUREG/BR–XXXX), and (5) compilations of legal decisions and orders of the Commission and Atomic and Safety Licensing Boards and of Directors' decisions under Section 2.206 of NRC's regulations (NUREG–0750).

NUREG/CR-6849
ERI/NRC 04-201

Analysis of In-Vessel Retention and Ex-Vessel Fuel Coolant Interaction for AP1000

Manuscript Completed: July 2004
Date Published: August 2004

Prepared by
H. Esmaili, M. Khatib-Rahbar

Energy Research, Inc.
P.O. Box 2034
Rockville, MD 20847-2034

S. Basu, NRC Project Manager

Prepared for
Division of Sytems Analysis and Regulatory Effectiveness
Office of Nuclear Regulatory Research
U.S. Nuclear Regulatory Commission
Washington, DC 20555-0001
NRC Job Code Y6696

ABSTRACT

The present study assesses the likelihood and potential location of the reactor pressure vessel lower head failure following low-pressure severe accident scenarios in AP1000, and subsequently, the energetics of ex-vessel fuel coolant interaction. The approach consists of the specification of initial conditions; determination of the mode, the size and the location of lower head failure based on heat transfer analyses; computer simulation of the fuel coolant interaction processes; and finally, an examination of the impact of the uncertainties in the initial conditions and the model parameters on the fuel coolant interaction energetics through a series of sensitivity calculations. The thermal analysis of lower head shows that the lower head failure probability at the side of the vessel due to the focusing effect of the thin stratified metal layer overlying the ceramic pool ranges from ~0.04 to ~0.30, depending on the uncertainties in late phase melt progression and the modeling parameters. On the other hand, the failure of the lower head due to thermal attack at the bottom location is assessed to be highly unlikely. Furthermore, two-dimensional ex-vessel fuel coolant interaction analyses show that the calculated impulse loads (and maximum pressures) for AP1000 remain below those that were estimated for AP600 using similar methods.

TABLE OF CONTENTS

LIST OF FIGURES

LIST OF TABLES

EXECUTIVE SUMMARY

The present study assesses the likelihood and potential location of the RPV lower head failure, following low-pressure severe accident scenarios in AP1000, and subsequently, to assess the energetics of ex-vessel Fuel Coolant Interaction (FCI). The approach used in this study consists of the specification of initial conditions; determination of the mode, the size, and the location of lower head failure; computer simulation of the FCI processes; and finally, an examination of the impact of the uncertainties in the initial conditions as well as the FCI model parameters on the fuel coolant interaction energetics through a series of sensitivity calculations.

The cavity designs in AP600 and AP1000 are similar, but the AP1000 Reactor Pressure Vessel (RPV) lower head is closer to the cavity floor. Given that the initial debris mass, composition, and superheat are the same in AP600 and AP1000, and the vessel failure modes are the same, it is argued in the Westinghouse PRA that the AP600 results can be applied to AP1000. The high impulse loads on the cavity wall in AP600 assessment led to the conclusion that cavity wall integrity could not be assured. Westinghouse asserted that even though the cavity wall was expected to fail, the steel containment integrity would be maintained.

A one-dimensional model is used to study the thermal response of the lower head by assuming two bounding melt configurations. The first melt configuration involves a stratified metallic layer on top of the molten ceramic pool (i.e., melt Configuration I as characterized in the present study), and the second configuration allows for the presence of an additional heavy metal layer below the ceramic pool (i.e., melt Configuration II). The major uncertainties in the initial conditions include the mass of UO_2 relocated to the lower head, the fraction of Zr oxidation, the decay heat in the molten pool, and the mass of steel in the top light metallic layer. These uncertainties are quantified based on the results of various studies for AP600 and the recent analyses for AP1000, using subjective judgment. The uncertainties are propagated through the model using 1000 random samples from the various distributions to arrive at the likelihood of exceeding the critical heat flux, thus resulting in vessel failure. The uncertainty distributions are characterized for melt Configuration I only; however, due to the complex nature of heat transfer processes between the heavy metallic and ceramic layers for Configuration II, the lower head failure potential in the heavy metallic region is assessed based on parametric calculations.

The results of the base case calculations for melt Configuration I show that the heat flux remains below the critical heat flux in the molten oxide pool, but the heat flux in the metal layer could exceed the critical heat flux because of the focusing effect associated with presence of the thin metal layers. For thin metal layers, part of the heat flux from the ceramic layer is focused on a small area on the vessel wall that can exceed the critical heat flux at that location. The thin metal layers are associated with smaller quantities of the molten oxide in the lower plenum following the initial relocation from the core into the lower head. Provided that the volume of the molten ceramic (oxide) pool in the lower plenum is not sufficient to submerge the core support plate, the quantity of steel that could melt and stratify would be small. In the present study, the amount of steel in the top metallic layer is correlated with the mass of UO_2 that relocates into the lower head.

A number of parametric calculations were performed to examine the sensitivity of the in-vessel retention results to the assumed initial conditions. These included the heat transfer correlations in the molten oxide pool, lower probability of low UO_2 mass (thus mitigating the focusing effect), the material properties, and partitioning of the decay heat to the light metallic layer on top of the ceramic melt. The fraction of decay heat in the top metal was assumed to be a function of the Zr oxidation fraction and the time of corium relocation into the lower plenum. The top metal layer decay heat fraction can vary between 0.1 and 0.2. Table E.1 shows the list of the various parametric cases.

Cases 1 through 8 assume no heat generation in the light top metallic layer, while for Cases 1D through 7D, a normal distribution is assumed between the lower bound of 0.1 and the upper bound of 0.2 for the fraction of the decay heat in the top metal layer (the rest of the decay heat is assumed to reside in the ceramic melt layer). The calculated results show that a combination of the focusing effect and the additional power in the light metallic layer can increase the likelihood of lower head failure by a factor of 2 for Case 1D, and 1.5 for Case 2D. However, for Case 3D, there is no significant increase in the conditional failure probability of the lower head. This result is not surprising, because for Cases 3 and 3D, the fraction of upward heat transfer in the molten oxide pool is greater than for Cases 1 and 1D. At some point, increasing the decay heat in the light metallic layer does not necessarily increase the conditional failure probability of the lower head because of the respective reduction in the decay heat in the molten oxide pool (and thus reducing the upward heat flux from the molten oxide

Table E.1 Comparison of lower head conditional failure probabilities (CFP)

Case	Description	Ceramic Layer CFP	Metal Layer CFP
In the Absence of Decay Heat in the Light Metal Layer			
1	Base case	0	0.15
2	DOE heat transfer correlations	0	0.20
3	Heat transfer correlations used in the INEEL study	0	0.30
4	Material properties	0	0.16
5	Reduce probability of low UO_2 mass	0	0.04
6	"Tails" of uncertainty distributions	0	0.16
7	Assumed ±10% uncertainty in CHF correlation	0	0.08-0.25
8	25% increase in heat transfer coefficient (oxide to light metal layer)	0	0.17
Including Decay Heat in the Light Metal Layer			
1D	All other conditions are identical to Case 1	0	0.27
2D	DOE heat transfer correlations	0	0.30
3D	Heat transfer correlations used in the INEEL study	0	0.31
4D	Reduce probability of low UO_2 mass	0	0.07
5D	"Tails" of uncertainty distributions	0	0.30
6D	Assumed ±10% uncertainty in CHF correlation	0	0.20-0.31
7D	25% increase in heat transfer coefficient (oxide to light metal layer)	0	0.29

pool to the top metal layer). In fact, for Case 1D, if the upper bound of the decay heat fraction is increased from 0.2 to 0.9, there is only a modest increase in the calculated conditional failure probability (i.e., from 0.27 to 0.32). The results of the sensitivity calculations show that the failure probability can range from 0.04 to about 0.3 depending on the likelihood that is assigned to the initial melt masses that would involve the relocation of smaller quantities of ceramic material into the lower plenum, and the heat transfer correlations that are used in the calculations.

Three additional sensitivity calculations were also performed as part of the response to the peer reviewer comments. The first sensitivity case involved the assessment of the impact of the tails of the uncertainty distributions on the calculated likelihood of vessel failure (6 and 5D). For the case without decay heat in the light metal layer (Case 6), the failure probability increases from 0.15 (Case 1) to 0.16, and for the case with decay heat in the light metal layer, the failure probability increases from 0.27 (Case 1D) to 0.30 (Case 5D). The next sensitivity case involved the assessment of the impact of the critical heat flux (i.e., ±10% variation in critical heat flux based on the available data) on the calculated likelihood of vessel failure. The uncertainties in the critical heat flux can have a significant effect on the failure probability that can range from 0.08 to 0.25 for the case without decay heat in the light metal layer (Case 7), and from 0.20 to 0.31 for the case with decay heat in the light metal layer (Case 6D). The final sensitivity case involved the assessment of the impact of an arbitrary increase in the heat transfer coefficient between the ceramic pool and the stratified light metallic layer by 25%. The impact of this enhancement in heat transfer coefficient on the calculated likelihood of vessel failure is shown to be minimal. The failure probability increases from 0.15 (Case 1) to about 0.17 (Case 8) for the case without decay heat in the metal layer, and from 0.27 (Case 1D) to 0.29 (Case 7D) for the case with decay heat in the metal layer, respectively. The variations in the failure probabilities for these three cases are within the range of other variations listed in Table E.1; therefore, the overall conclusions regarding the likelihood of in-vessel retention through external cooling of the lower head, remain unchanged.

A number of parametric calculations were performed for melt Configuration II by varying the mass of uranium in the bottom heavy layer, but assuming conservatively that the mass fraction of uranium is 0.4. The parametric calculations were performed for various fractions of uranium in the oxide form. The results of the calculations show that the local heat flux remained below the critical heat flux as based on data for AP1000 Configuration V[1] that were obtained from the recent critical heat flux experiments. However, it should be mentioned that even if the vessel were to fail at the bottom of the lower head, the melt column in the water pool is shorter than the melt column for a side failure of vessel (i.e., melt reaches the cavity floor sooner when the explosion is assumed to be triggered).

[1] Note that "Configuration V" refers to the Westinghouse lower head insulation design, and is not related to the lower head "melt Configurations I and II" terminology as defined in the present report.

Because of the distance of the explosion zone to the cavity wall, the pressures on the cavity wall would be lower than those resulting from a side failure.

Based on the in-vessel retention analysis, the base case for the ex-vessel FCI is assumed to involve a side failure of the vessel involving a metallic pour into the cavity water. For the AP1000 analysis, the entire RPV lower head is modeled based on the insights from the AP600 study by ERI. The impulse loads on the RPV are found to be similar to those on the cavity wall due to the proximity of the explosion zone to both the RPV and the cavity wall.

A number of sensitivity studies were also performed for AP1000. The results of the ex-vessel fuel coolant interaction analyses for AP1000 show that the impulse loads on the cavity wall remain below the calculated loads for AP600. In the AP600 analysis, the base case involved a mostly ceramic melt pour, while in the present AP1000 analysis the base case involves a metallic pour. However, the sensitivity calculations for the most severe case of a deeply flooded cavity in AP1000 clearly show that the previously reported AP600 impulse load predictions are bounding.

FOREWORD

Following a hypothetical core melt accident, molten core materials consisting of metallic components representing cladding (zirconium or Zr) and structural materials (primarily stainless steel) and ceramic components (uranium oxide or UO_2) representing the fuel, will relocate into the lower head of the reactor pressure vessel. The probability of such an event for AP1000, a Westinghouse advanced passive nuclear power plant design, is estimated to be 2.4×10^{-7} per reactor year, which is lower than that for the current generation reactors. Understanding the behavior of a molten core in the lower head will enable the staff to assess the likelihood, location, timing, and size of lower head failure, and to assess the effectiveness of employing the accident management strategy to cool the reactor pressure vessel lower head by external flooding. In the event the lower head failure cannot be prevented, the molten core debris released from the reactor pressure vessel will relocate into the cavity and will interact with the concrete basemat and sidewall. If unmitigated, such interaction has the potential of failing the cavity structure as well as the containment by overpressurization and/or concrete ablation thereby creating a pathway for release of fission products into the environment. Thus, understanding the behavior of a molten core in the cavity, in particular, core-concrete interaction and debris coolability, will enable the staff to assess the effectiveness of employing the accident management strategy to cool the ex-vessel core debris by an overlying water pool.

The present report documents an assessment of the likelihood and potential location of the reactor pressure vessel lower head failure, following low-pressure severe accident scenarios in AP1000. The report also documents an assessment of consequent ex-vessel fuel coolant interaction and dynamic loading of the containment resulting from such interaction. The thermal response of the lower head from relocated core debris was analyzed assuming two bounding melt configurations. The first melt configuration involved a stratified metallic layer on top of the molten ceramic pool, and the second configuration allowed for the presence of an additional heavy metal layer below the ceramic pool. The major uncertainties in the initial conditions included the mass of UO_2 relocated to the lower head, the fraction of Zr oxidation, the decay heat in the molten pool, and the mass of steel in the top light metallic layer. These uncertainties were quantified for the first configuration and propagated through the model to arrive at the likelihood of exceeding the critical heat flux, thus resulting in vessel failure. For the second configuration, parametric calculations were performed since uncertainties could not be quantified with any degree of confidence.

For the first melt configuration, the results show that the heat flux remains below the critical heat flux in the molten oxide pool, but the heat flux in the metal layer could exceed the critical heat flux due to the focusing effect and thus, could result in vessel failure on the side. The results of parametric calculations for the second melt configuration show that the local heat flux at the vessel bottom remained below the critical heat flux making the failure at the bottom much less likely. Even if the vessel were to fail at the bottom of the lower head, the ex-vessel consequence from fuel-coolant interactions (i.e., impulse loading on the cavity wall) will be less than that due to a side failure because the melt mass involved would be lower and the distance from the explosion zone to the cavity wall would be greater. Based on the in-vessel retention analysis and given the likely vessel failure modes for AP1000, the results of the ex-vessel fuel coolant interaction analysis show that the impulse loads on the AP1000 cavity wall are not large enough to challenge containment integrity in a manner that will cause fission product release into the environment.

The assessment documented in this report relied on tests and analysis programs carried out by the Office of Research. These include the recently completed RASPLAV and MASCA Phase I program, the Lower Head Failure (LHF) program completed earlier, and the Melt Coolability and Concrete Interaction (MCCI) program. The MASCA (MAterial SCAling) program and its predecessor RASPLAV program investigated experimentally the chemical interactions of in-vessel molten core with the reactor structural materials, and the effect of such interactions on thermal loading of the lower head. The LHF program investigated the effect of lower head thermal loading on the likelihood, location, timing, and size of the lower head failure. The MCCI program is investigating the effectiveness of an overlying water pool in cooling the ex-vessel core debris thereby arresting ex-vessel core-concrete interaction and consequent failure of the cavity and the containment.

Farouk Eltawila, Director
Division of Systems Analysis and Regulatory Effectiveness

ACKNOWLEDGEMENTS

The authors acknowledge valuable peer review comments provided by Drs. M. L. Corradini (University of Wisconsin-Madison), V. K. Dhir (University of California – Los Angeles) and F. Moody (Consultant, formerly of General Electric Company), on the draft version of this report.

This work was performed under the auspices of U.S. Nuclear Regulatory Commission, Office of Nuclear Regulatory Research, Contract Number NRC-RES-04-02-075.

LIST OF ACRONYMS

CFP	Conditional Failure Probability
CHF	Critical Heat Flux
CMT	Core Makeup Tank
DCH	Direct Containment Heating
DOE	Department of Energy
DVI	Direct Vessel Injection
ERI	Energy Research, Inc.
FCI	Fuel Coolant Interaction
GUI	Graphical User Interface
INEEL	Idaho National Engineering and Environmental Laboratory
IRWST	In-Containment Refueling Water Storage Tank
IVR	In-Vessel Retention
LHS	Latin Hypercube Sampling
LOCA	Loss of Coolant Accident
LWR	Light Water Reactor
NRC	Nuclear Regulatory Commission
NSSS	Nuclear Steam Supply System
PCS	Passive Cooling System
PRA	Probabilistic Risk Assessment
PWR	Pressurized Water Reactor
RAI	Request for Additional Information
RCS	Reactor Coolant System
RPV	Reactor Pressure Vessel

NOMENCLATURE

$A_{h,b}$ Heat transfer area between the heavy metal layer and the vessel, m^2

$A_{h,t}$ Heat transfer area between the heavy metal layer and the lower crust, m^2

$A_{l,b}$ Heat transfer area of between the upper crust of the ceramic pool and the light metallic layer, m^2

$A_{l,t}$ Heat transfer area between the light metallic layer and the reactor internal atmosphere, m^2

$A_{l,w}$ Heat transfer area between the light metallic layer and the rest of the reactor pressure vessel, m^2

$A_{o,b}$ Heat transfer area between the oxide pool and the bottom crust of the ceramic pool, m^2

$A_{o,t}$ Heat transfer area between the oxide pool and the top crust, m^2

$A_{o,w}$ Heat transfer area between the oxide pool and the crust layer adjacent to the vessel wall, m^2

A_s Total surface area of all core internal structures exposed to the molten pool, m^2

$A_{w,i}$ Heat transfer area between the vessel wall and the crust of the oxide pool adjacent to it, m^2

f_{ACT} Fraction of actinides in the melt

f_{FP} Fraction of fission products in the melt

f_{metal} Fraction of metals in the oxide layer

f_{ox_U} Fraction of uranium metal in the oxide layer

$h_{h,b}$ Heat transfer coefficient at the heavy metallic layer-vessel wall juncture, W/m^2-K

$h_{h,t}$ Heat transfer coefficient at the heavy metallic layer-lower oxide crust juncture, W/m^2-K

$h_{l,b}$ Heat transfer coefficient at the light metallic layer-lower oxide crust juncture, W/m^2-K

$h_{l,t}$ Heat transfer coefficient at the top surface of the light metallic layer, W/m^2-K

$h_{l,w}$ Heat transfer coefficient at the light metal layer, vessel wall juncture, W/m^2-K

$h_{o,b}$ Heat transfer coefficient at the oxide pool-lower crust juncture, W/m^2-K

$h_{o,t}$ Heat transfer coefficient at the oxide pool-upper crust juncture, W/m^2-K

$h_{o,w}$ Heat transfer coefficient at the oxide pool-wall crust juncture, W/m^2-K

h_{boil} Coefficient for Nucleate pool boiling Heat transfer, W/m^2-K^3

k_c Thermal conductivity of the crust, W/m-K

k_w Thermal conductivity of the vessel wall, W/m-K

Nu Nusselt number

P_{ACT} Total contribution of actinides to decay heat, W

P_{decay_tot} Total decay heat in the debris, W

Pr Fluid Prandtl number

Q_c''' Volumetric heat generation rate in the oxide crust, W/m^3

Q_h''' Volumetric heat generation rate in the heavy metal layer, W/m^3

Q_l''' Volumetric heat generation rate in the light metal layer, W/m^3

Q_o''' Volumetric heat generation rate in the oxide pool, W/m^3

$q''_{h,b}$ Heat flux from the heavy metal layer to the bottom of the vessel, W/m^2

$q''_{h,t}$ Heat flux from the lower oxide pool crust into the heavy metal layer, W/m^2

$q''_{l,b}$ Heat flux from the top oxide pool crust into the top light metal layer, W/m^2

$q''_{l,t}$ Heat flux from the top light metal layer into the internal atmosphere of the reactor, W/m^2

$q''_{l,w}$ Heat flux from the top light metal layer into the vessel wall, W/m^2

$q''_{o,b}$ Heat flux from the oxide pool into the lower crust, W/m^2

$q''_{o,t}$ Heat flux from the oxide pool into the top crust, W/m^2

$q''_{o,w}$ Heat flux from the oxide pool into the crust adjacent to the vessel wall, W/m^2

$q''_{w,i}$ Heat flux from the oxide pool crust that exists adjacent to the vessel wall into the vessel wall, W/m^2

$q''_{w,o}$ Heat flux from the vessel wall into the cavity water, W/m^2

Ra Rayleigh number

T_b^h Bulk temperature of the heavy metal layer, K

T_b^l Bulk temperature of the light metal layer, K

$T_{\max}^o$ Maximum temperature of the oxide pool, K

$T_{h,t}$ Temperature at the heavy metal layer-bottom crust juncture, K

$T_{l,b}$ Temperature at the light metal layer-lower oxide crust juncture, K

$T_{l,t}$ Temperature at the light metal layer-atmosphere interface, K

T_m^l Melting temperature of the light metal layer, K

T_m^o Melting temperature of the oxide pool, K

T_m^{ss} Melting temperature of stainless steel, K

T_m^v Melting temperature of vessel wall, K

T_s Temperature of the core internal structures of area A_s, K

T_{sat} Saturation temperature of cavity water, K

$T_{w,i}$ Inside vessel wall temperature, K

$T_{w,o}$ Outside vessel wall temperature, K

t_r Time of core release, s

$V_{c,l}$ Volume of the lower oxide crust, m^3

$V_{c,u}$ Volume of the upper oxide crust, m^3

$V_{c,w}$ Volume of the oxide crust that exists adjacent to the vessel wall, m^3

V_h Volume of the heavy metal layer, m^3

V_l Volume of the light metal layer, m^3

V_o Volume of the oxide pool, m^3

Greek Symbols

α Thermal diffusivity

β Thermal expansion coefficient

δ_s Vessel wall thickness, m

δ_c Oxide crust thickness, m (Further indexed by *u*, *l* and *w* for *upper, lower* and *wall*)

ε_t Emissivity at the light metal layer-atmosphere interface

ε_s Emissivity of the core internal structures of area A_s

μ Dynamic viscosity

σ Stefan-Boltzmann constant (5.672×10^{-8} $W/m^2\text{-}K^4$)

ν Kinematic viscosity

Subscripts

b Bottom, Bulk
boil Boiling
c Crust
d Downward
h Heavy metal layer
i Inside
l Light metal layer, liquid
lo Lower
m Melting
o Oxide (ceramic) pool, outside
s Structure
sat Saturation
t Top
u Upper, upward
v Vapor
w Wall

Superscripts

h Heavy metallic layer
l Light metallic layer
o Oxide (ceramic) pool
ss Stainless steel
v Vessel

1. INTRODUCTION

The physical processes involved in the late in-vessel phase of severe accidents in Light Water Reactors (LWRs) are very complex and remain uncertain. Under postulated severe accident conditions, large quantities of molten core material may relocate to the lower plenum of the Reactor Pressure Vessel (RPV) where it interacts with water, lower plenum and RPV structures. The heat transfer from the molten debris causes evaporation of any remaining water and heatup of the lower plenum and vessel structures. If the reactor cavity is flooded before melt relocation into the lower plenum, the vessel wall would be initially cool and the outer vessel temperature would remain close to the cavity water saturation temperature. Nucleate pool boiling of the cavity water is an efficient mechanism for heat removal from the molten debris in the lower plenum.

Provided that adequate heat removal could not be achieved, and if the local heat flux at the vessel wall were to exceed the critical heat flux, vessel failure would be expected.

Following the structural failure of the lower head, the molten core debris will pour into the reactor cavity where the potential for energetic Fuel-Coolant Interaction (FCI) with cavity water exists. This energetic FCI is initiated by transfer of energy from the hot liquid (fuel) to the colder liquid (coolant) during liquid-liquid contact resulting in rapid steam generation that could lead to a high local pressure. The dynamic loads on the cavity wall and the RPV could potentially lead to the failure of the cavity wall and/or subjecting the primary system piping connected to the steam generators and the main steam lines penetrating the containment boundary, to severe mechanical loads that could challenge the containment integrity.

1.1 Background

An assessment of the in-vessel retention (IVR) and ex-vessel fuel coolant interactions for AP600 was performed by Energy Research, Inc. (ERI) in the mid-1990s [1]. In this study, based on time-dependent, two-dimensional thermal analysis of an externally-cooled RPV lower head, various initial conditions that affect ex-vessel FCI behavior and the resulting dynamic loads were estimated. The uncertainties considered in the study included:

- Melt initial conditions at vessel breach,
- Cavity condition at vessel breach,
- Location, mode and size of vessel breach, and
- Containment and primary system pressure at vessel breach.

The melt initial conditions were based on the results of SCDAP/RELAP5 calculations. The Reactor Coolant System (RCS) was assumed depressurized, and the cavity and containment conditions at vessel breach were based on the thermal-hydraulic analysis of a direct vessel injection (DVI) line break using the MELCOR computer code. This study was also subjected to an independent peer review.

Additional IVR analyses were also performed for other accident scenarios in AP600 using both one- and two-dimensional heat transfer models [2].

As far as ex-vessel fuel coolant interactions are concerned, the major parameters that affect the explosion energetic are the water pool subcooling, the lower head failure size and location, and the melt composition and temperature. Due to uncertainties in these parameters, a number of parametric and sensitivity calculations were performed [1] to bound the expected range of dynamic loads on the RPV and the cavity walls.

Since the extent of cavity flooding in AP600 was not known, three scenarios were defined to form the basis of the ex-vessel fuel coolant interaction calculations:

- Scenario I – Low cavity water level and an unsubmerged RPV
- Scenario II – Medium cavity water level and a partially submerged RPV
- Scenario III – High cavity water level and a fully submerged RPV

In the base case calculation for each scenario, the melt composition was ceramic with a representative failure hole size of 0.4 m at a sidewall location (closer to the cavity wall). The FCI analyses documented in Reference [1] used the two-dimensional PM-ALPHA [3]/ESPROSE.m [4] and the one-dimensional TEXAS [5-7] computer codes.

The sensitivity studies considered the following two major categories:

1. *Variability in melt progression (initial conditions)* – these impact the melt temperature, composition, and failure size, as well as uncertainties associated with water pool subcooling.

2. *Variability in fuel coolant interaction modeling* – these include modeling parameters associated with particle breakup during premixing phase and fragmentation rate during the propagation phase.

The results of the calculations are reproduced from Reference [1] and are provided in Table 1.1. It is seen that the melt composition strongly impacted the calculated impulse loads. The metallic melt has a lower thermal energy and density. The water subcooling has the expected effect on the explosion pressures, i.e., higher subcooling leads to lower void fractions. In addition, modeling of the RPV structure within the computational domain can significantly impact the maximum impulse loads on the cavity wall depending on the water depth in the cavity. For the deeply flooded cavity, there is a doubling of the impulse load on the cavity wall and the loads on the RPV are similar to those on the cavity wall due to the proximity of the wall to the explosion zone.

The main conclusions of the AP600 FCI study included [1]:

- Comparison of the calculated impulse loads for different scenarios using the ESPROSE.m code with a typical impulse capacity of 25 kPa-s indicated that these high impulses point to the possibility of localized damage to the cavity wall even though the impulse capacity of the AP600 was not known at the time.

- Impulse loads on the reactor pressure vessel were expected to cause severe vibration of the pressure vessel, connected RCS piping, steam generators, and the main steam lines penetrating the steel containment structure.

It should be noted that given the high impulse load of 670 kPa-s on the lower head, the maximum uplift of the RPV is 55.4 ft [8]. A loading of 644 kPa-s produced less than 5% elongation on the steel containment vessel [8]. However, a discussion of the survivability of the containment penetrations due to excessive impulse loading is not provided in Reference [8].

1.2 Summary of the Westinghouse Assessment for AP600

It is stated on page 19-15 of NUREG-1512 [8] that the AP600 reactor vessel cavity concrete structure has a high dynamic pressure capacity, and the deterministic evaluation of ex-vessel FCIs indicated that the impulse loads from the ex-vessel fuel coolant interactions would fail the reactor cavity floor and wall structures, but the integrity of the embedded steel liner will be maintained. In addition, the containment vessel integrity would not be compromised by the displacement of the RPV. Therefore, the ex-vessel phenomenon associated with ex-vessel fuel coolant interactions would not lead to early containment failure in AP600 as stated on page 19-52 of NUREG-1512 [8].

In the Westinghouse assessment, two vessel failure modes were considered, namely, (1) localized creep rupture of the vessel at the side boundary where the highest heat fluxes occur, and (2) unzipping of the lower head leading to a so-called “hinged” failure mode. The TEXAS computer code was used to assess the resulting steam explosion loads. The initial conditions for the Westinghouse assessment reproduced from Reference [8] are listed in Table 1.2. The major difference between the conditions in Westinghouse and ERI assessment is that the melt composition in the Westinghouse assessment was metallic, whereas in the ERI assessment, the base case melt composition was ceramic even though a metallic pour was also considered as a sensitivity calculation.

The results of the Westinghouse calculations are shown in Table 1.3. Noting the high pressure of about 170 MPa and an assumed pulse duration of 6 msec [8], Westinghouse calculated that the containment vessel would be less than 20% of its ultimate strain capacity, and thus can withstand the peak loading from the hinged vessel failure mode. In addition, using the same peak pressure but an assumed pulse duration of 4 msec, the maximum uplift of the RPV itself would be about 22 feet and since the refueling canal is about 28 feet high, the RPV would remain in the refueling canal, and therefore, cannot directly challenge the steel containment integrity.

1.3 Applicability of AP600 Results to AP1000

The cavity design in AP600 and AP1000 are similar as discussed in the AP1000 PRA [9], but the AP1000 vessel lower head is closer to the cavity floor. Given that the initial debris mass, composition, and superheat are the same in AP600 and AP1000, and the vessel failure modes are the same, it is argued in Reference [9] that the AP600 results can be applied to AP1000.

The high impulse loads on the cavity wall in AP600 assessment (i.e., as shown in References [1] and [8]), led to the conclusion that cavity wall integrity could not be assured. Westinghouse asserted that even though the cavity wall was expected to fail, the steel containment integrity would be maintained [8].

Table 1.1 Summary of the ERI ex-vessel fuel coolant interaction calculation for AP600

Description of Calculations	Maximum Impulse Load (kPa-s)		
	ESPROSE.m		TEXAS
Scenario I (unsubmerged RPV)	Cavity Wall	RPV	Cavity Wall
Base case, saturated pool	85	-	-
Subcooled pool	160	-	-
Scenario II (partially submerged RPV)	Cavity Wall	RPV	Cavity Wall
Base case, saturated Pool	150	-	205
Melt superheat	147	-	215
Subcooled pool	300	-	335
Metallic melt	27 (128[a])	-	153
Hole diameter of 0.2 m	68	-	-
Hole diameter of 0.8 m	383[b]	-	644
Impact of RPV lower head	190	192	-
Dp=0.1 m, maximum fragmentation rate = 4 kg/s	15	-	-
Dp=0.1 m, maximum fragmentation rate = 400 kg/s	86	-	-
Fragmentation constant (increase to 0.0125)	-	-	457
Scenario III (fully submerged RPV)	Cavity Wall	RPV	Cavity Wall
Base case, subcooled water	300	-	-
Saturated pool, RPV modeled	288	320	-
Subcooled pool, RPV modeled	625	670	-

[a] with a water pool subcooling of 20K and initial melt temperature of 3100K
[b] calculation failed after 3 ms due to numerical problems

Table 1.2 Input parameters for Westinghouse TEXAS calculations [8]

Input Parameter	Hinged Mode	Localized	Sensitivity
Melt Composition	Steel	Steel	Steel
Melt Density (kg/m^3)	7800	7800	7800
Melt Temperature (°K)	1890	1890	1910
Melt Superheat (°K)	80	80	100
Jet Diameter (m)	0.068	0.060	0.060
Number of Jets	236	1	1
Jet Velocity (m/s)	2.26	0.17	0.17
Melt Flow Rate (kg/s)	15,100	3.8	3.8
Water Pool Depth* (m)	3.89 0.46	3.89 0.46	3.89 0.46
Nominal Pool Area (m^2)	20	2.5	5.0
Water Temperature (°K)	342	342	385
Nominal Subcooling (°K)	40	40	0
System Pressure** (MPa)	0.17	0.17	0.17

* Deep pool considered for bottom triggering, shallow pool for side triggering.
** Full depressurization of RPV to containment pressure is assumed.

Table 1.3 Peak impulse and pressure from Westinghouse assessment of AP600 ex-vessel fuel coolant interactions [8]

Calculation Case	Impulse (kPa-s)*	Pressure (MPa)*
Base Case (Hinged Failure)	490 (66)	170 (30)
Base Case (Localized Failure)	2.1 (negligible)	0.6 (0.16)
Sensitivity 1 (Melt Superheat)	2.2 (negligible)	N/A
Sensitivity 2 (Nominal Pool Area)	1.5 (negligible)	N/A
Sensitivity 3 (Breakup Model)	2.1 (negligible)	N/A
Sensitivity 4 (Water Temperature)	2.6 (negligible)	N/A

* Numbers in parentheses refer to cavity wall loading; numbers without the parentheses refer to floor loading.

Therefore, given the significance of the RPV lower head structure that is included in the two-dimensional ESPROSE.m calculation for the case of deeply flooded cavity, and the fact that the AP1000 lower head is closer to the cavity floor than the AP600, it is reasonable to perform ex-vessel fuel coolant interactions for this case only. The deeply flooded cavity tends to increase the impulse loads due to lack of the mitigating effect of explosion venting for shallow pools.

1.4 Scope and Objectives

The present study is intended to assess the likelihood and potential location of the RPV lower head failure, following low-pressure severe accident scenarios in AP1000, and subsequently, to assess the energetics of ex-vessel FCIs. The assessment of phenomenological processes governing melt water interactions under high pressure melt ejection conditions, is beyond the scope of this work. The approach used in this study consists of the specification of initial conditions; determination of the mode, the size and the location of lower head failure using detailed analyses; computer simulation of the FCI processes; and finally, an examination of the impact of the uncertainties in the initial conditions and the FCI model parameters on the fuel coolant interaction energetics through a series of sensitivity calculations.

A description of the mathematical model for the in-vessel retention analysis is provided in Section 2. The initial conditions in the lower plenum are specified in Section 3. Section 4 presents the results of in-vessel retention analyses using the mathematical model of Section 2, and the conditions of Section 3. Section 5 provides the initial conditions for the ex-vessel fuel coolant interactions analyses. The results of the ex-vessel fuel coolant interaction calculations are discussed in Section 6. The conclusions of this study are presented in Section 7. Appendix A documents the thermophysical properties of the core debris metallic and ceramic layers. Appendix B lists the peer review comments and the ERI responses to these comments. The ERI responses to additional peer review comments are documented in Appendix C. The Users' Manual for the ERI IVR computer program is included in Appendix D.

2. ANALYSIS OF IN-VESSEL RETENTION

The core debris attack on the RPV lower head and the retention of molten core debris inside RPV lower head through external cooling by cavity water has been the subject of numerous numerical and experimental investigations as exemplified by References [1-2] and [10-23], which include one-, and two-dimensional calculations, measurements of natural convection heat transfer in simulated molten pool configurations, and measurements of critical heat flux on the external surface of the RPV lower head.

In one of the earliest studies, a one-dimensional model was proposed in Reference [12] to study the thermal response of the RPV lower head following core relocation to the lower plenum. The model allowed for the spherical geometry of the lower head with convective heat transfer in the molten pool. A similar one-dimensional model was developed in Reference [2] to calculate a best estimate heat transfer coefficient for use in the MELCOR parametric model. The capability of the external cooling of the RPV lower head to prevent failure considering the presence of the RPV insulation was studied in Reference [13]. The analysis of the thermal response of the lower head was very simple assuming a partitioning of the heat transfer in the molten ceramic pool and one-dimensional conduction in the vessel wall. The focus of the analysis [13] was to assess the water inflow through the insulation and the two-phase heat removal in the gap between the insulation and the vessel wall.

The mathematical models used for the thermal response of the lower head have included both one-dimensional [2, 12, 18, 19] and two-dimensional models [1, 24]. A comparison of the one-dimensional and two-dimensional models in Reference [2] showed that a one-dimensional heat conduction model of the lower head performed adequately and the second order effects using a two-dimensional model were found to be negligible [2] considering the uncertainties associated with the late phase in-vessel melt progression.

The study of the in-vessel retention under externally cooled conditions requires closure relations for heat transfer in the molten ceramic and metallic regions. Reference [25] provides a detailed review of the heat transfer correlations for volumetrically heated pools. This review [25] includes experimental and numerical studies that have been reported in the literature for flat surfaces and curved configurations. A summary of the various heat transfer correlations for the ceramic pool and the stratified light molten metallic layer is also provided in References [18-19]. In the present study, references to these heat transfer correlations have been made where appropriate.

The main objective of the present study is to use a simple mechanistic model based on the existing constitutive relations, originally developed for AP600 [1-2], and a synthesis of severe core damage phenomenology (Section 3), to arrive at a likelihood of vessel failure for AP1000 (Section 4). Furthermore, the present analysis is intended to provide the necessary initial conditions (Section 5) as related to the RPV failure location, and the melt pour condition (e.g., temperature, composition, pour size, etc.) for subsequent assessment of FCI energetics (Section 6).

The technical basis and the mathematical model for analysis of the lower head thermal behavior under severe accident conditions, is presented in the present section. This includes a comparison of the model prediction to the results published in References [18] and [19] for AP600, and Reference [9] for AP1000.

2.1 Mathematical Model

The mathematical model that is used to assess the thermal response of the AP1000 lower head is based on the modifications to the one- and two-dimensional models that were formulated by Energy Research, Inc. (ERI) for AP600 as documented in References [1] and [2]. The model is based on a conceptual representation of two melt configurations shown in Figure 2.1. The melt configuration I assumes a two-layer melt pool with a light metallic layer of Fe-Zr on top of a ceramic pool of UO_2-ZrO_2-M_xO_y as shown in Figure 2.1a. On the other hand, the melt configuration II assumes a stratified molten pool consisting of a dense metallic bottom layer of Zr-U-Fe (in the bottom), a ceramic layer of UO_2-ZrO_2-M_xO_y (in the middle), and a light metallic layer of Fe-Zr (on top) as shown in Figure 2.1b. The ceramic layer does not include metals, and the top metallic layer is assumed to contain essentially no uranium metal. It is recognized that other configurations of the molten pool can be also envisioned [19]; however, in terms of the potential implications on the lower head integrity, the present three-layer configuration is considered to be adequate.

The governing equations for the thermal response of the various melt pool layers shown in Figure 2.1 are presented in the following subsections.

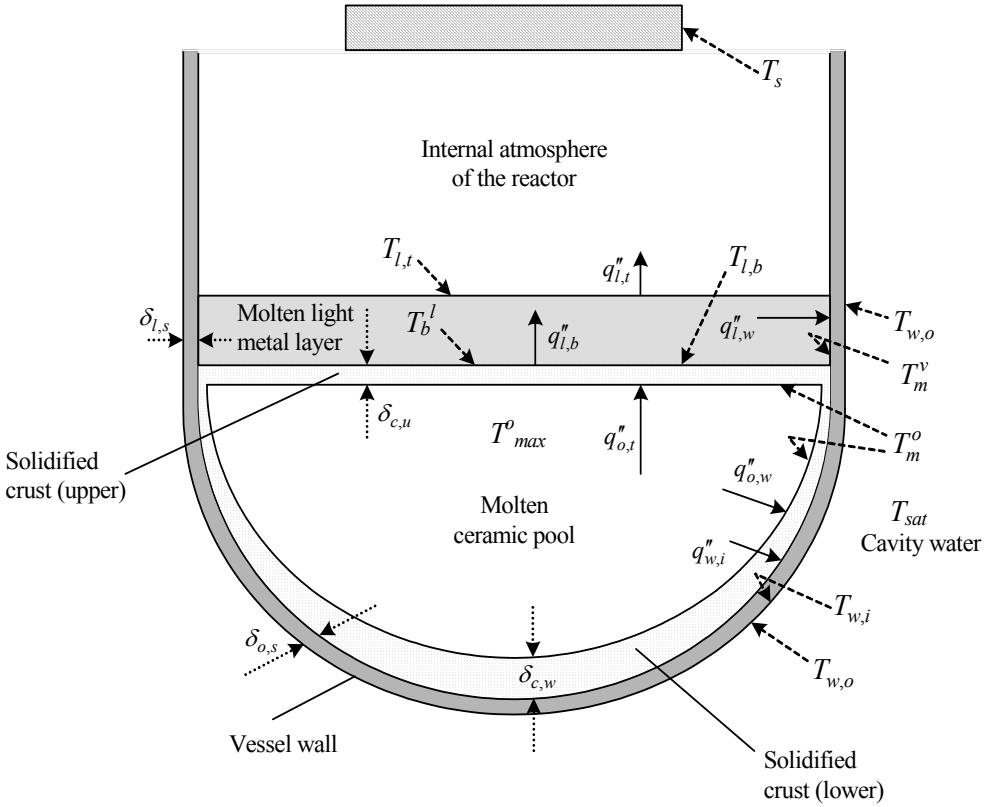

Figure 2.1a Schematic of the melt pool configuration I in the lower head (two layers)

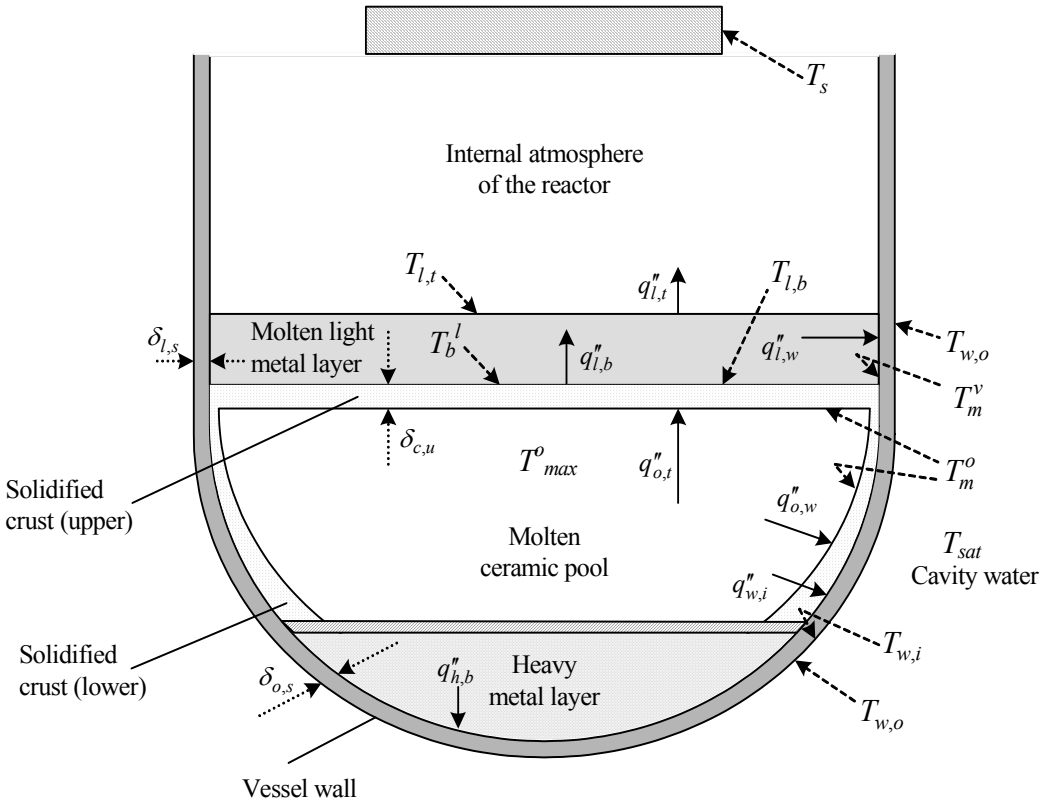

Figure 2.1b Schematic of the melt pool configuration II in the lower head (three layers)

2.1.1 Governing Equations

The conservation of energy equation can be written for each layer subject to the following limitations:

1. The heat generation in the vessel wall is negligible;
2. The radiation heat transfer from the light metal layer top surface is not sufficient to form a crust; and
3. The potential impacts of materials interactions (i.e., heat of mixing and autocatalytic effects) are not considered.

Top Light Metal Layer

$$Q_l'''V_l + q_{l,b}''A_{l,b} = q_{l,t}''A_{l,t} + q_{l,w}''A_{l,w} \quad (2.1)$$

Middle Ceramic (Oxide) Pool

$$Q_o'''V_o = q_{o,t}''A_{o,t} + q_{o,w}''A_{o,w} + q_{o,b}''A_{o,b} \quad (2.2)$$

$$q_{l,b}''A_{l,b} = Q_c'''V_{c,u} + q_{o,t}''A_{o,t} \quad (2.3)$$

$$q_{w,i}''A_{w,i} = q_{o,w}''A_{o,w} + Q_c'''V_{c,w} \quad (2.4)$$

$$q_{h,t}''A_{h,t} = q_{o,b}''A_{o,b} + Q_c'''V_{c,l} \quad (2.5)$$

Bottom Heavy Metal Layer

$$Q_h'''V_h + q_{h,t}''A_{h,t} = q_{h,b}''A_{h,b} \quad (2.6)$$

Additional expressions for heat fluxes in each region in terms of the corresponding temperature differences and the heat transfer coefficients that are based on experimental data are listed in Section 2.1.2.

2.1.2 Heat Transfer in Molten Layers

2.1.2.1 Light Metallic Layer

The upper surface heat flux from the light metal layer (on top of the ceramic layer) can be calculated as:

$$q_{l,t}'' = h_{l,t}(T_b^l - T_{l,t}) \quad (2.7)$$

where $h_{l,t}$ is the heat transfer coefficient from the metal pool to the upper surface, T_b^l is the metal pool bulk temperature, and $T_{l,t}$ is the temperature of the upper surface of the light metallic layer.

The heat loss from the top surface of the light metallic layer, by radiation, to the other structures in the reactor pressure vessel is approximated by the following equation:

$$q_{l,t}'' = \frac{\sigma\left[T_{l,t}{}^4 - T_s{}^4\right]}{\left[\frac{1}{\varepsilon_t} + \frac{1-\varepsilon_s}{\varepsilon_s}\frac{A_{l,t}}{A_s}\right]} \quad (2.8)$$

where T_s is the temperature of the other structures, A_s is the surface area of the other structures, ε_t is the emissivity of the upper surface of the metallic layer and ε_s is the emissivity of the other structures. In the present formulation, it is assumed that the temperature of the other structures is known (e.g., 950K).

The heat flux from the light metallic layer to the vessel wall can be expressed as:

$$q_{l,w}'' = h_{l,w}\left(T_b^i - T_m^v\right) \quad (2.9)$$

where $h_{l,w}$ is the heat transfer coefficient at the metal layer–vessel wall interface, and T_m^v is the melting temperature of the vessel wall. The vessel wall inside temperature is at its melting temperature. The high heat flux from the metal layer to the lower head leads to the melting and thinning of the RPV lower head wall.

The heat flux through the sidewall can be rewritten as:

$$q_{l,w}'' = \frac{k_w}{\delta_{l,s}}\left(T_m^v - T_{w,o}\right) \quad (2.10)$$

where $\delta_{l,s}$ is the thickness of the vessel wall in the top metal layer. Since there is no heat generation in the vessel wall, heat flux to the cavity water from the vessel wall is the same as $q_{l,w}''$:

$$q_{l,w}'' = h_{boil}(T_{w,o} - T_{sat}) = C_{boil}(T_{w,o} - T_{sat})^3 \quad (2.11)$$

where h_{boil} is the Rohsenow's nucleate pool boiling heat transfer coefficient [26], and C_{boil} is the nucleate boiling coefficient that is dependent on the properties of cavity water (see Section 2.1.3).

The heat flux from the top oxide crust to the light metallic layer $q_{l,b}''$ can be estimated using:

$$q_{l,b}'' = h_{l,b}\left(T_{l,b} - T_b^l\right) \quad (2.12)$$

where $h_{l,b}$ is the heat transfer coefficient from the metal layer to its bottom surface that is in contact with the upper crust in the ceramic (oxide) pool.

2.1.2.2 Ceramic Layer

The heat flux from the ceramic pool to the surrounding crust that is in contact with the lower head can be written as:

$$q''_{o,w} = h_{o,w}\left(T^o_{\max} - T^o_m\right) \tag{2.13}$$

where $T^o_{\max}$ is the molten ceramic (oxide) pool maximum temperature, T^o_m is the melting temperature of the ceramic pool, and $h_{o,w}$ is the heat transfer coefficient from the molten pool to the crust interface which is at the oxide pool melting temperature. Considering a uniform volumetric heat generation rate in the ceramic crust, the heat flux at the inner and the outer boundaries of the ceramic crust can be expressed as:

$$q''_{o,w} = \frac{k_c}{\delta_{c,w}}\left(T^o_m - T_{w,i}\right) - \frac{Q'''_c \delta_{c,w}}{2} \tag{2.14}$$

$$q''_{w,i} = \frac{k_c}{\delta_{c,w}}\left(T^o_m - T_{w,i}\right) - \frac{Q'''_c \delta_{c,w}}{2} \tag{2.15}$$

Since it is assumed that the heat generation in the vessel wall can be neglected, the heat flux by conduction through the lower head can be expressed by:

$$q''_{w,i} = \frac{k_s}{\delta_{o,s}}\left(T_{w,i} - T_{w,o}\right) \tag{2.16}$$

where $\delta_{o,s}$ is the thickness of the vessel wall in contact with the oxide (ceramic pool) layer.

The heat flux from the vessel wall into the reactor cavity water, $q''_{w,o}$, can be expressed by the following nucleate boiling relationship (See Equation 2.11):

$$q''_{w,i} = q''_{w,o} = C_{boil}\left(T_{w,o} - T_{sat}\right)^3 \tag{2.17}$$

Equations (2.13) through (2.17) involve five equations in five unknowns. The unknown variables are the heat fluxes ($q''_{w,o}$ and $q''_{w,i}$), the inner wall temperature ($T_{w,i}$), the outer wall temperature ($T_{w,o}$), and the crust thickness ($\delta_{c,w}$). Note that if the inner wall temperature is calculated to be higher than the melting temperature of the vessel wall, then the inner surface of the lower head is ablating (inner surface temperature corresponds to the melting temperature of the RPV), and the ablating thickness of the lower head is calculated.

The heat flux to the light metal layer through the upper ceramic crust is estimated using:

$$q''_{o,t} = h_{o,t}\left(T^o_{\max} - T^o_m\right) \tag{2.18}$$

$$q''_{o,t} = \frac{k_c}{\delta_{c,u}}\left(T^o_m - T^l_b\right) - \frac{Q'''_c \delta_{c,u}}{2} \tag{2.19}$$

$$q''_{l,b} = \frac{k_c}{\delta_{c,u}}\left(T^o_m - T^l_b\right) - \frac{Q'''_c \delta_{c,u}}{2} \tag{2.20}$$

Similarly, the heat flux through the lower ceramic crust is estimated using:

$$q''_{o,b} = h_{o,b}\left(T^o_{\max} - T^o_m\right) \tag{2.21}$$

$$q''_{o,b} = \frac{k_c}{\delta_{c,l}}\left(T^o_m - T_{h,t}\right) - \frac{Q'''_c \delta_{c,l}}{2} \tag{2.22}$$

$$q''_{h,t} = \frac{k_c}{\delta_{c,l}}\left(T^o_m - T_{h,t}\right) - \frac{Q'''_c \delta_{c,l}}{2} \tag{2.23}$$

2.1.2.3 Heavy Metallic Layer

The heat flux characteristics in the heavy metallic layer are complicated. The top surface of the heavy metallic layer is hot because it is in contact with the molten ceramic pool, and the bottom surface of the heavy metallic layer is cool due to nucleate boiling on the outside surface of the lower head (i.e., it is essentially at the constant saturation temperature of the cavity water, provided that the heat flux at the outside surface does not exceed the critical heat flux). In this melt configuration, the temperature gradient is governed by the magnitude of the internal heat generation, the temperature of the top boundary adjacent to the ceramic layer (since the outside boundary is expected to be cool due to external cooling), and the extent of convective motion that could impact the degree of thermal stratification that is expected to develop. The denser cooler fluid will sink to the bottom of the layer, and in the absence of significant natural convection, the

heat transfer in this stratified configuration is dominated by conduction of heat through the layer. Note that in the limit of zero internal heat generation in the heavy metallic layer, the heat from the overlying oxide pool is simply conducted through the bottom metallic layer, into the vessel wall and the cavity water.

The presence of volumetric heating in the heavy metallic layer can further complicate the heat transfer process. To envision the thermal response, consider a simplified slab geometry with internal heat generation, maintained at a higher temperature on the top surface, and lower temperature at the bottom surface. For this case, the maximum temperature occurs at a distance from the top surface inside the slab. In the limit, the location of the maximum temperature can be at the hot surface where the heat flux is zero. Under these conditions, the hot surface is effectively insulated and the heat generated in the layer would have to be transferred to the cold surface. If the maximum temperature is inside the slab, then the heat is transferred away from the layer to both the top hot surface and the bottom cool surface. Furthermore, under the conditions of the present melt configuration, the heat flux in the bottom metal layer and the top two layers are coupled and it is more difficult to analyze. However, it is not necessary to consider this complicated heat transfer problem to assess the heat transfer from the bottom metal layer to the vessel wall. In addition, it is noted that an attempt was not made in the present analysis to establish the phase diagram for the heavy metallic layer.

It is conservatively assumed in the analysis for the melt configuration II shown in Figure 2.1b that:

a. The heat transfer to the vessel wall involves the entire decay heat in the heavy metallic layer, and

b. The heat transfer at the interface from the heavy metallic layer to the ceramic layer is zero (i.e., an insulated top surface).

Therefore, using Equation (2.6), the heat flux to the bottom surface of the heavy metallic layer is estimated as follows:

$$q''_{h,b} = Q'''_h V_h / A_{h,b} \tag{2.24}$$

Furthermore, the heat flux in the vessel wall is given by:

$$q''_{h,b} = \frac{k_w}{\delta_{h,s}}\left(T_{w,i} - T_{w,o}\right) \tag{2.25}$$

where $\delta_{h,s}$ is the thickness of the vessel wall adjacent to the heavy metal layer.

During the calculations, if the inner wall temperature, $T_{w,i}$, exceeds the melting temperature of the vessel wall, the inner wall temperature in that location is set equal to the melting temperature; instead, the thickness of the melted vessel wall in that location is calculated.

Finally, the nucleate boiling heat flux from the vessel wall to the cavity water is given by (See Equation 2.11):

$$q''_{h,b} = C_{boil}\left(T_{w,o} - T_{sat}\right)^3 \tag{2.26}$$

2.1.3 Boiling Heat Transfer Coefficients

The nucleate pool boiling heat transfer coefficient h_{boil} uses Rohsenow's correlation [26]:

$$Nu = \frac{1}{C_{sf}{}^3}\left(\frac{c_{p,l}\Delta T_{sat}}{h_{fg}\,\mathrm{Pr}_l}\right)^2 \tag{2.27}$$

where $c_{p,l}$ is the water specific heat at constant pressure, h_{fg} is the heat of vaporization for water, Pr_l is the saturated liquid Prandtl number, k_l is the thermal conductivity of saturated liquid, C_{sf} is an empirical constant and ΔT_{sat} is the temperature difference between the surface and saturation temperature of water. All the fluid properties in Equation (2.27) are evaluated at the saturation temperature of water. The constant C_{sf} depends on the surface roughness and wetability, and is assigned a value of 0.013 [1], and the boiling coefficient (Equation (2.26)) is defined by the following relation:

$$C_{boil} = \left(\frac{g[\rho_l - \rho_v]}{\sigma_l}\right)^{\frac{1}{2}}\left(\frac{c_{p,l}}{h_{fg}C_{sf}\,\mathrm{Pr}_l}\right)^3\left(\mu_l h_{fg}\right) \tag{2.28}$$

where g is the gravitational acceleration, ρ_l is the density of the saturated liquid and ρ_v is the density of the saturated vapor, σ_l is the liquid surface tension, and μ_l is the liquid viscosity. There is no need to consider the variations in C_{sf} because the final results are not sensitive to this value. As long as the surface is in the nucleate boiling regime, the surface temperature remains close to the saturation temperature of water.

Empirical natural convection heat transfer correlations are listed in Table 2.1. A distinction should be made between the maximum temperature and the bulk temperature in terms of the definition of the heat transfer correlations. For the molten ceramic pool, the Grashof number is based on the maximum temperature as defined by Mayinger; however, the Nusselt number correlations in the literature are based on Rayleigh number (based on internal heat generation). In the present analysis, the energy balance in the molten ceramic pool yields the molten ceramic pool superheat. Since the ceramic pool is bounded by upper and lower crusts, only the molten pool superheat is used to calculate the heat transfer to the pool boundaries (the melt superheat is based on the maximum pool temperature because the ceramic pool is bounded by a crust at the ceramic pool melting temperature). In addition, without any loss of generality, the heat transfer correlations (based on internal Rayleigh number) along with the heat generation in the pool can be used directly to calculate the heat transfer partitioning to the lower and upper surfaces of the molten ceramic pool. For the upper steel layer, the heat transfer correlations are based on the bulk temperature. An energy balance in the metal layer yields the bulk temperature that is used to calculate the heat transfer to the top/bottom surfaces of the metal layer and to the vessel lower head. Table 2.1 also provides the heat transfer correlations used in the Department of Energy (DOE) [18] and the Idaho National Engineering and Environmental Laboratory (INEEL) [19] studies. The ranges of applicability of the correlations listed in Table 2.1 are given in Table 2.2. It should be noted that for the present study, the angular variation of heat transfer coefficient in the molten ceramic pool as proposed in Reference [18] has been used (also note that the angular variation of heat transfer coefficient as developed by Park and Dhir [27] was used in the original ERI model [1-2]. This relationship, together with that of Asfia and Dhir [17], remain optionally available in the ERI IVR code module for sensitivity calculations as described in Appendix D).

2.1.4 Critical Heat Flux Correlation

The critical heat flux correlation is given as [18]:

$$q''_{CHF} = A_{CHF} + B_{CHF}\theta + C_{CHF}\theta^2 + D_{CHF}\theta^3 + E_{CHF}\theta^4 \quad (2.29)$$

where the coefficients A through E are based on experimental results (W/m^2), and θ is the angle in degrees. The critical heat flux coefficients are listed in Table 2.3.

Note that since the coefficients for Westinghouse lower head insulation design Configuration V of AP1000 were not available at the time the present analysis were performed, following the statements in Reference [9] based on the knowledge of the experimental data for Configuration V, it was assumed that the CHF was higher by a factor of 1.44 as compared to Westinghouse lower head insulation design Configuration III for which the correlation and data were available.

Following the peer review of the present report, CHF data for configuration V became available [28]. A comparison of the CHF for Configuration V used in the present study (shown as the solid line) and the reported data [28] is displayed in Figure 2.2 (the dashed lines represent ±10% variation from the solid line). The data are for 3" baffle (M3), 6" baffle (M6), and the 6" to 3" transition baffle (M63). It is clear that the CHF is considerably increased over the entire surface of the lower head; however, the enhancement of the critical heat flux in the uppermost location is less than that at the lower angular position. Most notably, the CHF for higher angular position does not consistently increase, and Reference [28] maintains that "under representative AP1000 exit geometry (at the RPV nozzle gallery), the natural circulation flow is dominantly subcooled, and is modulated by periodic flashing, and frictional phenomena at the exit." In the present analysis, sensitivity calculations are performed to examine the potential impact of uncertainties in the critical heat flux even though the experimental uncertainties are not reported in Reference [28].

2.1.5 Solution Method

The system of Equations (2.1) through (2.29) is solved using a non-linear Newton-Raphson method. In order to account for temperature dependence of the viscosity, the solution involves two passes. In the first pass, the layer temperature is set to its melting temperature, and the viscosity is evaluated at the melting temperature. This provides an estimate of the viscosity, and intermediate values for the heat transfer correlations. Once the heat transfer correlations are calculated, the temperature of each layer can be calculated. In the second pass, the viscosity is evaluated at the new temperatures from the first pass, and the process is repeated.

Table 2.1 Heat transfer correlations used in ERI, DOE and INEEL models

Model		Top surface	Bottom surface	Side wall	Angular variation
ERI [1-2]	**Metallic layer**	Globe-Dropkin [29] $Nu_l = 0.069 Ra_l^{0.333}\,\mathrm{Pr}_l^{0.074}$	Globe-Dropkin [29] $Nu_l = 0.069 Ra_l^{0.333}\,\mathrm{Pr}_l^{0.074}$	Churchill-Chu [30] $Nu_{l,w} = \left[0.825 + \left(\frac{0.387 Ra_l^{1/6}}{\left[1+(0.492/\mathrm{Pr}_l)^{9/16}\right]^{8/27}}\right)\right]^2$	
	Ceramic pool	Kulacki-Emara [31] $Nu_u = 0.345\left(Ra_{q,u}\right)^{0.226}$	Mayinger [24] $Nu_d = 0.55\left(Ra_{q,d}\right)^{0.2}$		Park and Dhir [27] $h_d(\theta) = \bar{h}_d\left(b_1 \sin^2\theta + b_2\right)$ $b_1 = \frac{9.12(1-\cos\theta_0)}{8-9\cos\theta_0+\cos 3\theta_0}$ $b_2 = 0.24$
DOE [18]	**Metallic layer**	Globe-Dropkin "Specialized" $Nu = 0.15 Ra^{1/3}$	Globe-Dropkin "Specialized" $Nu = 0.15 Ra^{1/3}$	Churchill-Chu $Nu = 0.076 Ra^{1/3}$	
	Ceramic pool	Mini-ACOPO[2] [32] $Nu_u = 0.345 Ra^{0.233}$	Mini-ACOPO $Nu_d = 0.0038 Ra^{0.35}\left(\frac{H}{R}\right)^{0.25}$		Mini-ACOPO $\frac{Nu_d}{\overline{Nu}_d} = 0.1 + 1.08\left(\frac{\theta}{\theta_{tot}}\right) - 4.5\left(\frac{\theta}{\theta_{tot}}\right)^2 + 8.6\left(\frac{\theta}{\theta_{tot}}\right)^3$ for $0.1 \le \left(\frac{\theta}{\theta_{tot}}\right) \le 0.6$ and $\frac{Nu_d}{\overline{Nu}_d} = 0.41 + 0.35\left(\frac{\theta}{\theta_{tot}}\right) + \left(\frac{\theta}{\theta_{tot}}\right)^2$ for $0.6 \le \left(\frac{\theta}{\theta_{tot}}\right) \le 1.0$
INEEL [19]	**Metallic layer**	Globe-Dropkin $Nu_l = 0.069 Ra_l^{0.333}\,\mathrm{Pr}_l^{0.074}$	Globe-Dropkin $Nu_l = 0.069 Ra_l^{0.333}\,\mathrm{Pr}_l^{0.074}$	Churchill-Chu $Nu_{l,w} = \left[0.825 + \left(\frac{0.387 Ra_l^{1/6}}{\left[1+(0.492/\mathrm{Pr}_l)^{9/16}\right]^{8/27}}\right)\right]^2$	
	Ceramic pool	ACOPO[2] $Nu_u = 2.4415 Ra'^{0.1772}_p$	ACOPO $Nu_d = 0.1857 Ra'^{0.2304}_p\left(\frac{H}{R}\right)^{0.25}$		Mini-ACOPO (Same as the DOE approach)

[2] Mini-ACOPO was a 1/8th scale facility; while APOCO was a 1/2 scale facility [32]

Notations for Table 2.1

Mayinger correlation [24]:

$Nu_d = \frac{\bar{h}_d R_1}{k_o}$	The surface-averaged Nusselt number
R_1	Inner radius of the lower head, m
ΔT	The difference between the maximum pool temperature and the melting temperature, K
$Ra_{q,d} = \frac{g\beta_o Q_o''' R_1^5}{\alpha_o \nu_o k_o}$	Rayleigh number based on the internal heat generation for steady state conditions

Kulacki-Emara correlation [31]:

H_o	Maximum depth of the ceramic molten pool, m
$Nu_u = \frac{h_u H_o}{k_o}$	Nusselt number
$Ra_{q,u} = \frac{g\beta_o Q_o''' H_o^5}{\alpha_o \nu_o k_o}$	Rayleigh number based on the internal heat generation for steady state conditions

Churchill-Chu correlation [30]:

T_b	Bulk temperature of the molten metal pool
T_w	Wall temperature
H	Height of the molten metal pool
$Ra_l = \left[\frac{g\beta}{\alpha\nu} H^3 (T_b - T_w)\right]_l$	Rayleigh number = $Gr \bullet \Pr = \frac{g\beta H^3 \Delta T}{\alpha\nu}$
g	Gravitational acceleration, 9.81 m/s^2
H	Height of the metallic layer, m
Gr	Grashof number = $\frac{g\beta H^3 \Delta T}{\nu}$
Pr	Prandtl number = $\frac{\nu}{\alpha}$

Notations for Table 2.1(Continued)

ACOPO correlations [18]:

$Ra = \frac{g\beta_o Q_o''' H_o^{\,5}}{\alpha_o \nu_o k_o}$	Rayleigh number
θ	Angle from bottom of the ceramic pool, degrees
θ_{tot}	Maximum angle at upper surface of ceramic pool, degrees
$Nu_{dn}(\theta)$	Pool Nusselt number in the downward direction
$\overline{Nu}_{dn}(\theta)$	Average ceramic pool Nusselt number in the downward direction

Angular-dependence of heat transfer coefficient:

θ	Angle (degrees)
θ_0	Angle measured from the bottom of vessel shall to the inner vessel surface where the ceramic molten pool contacts the surface (Degrees)
$h_d(\theta)$	Local heat transfer coefficient, W/m^2-K
$\overline{h_d}$	Average heat transfer coefficient, W/m^2-K

Table 2.2 Ranges of applicability of the correlations listed in Table 2.1

Model		Heat Transfer Correlation	Range of applicability	
			Ra	Pr
ERI [1-2]	Ceramic Pool	Mayinger [24]	$7x10^6 – 5x10^{14}$	0.5
		Kulacki-Emara [31]	$2x10^4 – 4.4x10^{12}$	7
	Top Metal Layer	Globe-Dropkin [29]	$3x10^5 – 7x10^9$	0.02-8750
		Churchill-Chu [30]	$0.1 – 10^{12}$	Any
DOE [18]	Ceramic Pool	Mini-ACOPO [32]	$10^{12} – 7x10^{14}$	2.6-10.8
	Top Metal Layer	Globe-Dropkin "Specialized"	$3x10^5 – 7x10^9$	0.02-8750
		Churchill-Chu	$0.1 – 10^{12}$	Any
INEEL 19]	Ceramic Pool	ACOPO	$10^{12} – 2x10^{16}$	
	Top Metal Layer	Globe-Dropkin	$3x10^5 – 7x10^9$	0.02-8750
		Churchill-Chu	$0.1 – 10^{12}$	Any

Table 2.3 Critical heat flux coefficients for various Westinghouse lower head insulation design configurations

Coefficient	AP600 Configuration III [18]	AP1000 Configuration IV	AP1000 Configuration V
A_{CHF}	4.9×10^{5}	See Note (1)	See Note (2)
B_{CHF}	3.02×10^{4}	"	"
C_{CHF}	-8.88×10^{2}	"	"
D_{CHF}	13.5	"	"
E_{CHF}	-6.65×10^{-2}	"	"

[1] These values were not available at the time the present study was performed, but Westinghouse maintained that the CHF was 20% to 30% higher than the Westinghouse lower head insulation Configuration III.

[2] These values were not available at the time the present study was performed, but Westinghouse maintained that the CHF was 20% higher than Configuration IV.

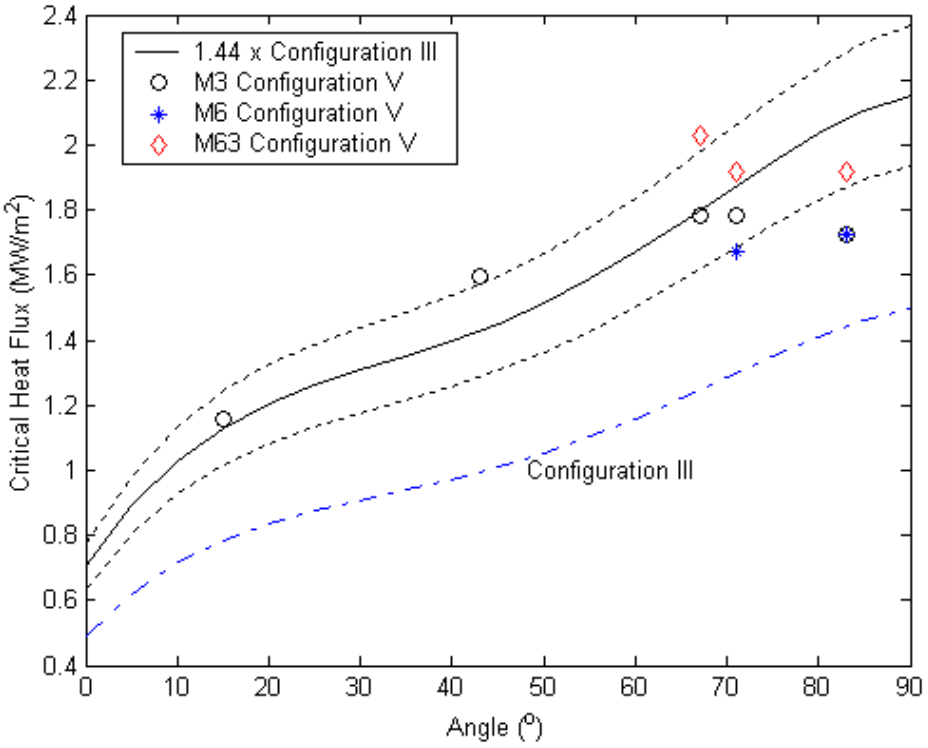

Figure 2.2 Lower head Configuration V critical heat flux data [28] (Note: the black dashed lines represent ±10% variation from the solid line that is assumed in the present study. These are not the actual uncertainties in the measurements of CHF)

2.2 Material Properties

The material properties are calculated using the approach proposed in Reference [19]. The details of the approach that is used to calculate the various physical properties are provided in the Appendix A.

2.3 Decay Heat

The decay heat for the base case is assumed to reside entirely in the ceramic (oxide) pool for the two-layer melt configuration (oxide pool at the bottom and a metallic pool at the top). This is reasonable, because the major challenge from the light metallic pool overlying the ceramic layer is the focusing effect, and the decay heat in the metallic layer is expected to play a secondary role. Therefore, the critical heat flux could be exceeded for the thin top metallic layer configurations. However, for the three-layer configuration envisioned in Figure 2.1, the impact of the decay heat in the heavy metal layer below the oxide layer, is expected to be more significant. In this case, the decay heat is partitioned between the oxide layer and the heavy metal layer.

In the present analysis, the partitioning of the decay heat between the ceramic and the heavy metallic layers is calculated using a simple approach that is based on the mass fraction of U in the respective layers, that is:

$$\begin{aligned} Q_h''' + Q_o''' V_o &= P_{decay-tot} \\ \frac{Q_h''' V_h}{Q_o''' V_o} &= \frac{m_U (270/238)}{m_{UO_2}} \end{aligned} \tag{2.30}$$

where m_U is the mass of uranium in the bottom (heavy) metallic layer, and m_{UO_2} is the mass of UO_2 in the ceramic layer.

Another approach [33] would be to partition the decay heat into the bottom heavy metal layer based on the equivalent volume of the material that has reacted to produce the uranium metal:

$$\frac{Q_h'''}{Q_o'''} = \frac{m_U (270/238)}{\rho_o V_h} \tag{2.31}$$

The impact of heat generation in the upper metallic layer is assessed as part of a sensitivity study that is discussed in Section 4.3 of this report. For this case, the fraction of decay heat in the metal layer is based on the formulation in Reference [19]:

$$f_{metal} = (1 - f_{ox-Zr})[f_{group4} + f_{Zr\&Nb}] + f_{group6} \tag{2.32}$$

$$f_{Zr\&Nb} = M_{Zr\&Nb} t_r + B_{Zr\&Nb} \tag{2.33}$$

$$f_{group6} = M_{group6} t_r + B_{group6} \tag{2.34}$$

$$f_{group4} = M_{group4} t_r + B_{group4} \tag{2.35}$$

where t_r is the time of core release, f_{ox-Zr} is the fraction of Zr oxidized, and the coefficients are given as [19]:

	$0 \le t_r < 18000$ sec	$18000 \le t_r < 28880$ sec
B_{group4}	0.0572	0.0334
B_{group6}	0.0688	0.0828
$B_{Zr\&Nb}$	0.1068	0.1326
M_{group4}	-1.473E-6	-1.502E-7
M_{group6}	+1.236E-6	+4.572E-7
$M_{Zr\&Nb}$	+2.154E-6	+7.197E-7

2.4 Results of Benchmarking Calculations

The present model discussed in the previous sections is benchmarked against the results of the DOE [18] and the INEEL [19] studies for AP600, as documented in Appendix D of Reference [19]. These results are digitized and compared with point estimate calculations using the present model, based on the input parameters listed in Table C-1 of Reference [19]. The description of the various inputs for the present ERI model is provided in Table 2.4. It should be noted that the material property data in Table 2.4 are derived based on those provided in Table C-1 of Reference [19].

As mentioned previously, in the present ERI model the temperature of the 'other structures' (i.e., serving as the radiative heat sink in Equation (2.8)) is assumed known. In the DOE and INEEL models, the 'other structures' are defined as the core barrel, whose temperature is calculated assuming conduction through the core barrel and radiation to the inner surface of the vessel wall. However, the results of the calculations in Reference [19] show that the structure temperature is essentially constant at about 950K. Therefore, in the present ERI model, it is assumed that the temperature of the 'other structures' acting as the radiation heat sink is fixed at 950K.

Figures 2.3 through 2.8 show the comparison of the benchmarking calculations for the present ERI model to the DOE and INEEL models. For the ERI model, two calculations are performed. In the first calculation,

the heat transfer correlations are assumed to be the same as those in the DOE model (refer to Table 2.1). In the second calculation, the heat transfer correlations are changed to the ERI heat transfer correlations as documented in Reference [1] and listed in Table 2.1.

The results of the present ERI model calculations show good agreement with the results reported in Reference [19] for both DOE and INEEL models, and this agreement is especially good as compared to the INEEL results. The initial conditions in the ERI model are taken directly from the INEEL study [19], and it is not surprising that such good agreement exists. Both the ERI and INEEL model predictions are somewhat different from those of Reference [18], particularly for the light metallic layer. As stated in Reference [19], the reason for these observed differences is most likely due to the differences in the values for some of the parameters used in Reference [18] calculations.

The results of the benchmarking calculations also show that the model predictions are not very sensitive to the choice of heat transfer correlations. In fact, the difference between the two sets of the present ERI model predictions with different set of heat transfer correlations is less than 5%.

Table 2.4 ERI Input description for the benchmarking calculations

Parameter		**Value**
Water saturation temperature (K)		400
Lower Head	Thermal conductivity (W/m-K)	32
	Melting temperature (K)	1600
	Inner radius (m)	2
	Thickness (m)	0.15
Molten Ceramic Pool	Density (kg/m^3)	8191
	Volume (m^3)	10.85
	Thermal conductivity (W/m-K)	5.3
	Kinematic viscosity (m^2/sec)	5.7x10^{-7}
	Specific heat capacity) (J/kg-K)	533.2
	Thermal diffusivity (m^2/sec)	1.12 x10^{-6}
	Thermal expansion coefficient(K^{-1})	1.05 x10^{-4}
	Height of Pool (m)	1.52
	Pool Angle (deg)	76.14
Metallic Pool	Density (kg/m^3)	6899.2
	Thickness (m)	0.9273
	Thermal conductivity (W/m-K)	25
	Kinematic viscosity (m^2/sec)	5.9 x10^{-7}
	Specific heat capacity (J/kg-K)	789.5
	Thermal diffusivity (m^2/sec)	4.59 x10^{-6}
	Thermal expansion coefficient) (K^{-1})	1.11 x10^{-4}
	Melting temperature (K)	1600
Ceramic pool heat generation (MW/m^3)		1.3
Ceramic pool melting temperature (K)		2973
Other structure area (m^2)		75.4
Other structure temperature (K)		950
Ceramic Crust	Density (kg/m^3)	8191
	Thermal conductivity (W/m-K)	2.8
	Specific heat capacity (J/kg-K)	533.2
	Thermal diffusivity (m^2/sec)	5.7 x10^{-7}
	Volumetric heat generation rate (MW/m^3)	1.3
Upper steel layer surface emissivity		0.45
Upper structure emissivity		0.8

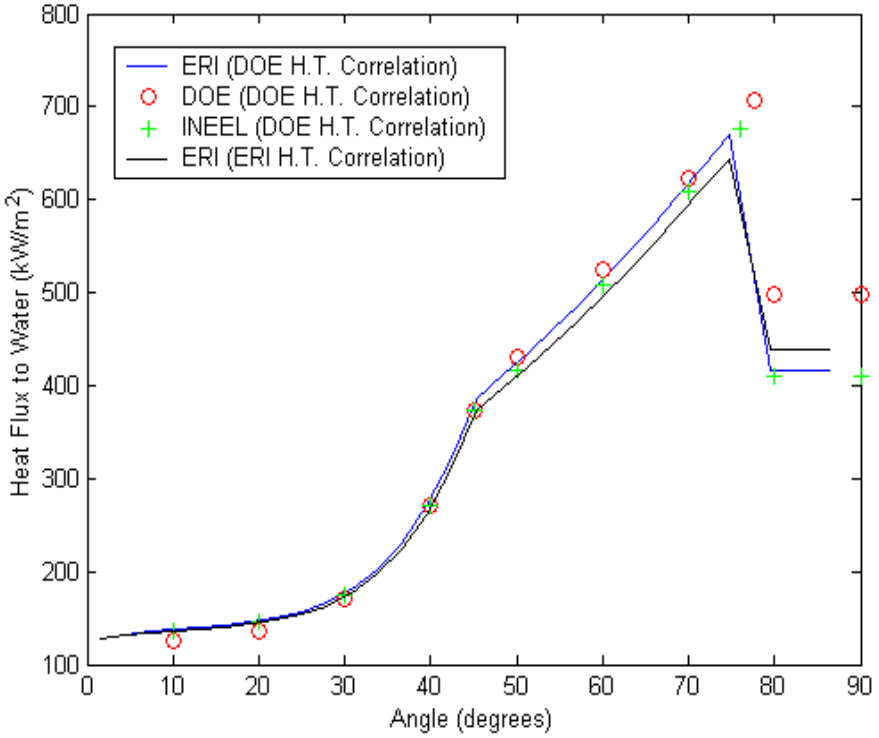

Figure 2.3 Angular variation of wall heat flux (benchmarking calculation)

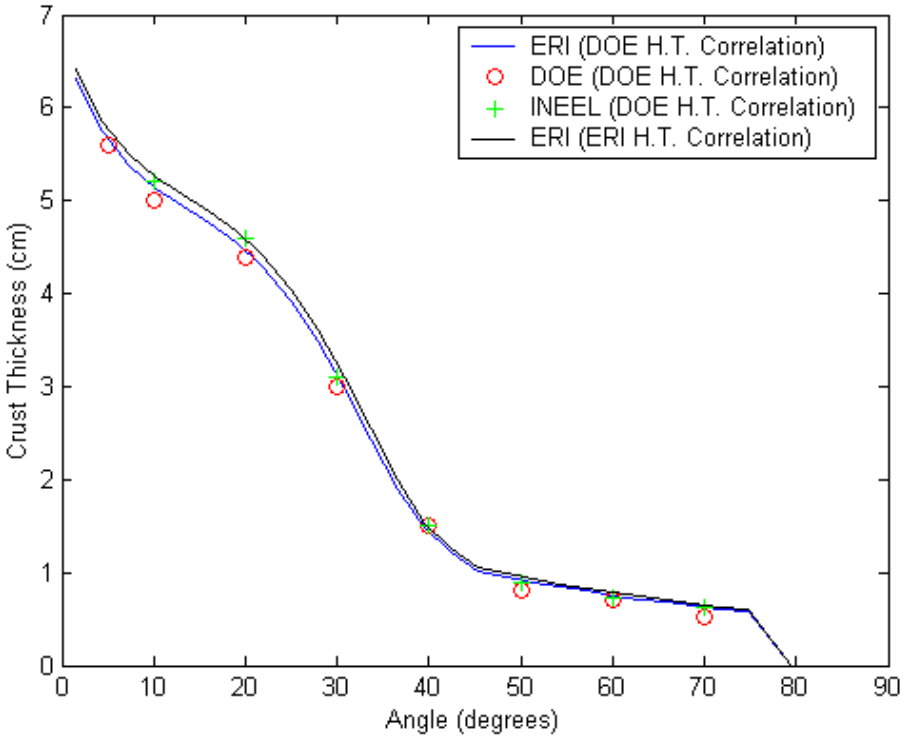

Figure 2.4 Angular variation of corium crust thickness (benchmarking calculation)

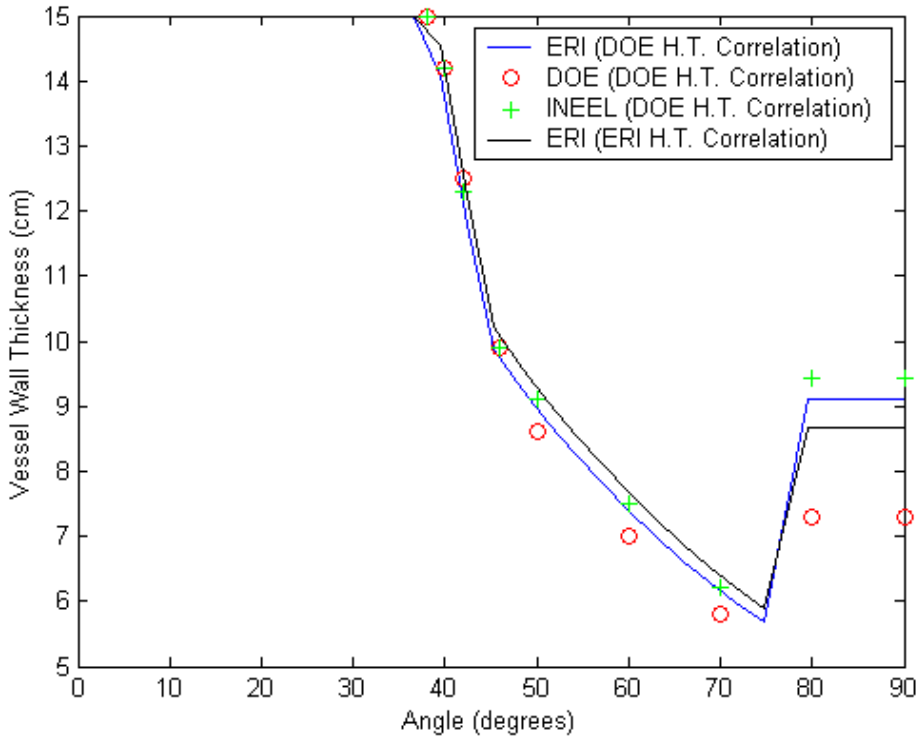

Figure 2.5 Angular variation of vessel wall thickness (benchmarking calculation)

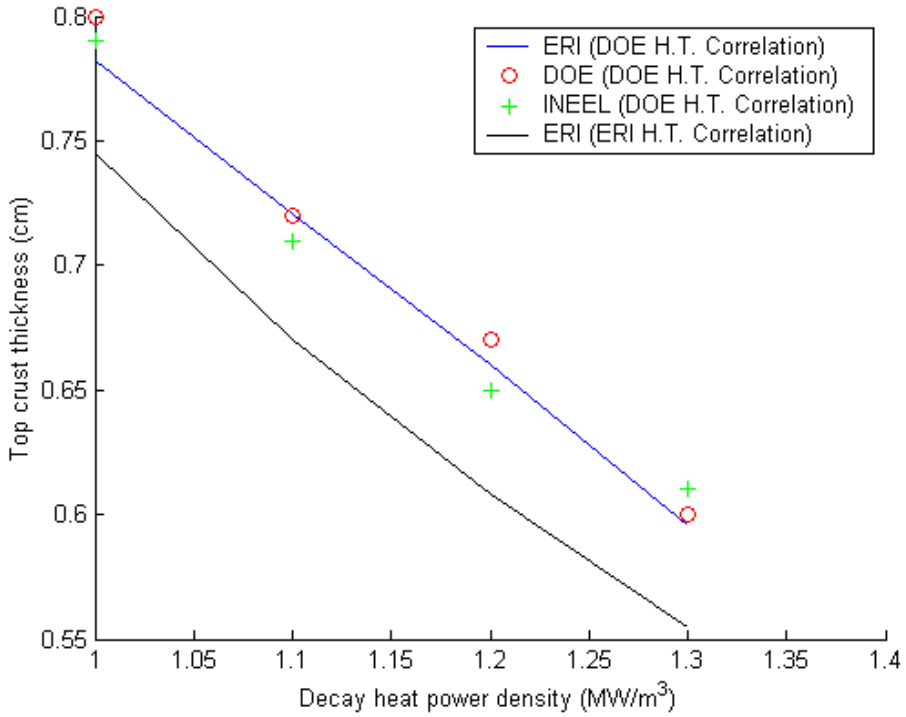

Figure 2.6 Response of the upper crust thickness to the decay heat power density (benchmarking calculation)

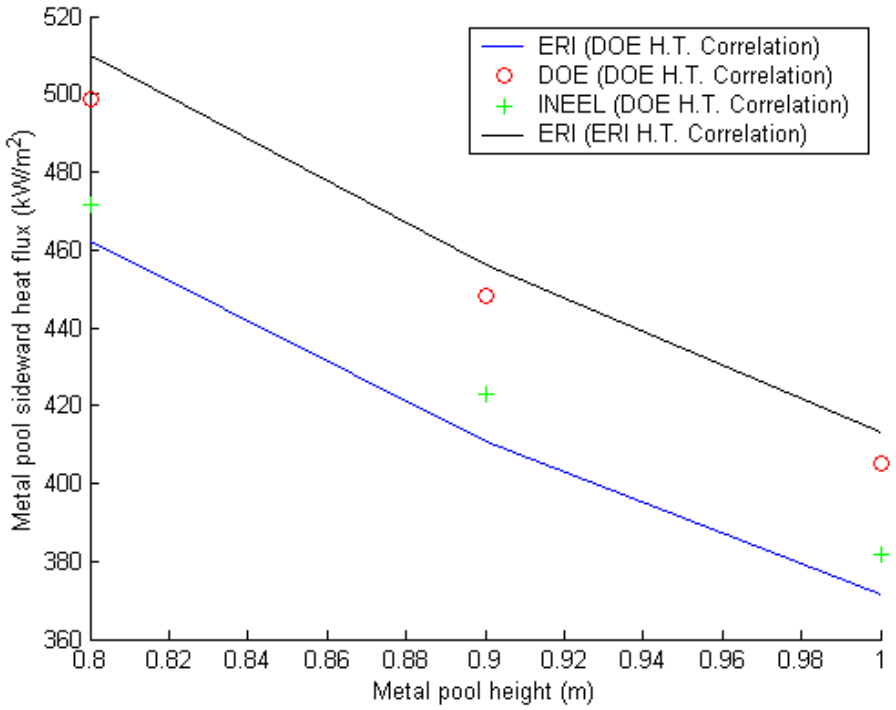

Figure 2.7 Response of the metal pool sideward heat flux to the metal pool height (benchmarking calculation)

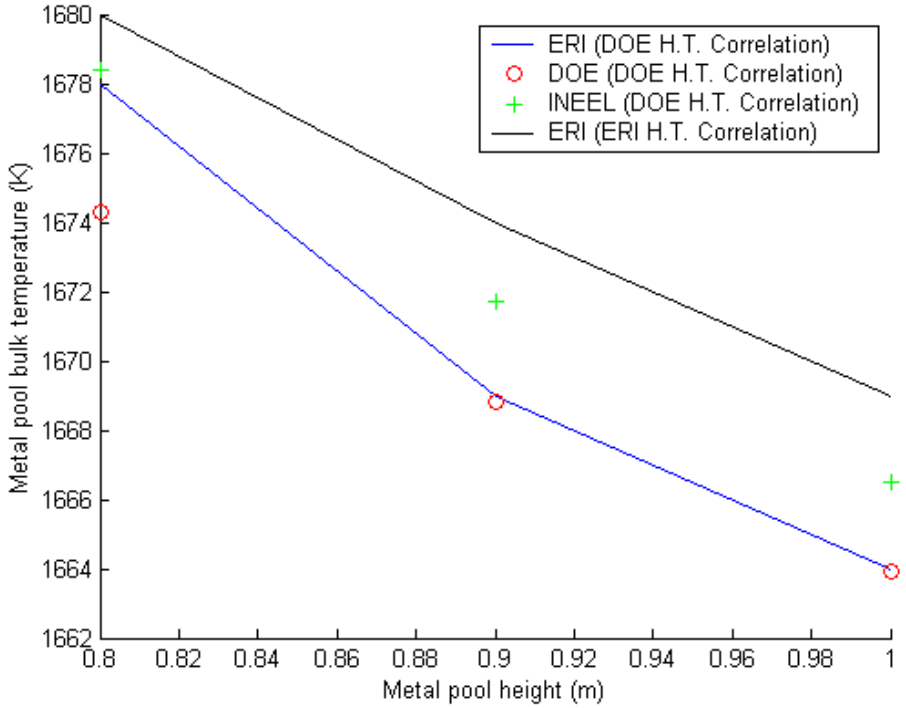

Figure 2.8 Response of the metal pool bulk temperature to the metal pool height (benchmarking calculation)

3. INITIAL CONDITIONS APPLICABLE TO ANALYSIS OF IN-VESSEL RETENTION

3.1 Background

The delineation of the initial conditions involves the specification of the mass of debris relocating to the lower plenum, the composition of the debris, the melt configuration of the debris in the lower plenum, the decay power, and the thermo-physical properties of the debris in the lower plenum and the vessel wall. The conditions in the cavity (water temperature and pressure) play a secondary role as long as the lower head is covered with water, because the vessel wall outer temperature should remain very close to the water saturation temperature in the nucleate boiling regime.

The vessel is expected to fail when the heat flux from the debris to the vessel wall exceeds the Critical Heat Flux (CHF) limit. Therefore, the critical heat flux plays an important role in the success of cooling by water on the external surface of the lower head to retain the debris inside the vessel and to avert vessel failure. It is important to note that under extreme conditions, the melting of the lower head can lead to significant thinning of the vessel wall even though the local heat flux remains at or below the critical heat flux [1].

A study of external reactor vessel cooling was conducted for AP600 as documented in Reference [18]. This study concluded that the failure of an externally flooded AP600 reactor vessel is physically unreasonable. This is because the heat flux remained below the critical heat flux, and the structural calculations based on the minimum vessel wall thickness indicated that vessel retains its integrity as long as the heat flux is below CHF.

Reference [18] was subjected to a peer-review, and a number of reviewers questioned some of the assumptions regarding the initial conditions in this study. Following the submission of the AP600 DOE report by Westinghouse to the Nuclear Regulatory Commission (NRC), INEEL was contracted by NRC to perform: (1) an in-depth critical review of the AP600 DOE study and the model used; (2) an assessment of the peer reviewer comments and the authors' responses to identify areas where the peer reviewer concerns were not adequately addressed; and (3) an independent confirmatory analysis.

The results of the INEEL study are documented in Reference [19]. In general, INEEL identified the following items where it was judged that the peer review concerns were not adequately addressed by the authors of Reference [18], thus requiring additional analyses:

- Range of the uncertainty distributions for the input parameters (i.e., the ranges were not considered to be sufficiently broad)
- Debris melt configuration (i.e., did not include alternative intermediate states)
- Decay heat in the metallic layer (i.e., the layer may contain heat sources from oxidation, fission product retention or dissolved uranium)
- Emissivity of the metallic layer (i.e., emissivity was considered to be high)
- Critical heat flux and insulation effects (i.e., comments regarding the applicability of ULPU data and the impact of phenomena such as insulation effects, surface fouling, etc.)
- Cavity flooding time (i.e., issues regarding partial flooding and lower subcooling)
- Decay heat load (i.e., comments on the potential for a higher decay heat)
- Validity of the ACOPO correlations – prototypic material effects (i.e., experimental verification)
- Validity of the ACOPO correlations during transient time (i.e., higher heat fluxes can occur at locations where CHF is the lowest)
- Validity of the ACOPO correlations – vapor transport effects (i.e., enhanced heat transfer due bubble rise)
- Vessel wall melting temperature (i.e., concerns that the range of possible eutectic temperatures was not evaluated)
- Ceramic pool liquidus temperature (i.e., suggestions for consideration of other possible temperatures).

To address these concerns, Rempe, et al. [19] re-quantified the initial conditions applicable to several input parameters, and subsequently performed sensitivity analyses to demonstrate their bounding impact on the lower head integrity. The sensitivity analyses were primarily focused at the various heat transfer correlations used in Reference [18] in order to compensate for the lack of sufficient experimental data.

In the INEEL study, the quantification of the debris mass and composition in the lower plenum and the timing of the core relocation into the lower plenum (that can impact the decay heat), were based primarily on the results of the SCDAP/RELAP5 calculations that were performed by INEEL for AP600. In addition, in the INEEL study, two new debris pool configurations were also introduced. The additional melt configurations included:

(1) Melt Configuration B - a four-layer system composed of a ceramic pool at the bottom, a thin molten metallic layer on top of it, followed by a second molten ceramic pool on top of the thin metal layer, and finally a top molten light metallic layer.

(2) Melt Configuration C - a heavy molten metal layer containing dissolved uranium in unoxidized Zircaloy located below the molten ceramic pool.

The Melt Configuration A in the INEEL study was similar to that of the DOE study [18], namely, a molten ceramic layer topped by a molten metallic layer.

One of the major observations in both the DOE and the INEEL studies was the focusing effect of the molten light metallic layer that could result in a large heat flux (transfer of heat over a relatively small heat transfer area) possibly exceeding CHF at the locations of the thin metallic layers. For a thin metal layer on top of the ceramic pool, a portion of the decay heat in the lower ceramic pool needs to be dissipated though a small surface area bounded by the metal layer. Therefore, the factors that could potentially compromise the vessel integrity in the metal layer are the amount of steel and the decay power in the lower ceramic layer.

The AP1000 reactor is expected to operate at a power level that is about 75% higher than AP600 core thermal power (76% in total plant NSSS power). This increased power is achieved through an increase in the core length and the number of core fuel assemblies, while retaining the same fuel assembly design, reactor pressure vessel diameter, and Reactor Coolant System (RCS) piping dimensions. In addition, the AP1000 design has replaced the in-vessel steel reflector plates of the AP600 with a 7/8" thick core stainless steel shroud. The bottom plate of the shroud is mounted flush on the core support plate. The core barrel is 2" thick and hangs from the upper head flange. Cooling holes through the core shroud provide cooling flow to the shroud from the core flow. Furthermore, the sizes of the reactor coolant pumps, the steam generators, and the pressurizer have been increased to accommodate the increased power level.

The changes in the AP1000 design that could potentially impact in-vessel debris retention include:

- Reactor power that has increased to 3400 MW(t),
- The existence of the core shroud in AP1000 versus the reflector in AP600, and
- The use of a thicker (by about an inch) lower core support plate.

In the AP1000 Probabilistic Risk Assessment (PRA) [9], Westinghouse has relied on the DOE AP600 methodology to quantify the heat flux from the debris to the lower head. However, because of the higher power in the debris (resulting in an earlier core relocation after accident initiation), the AP600 CHF was expected to be exceeded for AP1000. Therefore, Westinghouse has introduced design changes in AP1000 to increase the margin to CHF and thereby, vessel failure. The UPLU Configuration IV for AP1000 that relies on natural circulation of two-phase mixture through the insulation region has been shown experimentally to achieve up to 30% increase in the critical heat flux.

In order to assess the implications of changes in design, and the impact of the identified deficiencies in the original AP600 DOE study, the present study has been conducted for AP1000.

This assessment for AP1000 considers the insights from the studies that have been conducted over the last decade, and utilizes the mathematical model that was described earlier for the following debris melt configurations in the AP1000 lower plenum:

- Melt Configuration I - A molten ceramic pool with an overlaying molten light metallic layer, and

- Melt Configuration II - A molten ceramic pool sandwiched between a bottom heavy metallic layer and a top light metallic layer.

These two melt configurations are believed to be bounding in terms of their impact on the lower head integrity for AP1000. The first configuration is similar to the melt Configuration A in the INEEL study [19] and that used in References [9] and [18] and considers the impact of the low metallic mass (i.e., smaller metallic layer thickness and heat transfer contact area) that tends to increase the heat flux to the vessel wall and the outside water. The second configuration is a combination of melt Configurations A and C in the INEEL study [19] that can simultaneously simulate the presence of two metallic layers, also considered in a recent Westinghouse study [33].

3.2 Specification of Initial Conditions for AP1000

In the present assessment, the uncertainties associated with the initial conditions include the decay power, fraction of Zr oxidation, mass of UO_2 relocation to the lower plenum, and the amount steel in the lower plenum debris.

The mass and composition of various regions inside the vessel are provided in Table 3.1 that is a reproduction of Table 39A-1 (in the revised Chapter 39 [34]) from the AP1000 PRA [9]. The total mass of steel including the lower internal is 68 mt.

The mass and composition of debris in the lower plenum after core relocation is dependent on the accident scenario. However, there are significant uncertainties with late phase melt progression. In the present assessment, the scenarios of interest involve full depressurization of the Reactor Coolant System (RCS). According to the AP1000 PRA [9], accident classes 3BE, 3BL, and 3D are scenarios that can achieve dry vessel configuration and are therefore of interest to in-vessel retention. Scenario 3BE has a conditional probability of 0.5 within the subset of the plant damage states, with scenario 3BL with a conditional probability of 0.35 and scenario 3D with a conditional probability of 0.15.

In the present assessment, the quantification of the initial conditions is based on the results of plant-specific MELCOR calculations by ERI [35-36], and MAAP calculations by Westinghouse (in the revised Chapter 39 for AP1000 PRA [34]). In addition, the insights gained from previous studies for AP600 [1, 18], comments by peer reviews of these studies, and the plant-specific SCDAP/RELAP5 calculations by INEEL for AP600 are also used, where appropriate. The uncertainty distributions are developed for the proposed ERI Configuration I only, similar to the DOE study and INEEL configuration A. The ERI Configuration II is a postulated intermediate debris state that is based on the peer reviewer comments as documented in the AP600 DOE study [18]. For this configuration, only sensitivity analyses are performed.

3.2.1 Decay Heat

The decay heat in the ceramic pool plays an important role in the total heat flux from the debris to the vessel wall and the molten metal layers. Therefore, the quantification of the decay power in the ceramic pool is very important. It should be noted that in the ERI Configuration I (ceramic pool with a molten steel layer on top), the decay energy is assumed to reside in the ceramic pool by default (later, the results of a sensitivity case will be presented to show the effect of this assumption, by allocating a portion of the decay heat from the ceramic layer into the top metallic layer). For the present ERI Configuration II, the decay power is partitioned between the ceramic pool and the bottom (heavy) metallic layer (see Section 2.2).

According to the AP1000 plant-specific MELCOR calculations [35], core relocation to the lower plenum occurs between 2.6 hours (time of core support plate failure) for a large Loss of Coolant Accident (LOCA) (i.e., scenario 3BR) and 3.7 hours for scenario 3BE. At the time of core relocation to the lower plenum, the whole core decay heat is about 24 MW for scenario 3BR and 23 MW for a medium-sized DVI line break (i.e., scenario 3BE). This decay power accounts for the loss of volatile fission products from the melt. In the Westinghouse MAAP calculation documented in the revised Chapter 39 of AP1000 PRA in response to NRC RAI 720.088 [34], the time of core relocation is about 1.7 hours, and the total core power is 28.7 MW. In Reference [19], INEEL compared the decay power used in the DOE study [18] with the 1979 ANS 5.1 Standard and considered a 10% uncertainty in the decay power for AP600. By scaling the decay power from AP600 (1933 MW(t)) to AP1000 (3400 MW(t)), the decay heat at various times of interest are tabulated in Table 3.2.

For scenario 3BE at 3.7 hours, the decay power is between 26 and 29 MW(t) accounting for the loss of volatiles. MELCOR predicted a decay power of 23 MW at 3.7 hours. For a core relocation time of 6000 seconds as predicted by MAAP calculation, MELCOR predicts a whole core decay power of 38 MW(t).

Therefore, following the above discussion, the uncertainty distribution for the decay heat as shown in Figure 3.1 is proposed. This distribution assumes that the most likely decay heat values correspond to the range of 23 to 29 MW(t) for AP1000, with a low likelihood that the debris pool decay heat could be expected to exceed 29 MW(t).

Table 3.1 Core and lower internals material inventories in the AP1000 reactor vessel

Component	Material	Mass (mt)
Core		
Fuel	UO_2	95.9
Active Core Cladding	Zircaloy	17.9
Additional Zirconium	Zircaloy	4.8
Control Rods	Silver/Indium/Cadmium	3.9
Total core	All	122.5
Lower Internals (below top of active fuel)		
Core Barrel	Stainless Steel	19
Lower support plate	Stainless Steel	25
Core shroud	Stainless Steel	12
Shroud support structure	Stainless Steel	9
LP energy absorber	Stainless Steel	3
Total lower internals	All	68
Total core & lower internals	All	190.5

Table 3.2 Comparison of decay heat

Time (s)	Decay Power 1979 ANS 5.1 Standard [MW(t)]		Decay Power 1979 ANS 5.1 Standard + 10% [MW(t)]		Decay power fraction accounting for loss of volatile fission products[1]
	AP600	AP1000	AP600	AP1000	
5000	25.0	43.9	27.5	48.3	0.73
10000	20.4	36.0	22.4	39.6	0.76
20000	16.9	29.6	18.6	32.6	0.80

[1] Based on Figure 7.2 of Reference [18].

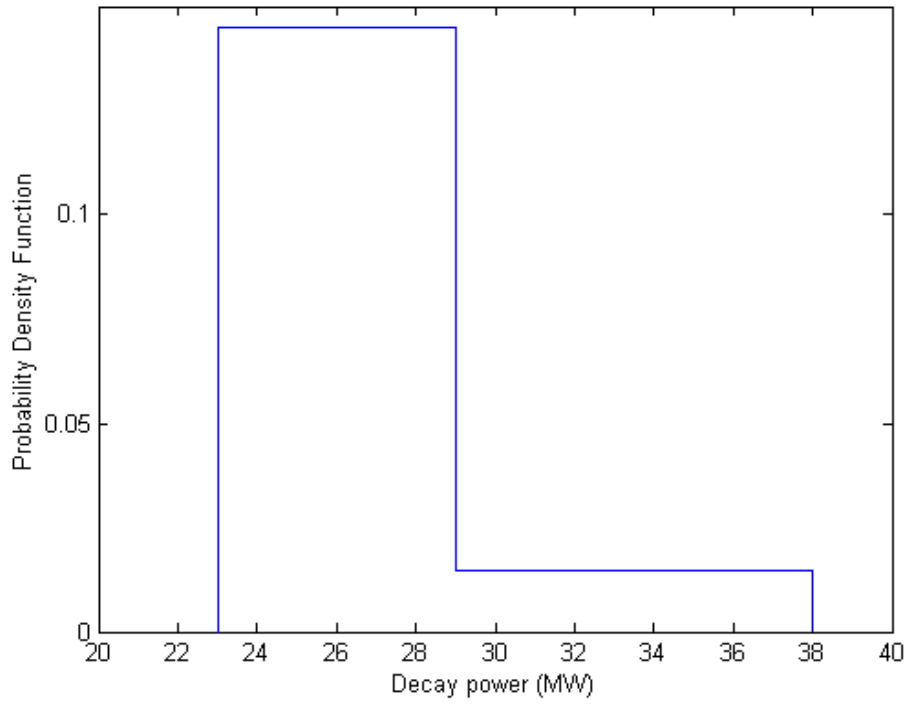

Figure 3.1 Distribution of decay power for AP1000

3.2.2 Zr Oxidation Fraction

The results of the AP1000 plant-specific MELCOR calculations for the 3BR and 3BE scenarios show about 50% of the core inventory of Zr is expected to be oxidized prior to significant melt-pool relocation to the lower plenum. In the MAAP calculation in the AP1000 PRA (revised Chapter 39 [34]), the Zr oxidation fraction was estimated to be about 0.3, which is relatively low. In the DOE AP600 study [18], the most probable range for Zr oxidation fraction is between 0.4 and 0.6, and for the range between 0.6 to 0.7 and 0.7 to 0.9, lower probabilities are assigned. For the high-pressure scenarios considered as part of the NRC Direct Containment Heating (DCH) issue resolution for Pressurized Water Reactors (PWRs) [37], the most probable Zr oxidation fraction was about 0.4, and lowest value was 0.2 with an upper bound of about 0.6. Even though the high pressure scenario conditions that were considered for the DCH issue resolution study is not directly relevant to this study, nevertheless, it is being referenced to show the range of uncertainties that have been considered in recent years and for previous studies.

Therefore, following the above considerations, and the results of the MELCOR plant-specific calculations, the most probable range for the present study is between 0.4 and 0.6 as shown in Figure 3.2. MELCOR sensitivity calculations show that the Zr oxidation fraction can vary from 0.5 to 0.65 [35]. The lower range of 0.3 to 0.4 is considered based on the single MAAP calculation but with a lower probability. The upper bound of the Zr oxidation in this study is assumed to be 0.8. This is mainly due to the fact that even though full-loop natural circulation of steam throughout the primary circuit is expected[3], nevertheless, metallic blockages are likely to impede the extent of Zr oxidation.

3.2.3 Ceramic Relocation to the Lower Plenum

The total core UO_2 inventory in AP1000 is about 96 mt as shown in Table 3.1. In the DOE study for the AP600 [18], it was assumed that the entire core relocated to the lower plenum resulting in the submergence, and eventual melting of the lower core support. The melting of the lower core support plate, the massive core reflector, and the previously formed metallic blockages, resulted in a substantial quantity of steel that was assumed to float on the top of the ceramic pool.

In the SCDAP/RELAP5 analysis for AP600 discussed in Reference [1], the initial relocation of the core to the lower plenum involved about 50% of the core UO_2 inventory by about 12000 seconds, and the subsequent relocation of an additional 35% of the core UO_2 inventory at about 800 seconds later. However, this relocation scenario assumed that all relocated debris immediately passed through the perforations in the core support plate. But if the relocated core debris could be retained on the core support plate, additional calculations (see discussions in Reference [1]) suggest that the first relocation could last for more than an hour. Clearly, such a case is plausible given inherent uncertainties in late phase in-vessel melt progression.

In the Westinghouse MAAP calculation (revised Chapter 39 of AP1000 PRA [34]), the initial crucible contained about 72,600 kg of molten ceramic material (about 70% of the core UO_2 inventory). Upon failure of the melt crucible/crust, about 48 mt of UO_2 (~50% of the core inventory) was calculated to relocate into the lower plenum at about 6000 seconds into the accident. However, in the MAAP calculation, the relocation was gradual, and eventually a significant portion of the core relocated to the lower plenum that subsequently resulted in the submergence of the lower core steel support plate. Therefore, the initial relocation in the MAAP calculation was similar to the SCDAP/RELAP5 calculation for AP600. This is not to minimize the significant uncertainties in the later phase melt progression and core debris relocation, but to emphasize that given the current state of knowledge, an estimate of core relocation can only be made if a wider range of conditions are envisioned. In the MELCOR calculations for scenarios 3BE and 3BR [35], the initial relocation involved about 77 mt of UO_2 (80% of core inventory).

For the sake of comparison, it is interesting to note the distribution assumed for a wet core condition in a high pressure transient for the DCH issue resolution study for existing PWRs [37]. Clearly, the high-pressure conditions of the scenario as envisioned for the DCH study is not applicable to the present low-pressure case in AP1000; nevertheless, given the phenomenological uncertainties in the late phase melt progression, the RCS pressure may play a less decisive role in so far as the melt progression and relocation phenomena are concerned. In the high-pressure scenario, about 70% to 80% of the core was contained in the initial crucible, and upon failure of the crust, it was assumed that 50%

[3] Note that the AP1000 design does not have the "loop-seal" configuration of the existing Westinghouse plants; thereby, most severe accidents would involve a high potential for full-loop natural circulation, albeit with various degree of intensity, depending on the RCS pressure level, and other conditions of the accidents.

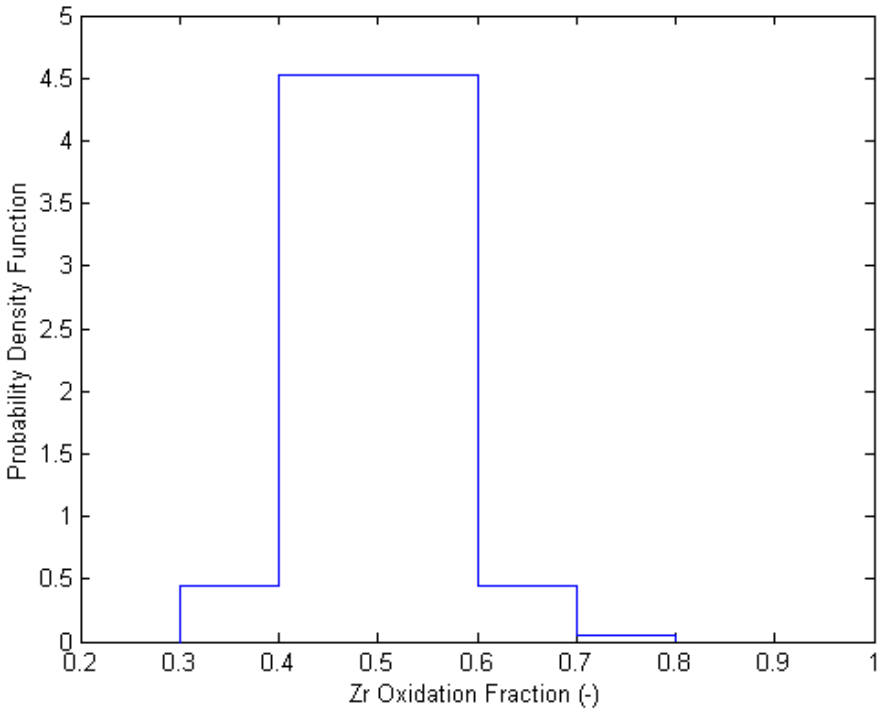

Figure 3.2 Distribution of Zr oxidation for AP1000

of melt would be released to the lower plenum. Therefore, the best estimate value of the initial relocation involved about 40% of the core, with the upper bound of about 80%.

In the present assessment, it is assumed that a significant portion of the core (~70% to 80%) would melt and relocate to the lower plenum, but relocation involving a lower mass of the molten core (~50%) cannot be ruled out. This is true especially in light of the fact that the vessel is cooled with the cavity water flowing through the insulation, and there is potential for cooling of the core barrel (by radiation to the vessel wall, subsequent conduction across the vessel wall and convection/boiling of the cavity water flowing through the insulation). Therefore, it is conceivable that there could be a time window before the occurrence of a second relocation of the ceramic rich molten debris into the lower plenum region [36].

Using the phenomenological picture just described, the proposed uncertainty distribution of Figure 3.3 considers the potential for relocation of a smaller fraction of the core debris into the lower plenum. Note that the upper bound of the uncertainty distribution is not that critical, because as the mass of the ceramic pool increases, it is expected to submerge the core lower support plate resulting in significant addition of molten steel on top of the ceramic pool, thereby mitigating the focusing effect of the thin stratified metallic layer.

The mass of ZrO_2 in the ceramic pool is assumed to scale with the mass of fuel relocated to the lower plenum, and the fraction of Zr oxidation. Therefore, the mass of ZrO_2 is given by:

$$M_{ZrO_2} = \frac{M_{UO_2}}{M^o_{UO_2}} f_{Zr} M^o_{Zr} \frac{123}{91} = M_{UO_2} f_{Zr} \frac{17.9}{95.9} \frac{123}{91} \qquad (3.1)$$

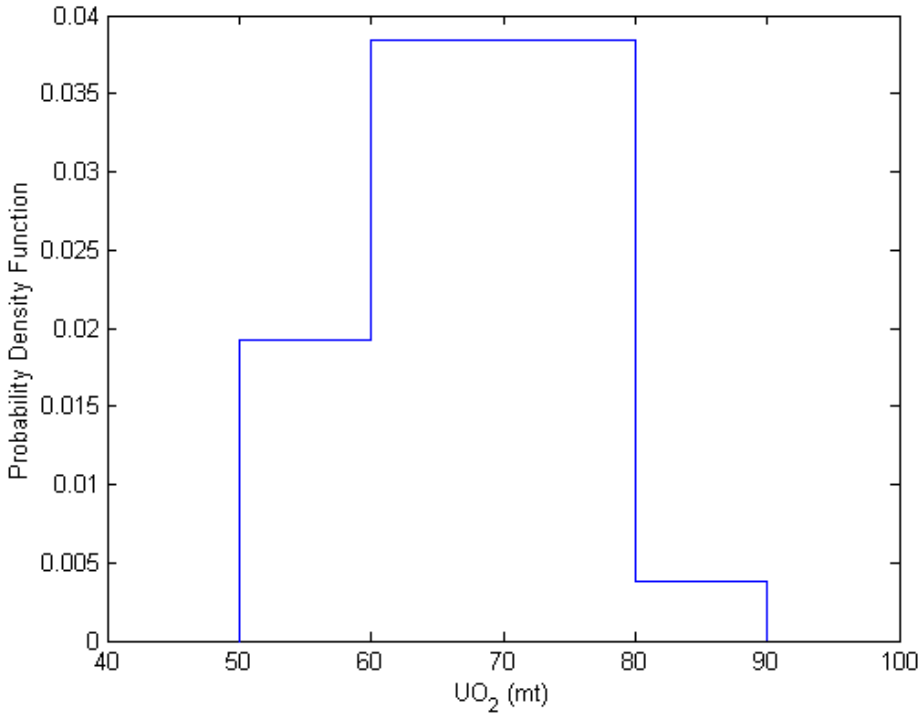

Figure 3.3 Distribution of UO_2 in the lower plenum for AP1000

where f_{Zr} is the fraction of core Zr oxidation, M^o_{Zr} is the core Zr inventory, $M^o_{UO_2}$ is the core UO_2 inventory, and M_{UO_2} and M_{ZrO_2} are the masses of UO_2 and ZrO_2 in the ceramic pool, respectively.

3.2.4 Molten Metal Distribution in the Lower Plenum

One of the most important aspects of the in-vessel melt retention is the potential for the formation of a top (light) metallic layer, especially if the layer is thin enough to cause significant focusing effect. In the present assessment, it is assumed that the mass of the steel layer is correlated with the mass of UO_2 in the lower plenum. For a low ceramic pool mass, the lower core support plate would not be submerged and therefore, the amount of steel would be limited. The distance from the bottom of the core support plate to the bottom of the vessel is 1.41 m, and the radius of the vessel lower head is 2 m. Therefore, the volume below the lower core support plate is 9.6 m^3. In the Westinghouse response to RAI 720.088 [34], it is estimated that the lower core support plate drops by about 9cm following the heat up of the core barrel/shroud. Following the drop in the lower core support plate, the volume below the plate is estimated to be about 8 m^3. Assuming a ceramic pool density of 8200kg/m^3, and the conservative volume of 8 m^3, the mass of debris is about 66 mt. Using Equation (3.1), the mass of UO_2 is estimated to be about 60 mt. Therefore, about 60 mt of UO_2 can relocate to the lower plenum without submerging the lower core plate. Under these conditions, the amount of steel in the upper metallic layer is very limited. It is assumed that the lower bound of steel mass is 3 mt that contains only the lower plenum energy absorbers from Table 3.1. In Reference [9], it was estimated that about 25% of core barrel could be molten prior to core relocation. Referring to Table 3.1, the total amount of steel could be as high as 8 mt that includes 3 mt of lower plenum energy absorbers, and 5 mt of core barrel. It is assumed that the quantity of steel varies in direct proportion to the mass of UO_2 as shown in Figure 3.4. Thus, for the 50 to 60 mt of UO_2 in the lower plenum, the steel mass can vary between 3 to 8 mt.

For higher molten pool mass, the core support plate would be submerged, and therefore, there is a discontinuity in the steel mass as a function of ceramic mass in the lower plenum shown in Figure 3.4. For this case, it is estimated that the entire lower core support plate would be molten, and significant portion of the core barrel and core shroud would melt and form a molten metallic pool on top of the ceramic pool. As a best estimate, given that 50% of shroud/barrel melt, the total steel mass is 48 mt. In the AP1000 PRA, the

lower bound steel mass was 51 mt [9]. In the present assessment, for the best estimate core UO_2 mass of 60 to 80 mt, the steel mass is assumed to vary between 40 to 60 mt (note that the total steel mass is about 70 mt according to Table 3.1). For the upper end of the spectrum, and for the higher UO_2 mass, the melt contains the rest of the steel.

Note that metal layer can contain some of the unoxidized Zr that was previously held-up in the metallic blockages in the lower regions of the core on top of the core support plate. Therefore, for UO_2 masses greater than 60 mt, the remaining Zr can be in the metallic layer:

$$M_{Zr} = M_{Zr}^{o}(1 - f_{Zr}) \tag{3.2}$$

Therefore, the dependence of the stainless steel in the lower plenum on the relocated ceramic mass for AP1000 (Figure 3.4), together with the distribution of the ceramic mass as shown in Figure 3.3, define the distribution of the light metallic layer. This is the most significant difference in the specification of initial conditions in the present study as compared with the Westinghouse analyses [9].

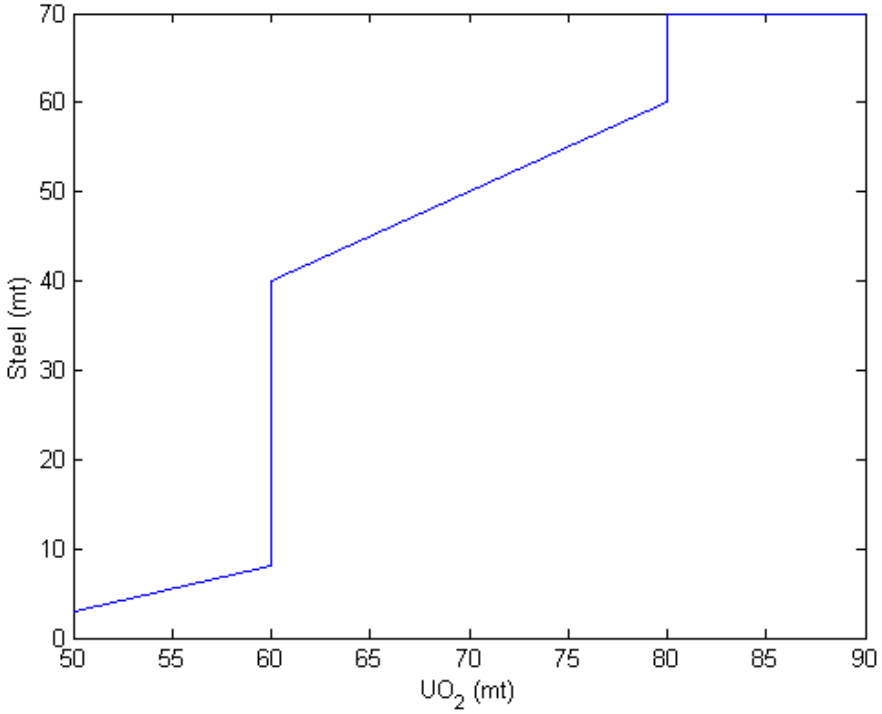

Figure 3.4 Relationship of stainless steel in the lower plenum and the ceramic mass for AP1000

4. RESULTS OF IN-VESSEL RETENTION ANALYSIS

4.1 Probabilistic Framework

In the present approach, the uncertainties in accident progression variables, and the model parameters, x_i, are represented by probability density functions, $f(x_i)$, representing the analyst's degree of belief in the expected range of the uncertainty domain, as discussed in Section 3.

The uncertainties are propagated through the present ERI model using the Latin Hypercube Sampling (LHS) [38] technique for the vector of random samples, y_j, defined by:

$$y_j = f_j(x_{1,j}, x_{2,j}, \ldots\ldots x_{i,j}, \ldots\ldots x_{k,j}) \qquad (4.1)$$

where j is the number of random samples, and k is the total number of variables with uncertainty.

The uncertainties in the vessel heat flux loads are determined as the output distributions based on the predictions of the present ERI model. The likelihood of vessel failure is dependent on the magnitude of heat flux. If the heat flux to the cavity water at any location exceeds the critical heat flux, RPV lower head failure is assumed.

4.2 Base Case (Melt Configuration I) Results

The results of the in-vessel retention are presented in this section. The LHS code was used to generate 1000 random samples from the distributions for the material properties (see Table 2.4), decay heat (Figure 3.1), Zr oxidation fraction (Figure 3.2), lower plenum ceramic and metal mass (Figures 3.3 and 3.4), and three other parameters listed in Table 4.1. The mean and standard deviation values in Table 4.1 are based on those reported in Reference [19].

For the base case, the heat transfer correlations listed in Table 2.1 are used. However, for the angular variation of the heat transfer correlation, the expression for the mini-ACOPO as proposed in Reference [18] and also used in the INEEL study [19] are used. The temperature and the area of the other structures is assumed to be the same as those of the benchmarking calculations as discussed in Section 2.3.

Figure 4.1 shows the initial condition for the base case. The mean decay heat density is 2.1 MW/m^3 with an upper bound of about 3 MW/m^3. The shape of the uncertainty distribution for the steel mass shown in Figure 4.1b is due to the dependence of the steel mass on the UO_2 mass relocation as was discussed in Section 3.1.4. Furthermore, the base case analyses assume a two-layer configuration of ceramic pool with an overlaying metallic layer (i.e., Configuration I).

The ratio of the local heat flux to CHF is shown in Figure 4.2. The distributions are shown at three locations: (1) at the bottom of the vessel, (2) at the top of the oxide layer adjacent to the metal layer, and (3) in the metal layer. Note that the height of the oxide layer varies with the mass of the debris in the lower plenum as shown in Figure 4.1b. Therefore, the top of the oxide layer is not at a fixed angle (the angle varies between 63^o and 79^o depending on the mass). However, since the maximum heat flux in the oxide layer occurs at the top, the distribution shown in Figure 4.2 signifies the maximum heat flux. At the bottom of the vessel (at 0^o), the heat flux is lowest, and even though the CHF is also lowest at this location, the ratio of Q/Q_{CHF} is around 0.2. At the top of the molten oxide layer, the heat flux ratio is significantly increased, but remains below 1. Therefore, the Conditional Failure Probability (CFP) is zero. In the metal layer; however, due to the focusing effect of the heat flux to the side of the vessel, the CFP is 0.15. The heat flux ratio can reach up to 1.5 in the upper bound. Significant melting of the vessel wall is predicted both in the top metallic layer region, and near the top of the molten oxide layer. No melting of the vessel wall is predicted at the bottom of the vessel.

Table 4.1 Uncertainties in the emissivity of surfaces and the vessel thermal conductivity

Physical Property	Mean	Standard Deviation
Vessel thermal conductivity (W/m-K)	32	2
Metal emissivity	0.29	0.04
Structure emissivity	0.8	0.03

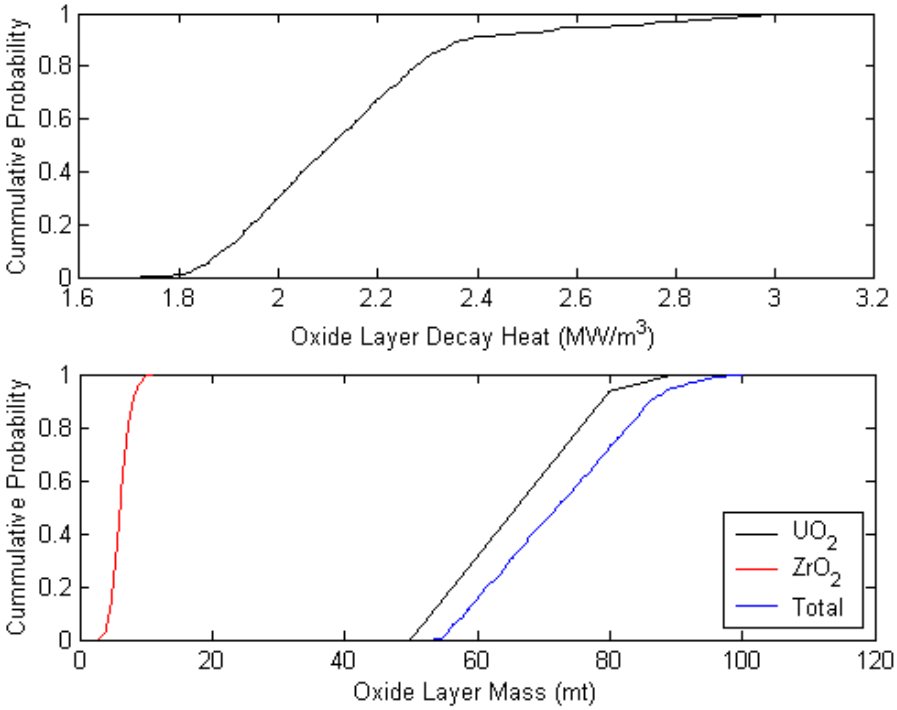

Figure 4.1a Base case distribution of initial conditions

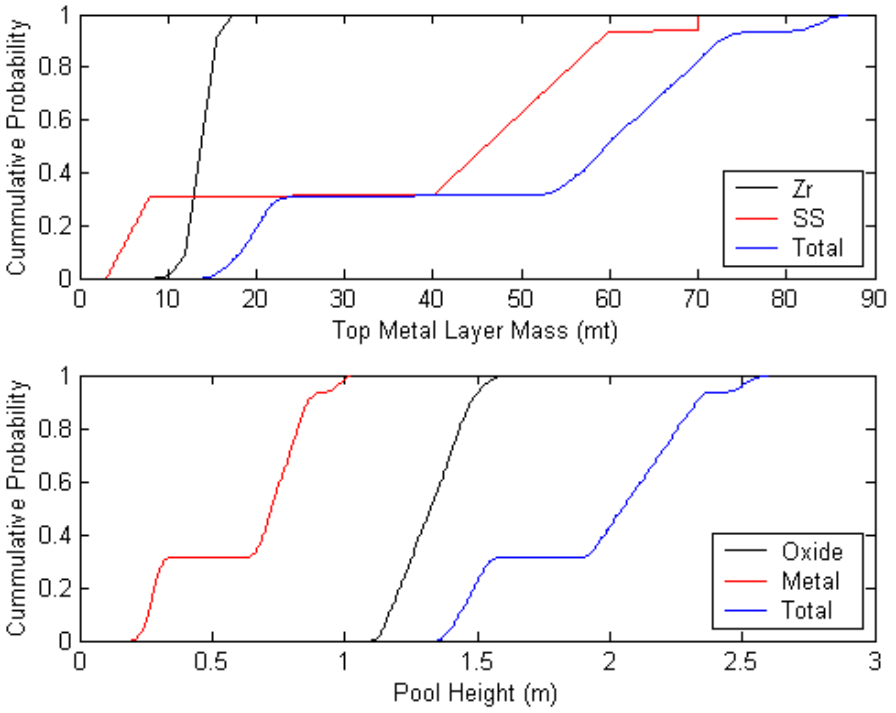

Figure 4.1b Base case distribution of initial conditions (continued)

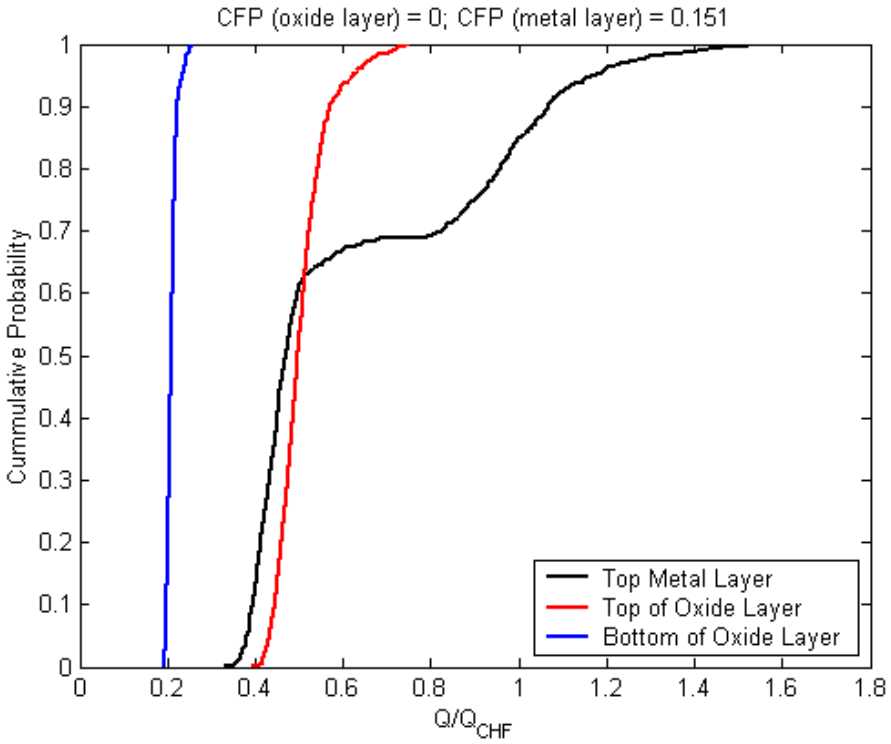

Figure 4.2 Base case distributions of output parameters

Figures 4.3 and 4.4 show the distributions of the oxide layer crust thickness, the heat flux ratio to water, the heat flux ratio, and the vessel wall thickness as a function of the angle for a single realization of the input parameters. For Figure 4.3, the mean values of the distributions are used. This corresponds to 66,266kg of UO_2, 6,211kg of ZrO_2, 13,714kg of Zr, and 37,376kg of steel. For Figure 4.4, only the lower bound masses are used, and other parameters are the same as those for Figure 4.3. The masses for Figure 4.4 are 50,000kg of UO_2, 6,307kg of ZrO_2, and 3,000kg of steel (note that there is no Zr in the light metal layer). Note that in the steel layer in Figure 4.4, the heat flux to the cavity water is more than four times larger than the critical heat flux, which is due to the focusing effect of the top steel layer.

4.3 Sensitivity Analysis

A number of sensitivity calculations are performed in this section to examine the impact of the initial conditions, and the heat transfer correlations on the conditional failure probability of the vessel lower head.

The list of the sensitivity calculations is given in Table 4.2. The largest impact on the conditional failure probability is due to the focusing effect associated with the low mass of debris in the lower plenum. The CFP is decreased by a factor of four from 0.15 to 0.04 for a reduction in the probability from 0.0193 to 0.0046 (see Figure 3.3). For the case of the material properties in the sensitivity calculation, the point estimate mean values are used. The material properties distributions have minimal impact on the estimated CFP. The sensitivity case involving the heat transfer correlations shows that the CFP is within 30% of that using the base case correlations.

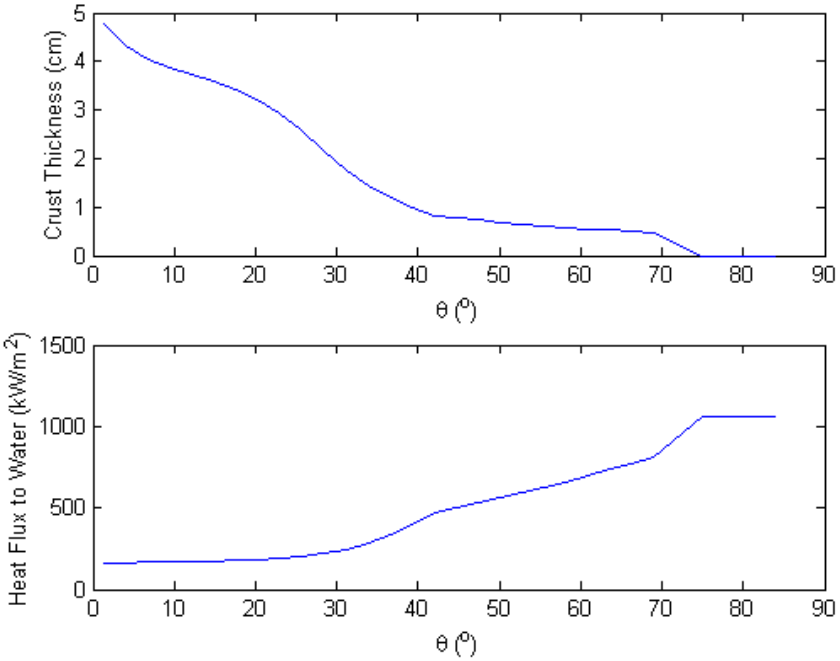

Figure 4.3a Base case angular variation for mean values of parameters (Case 1)

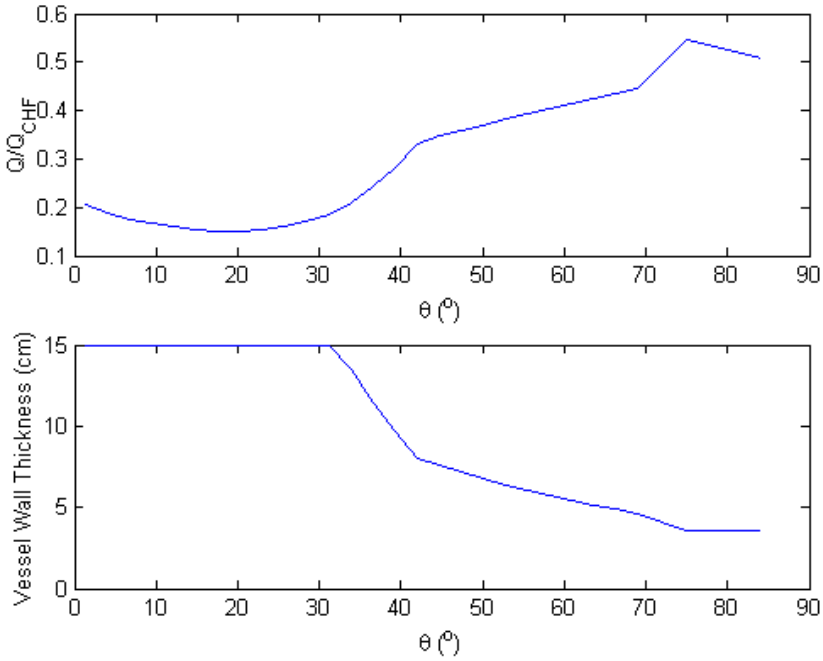

Figure 4.3b Base case angular variation for mean values of parameters (Case 1) (continued)

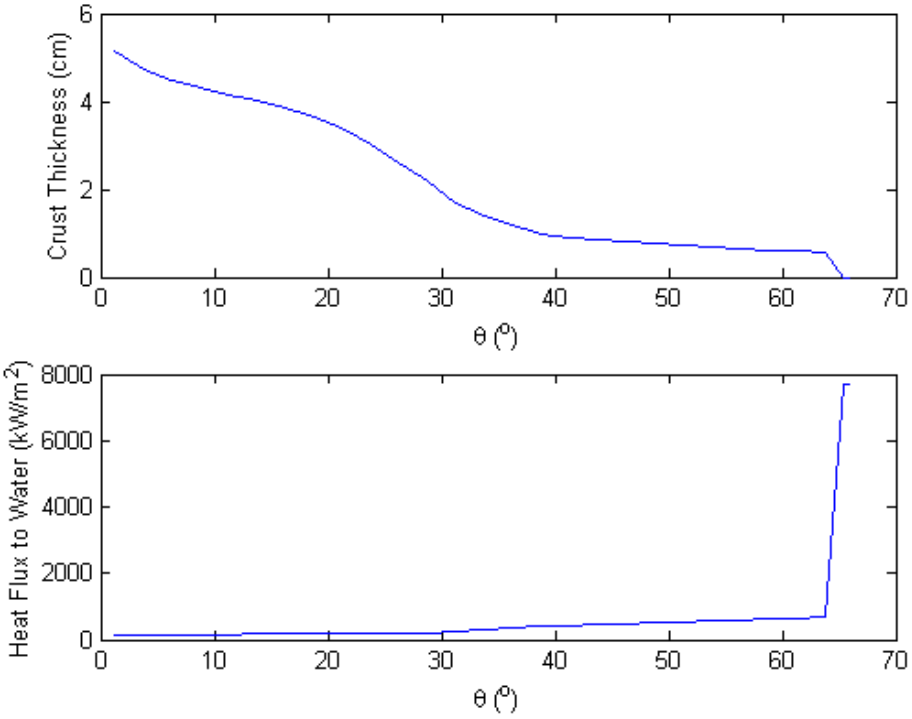

Figure 4.4a Base case angular variation for low melt mass (Case 1)

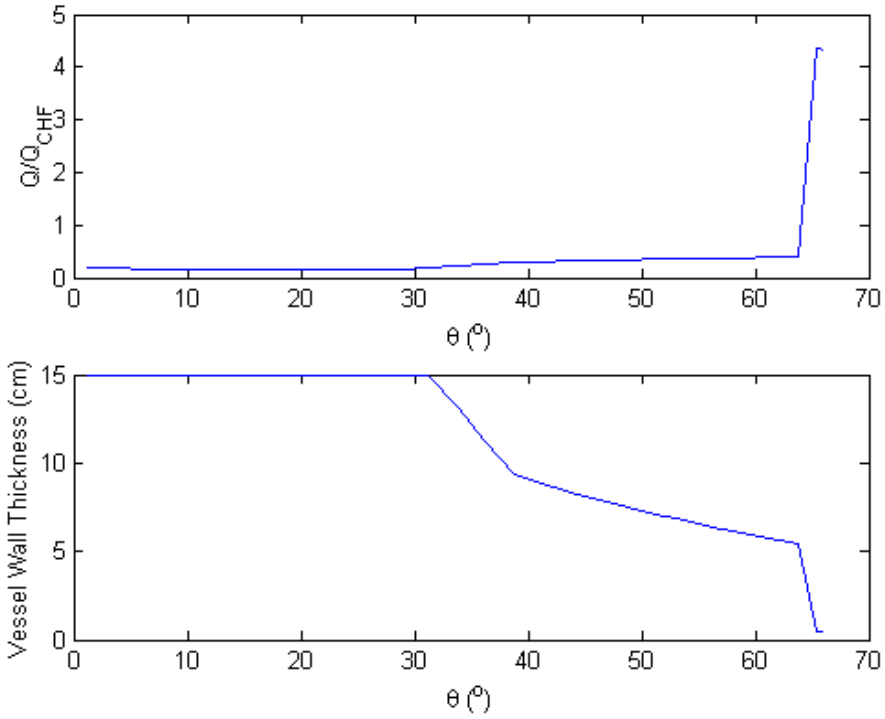

Figure 4.4b Base case angular variation for low melt mass (Case 1) (continued)

Table 4.2 Comparison of lower head conditional failure probabilities (CFP)

Case	Description	Ceramic Layer CFP	Metal Layer CFP
In the Absence of Decay Heat in the Light Metal Layer			
1	Base case	0	0.15
2	DOE heat transfer correlations	0	0.20
3	Heat transfer correlations used in the INEEL study	0	0.30
4	Material properties	0	0.16
5	Reduce probability of low UO_2 mass	0	0.04
6	"Tails" of uncertainty distributions	0	0.16
7	Assumed ±10% uncertainty in CHF correlation	0	0.08-0.25
8	25% increase in heat transfer coefficient (oxide to light metal layer)	0	0.17
Including Decay Heat in the Light Metal Layer			
1D	All other conditions identical to Case 1	0	0.27
2D	DOE heat transfer correlations	0	0.30
3D	Heat transfer correlations used in the INEEL study	0	0.31
4D	Reduce probability of low UO_2 mass	0	0.07
5D	"Tails" of uncertainty distributions	0	0.30
6D	Assumed ±10% uncertainty in CHF correlation	0	0.20-0.31
7D	25% increase in heat transfer coefficient (oxide to light metal layer)	0	0.29

For the decay heat in the top metal layer, the use of Equation (2.32) and the uncertainty distributions associated with Zr oxidation fraction and timing of release discussed in Section 3 show that the fraction of the decay heat can vary between 0.1 and 0.2. In this series of sensitivity calculations (Cases 1D to 7D), a normal distribution is assumed between the lower bound of 0.1 and the upper bound of 0.2 for the fraction of the decay heat in the top metal layer (the rest of the decay heat is in the oxide layer). The results show that a combination of the focusing effect and the additional power in the metal layer can increase the likelihood of failure by a factor of 2 for Case 1D, and 1.5 for Case 2D, respectively. However, for the case with the heat transfer correlations as used in the INEEL study (Case 3D), there is no significant increase in the CFP (as compared with the same case without the decay heat in the metallic layer, i.e., Case 3). This result is not surprising, because for the case based on the correlations as used in the INEEL study (Cases 3 and 3D), the fraction of upward heat transfer in the molten oxide pool is greater than for Cases 1 and 1D. At some point, increasing the decay power in the metal layer does not necessarily increase the CFP because of the reduction in the decay heat in the molten oxide pool. In fact, for Case 1D, if the upper bound of the decay heat fraction is increased from 0.2 to 0.9 (results not shown in Table 4.2), there is only a modest increase in CFP (i.e., from 0.27 to about 0.32). The results of these calculations for Cases 1 through 5 and Case 1D are shown in Figures 4.5 through 4.9. The sensitivity cases are identified by broken curves in these figures.

In response to the peer review of the draft version of the present report (See Appendix B), several additional sensitivity calculations were performed.

The first additional sensitivity involves the assessment of the impact of the tails of the uncertainty distributions on the conclusions of the IVR analysis (Cases 6 and 5D). This is not expected to change significantly the overall results of the IVR analysis, and it has no bearing on the FCI analysis. The input distributions are provided in Figures 4.10 through 4.12. The calculated results are shown in Figures 4.13 and 4.14 for the cases with and without the decay heat in the light metal layer. As expected, the tails of the uncertainty distributions associated with the initial conditions do not significantly affect the calculated results. For the case without decay heat in the light metal layer, the failure probability increases from 0.15 (Case 1) to about 0.16 (Case 6), and for the case with decay heat in the top metallic layer, the lower head failure probability increases from 0.27 (1D) to 0.30 (5D).

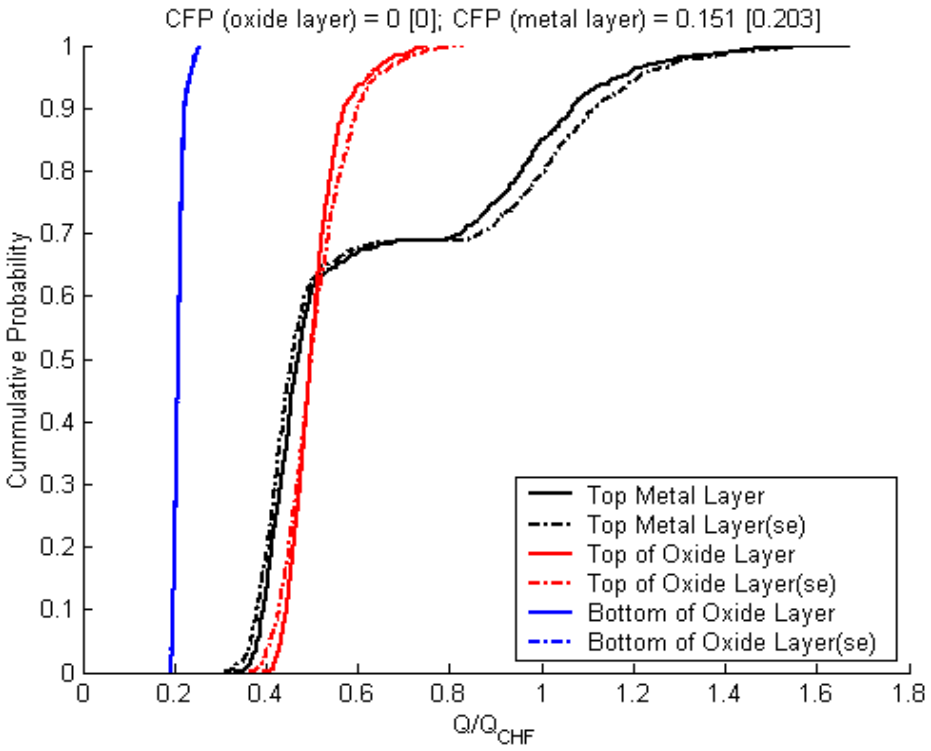

Figure 4.5 Sensitivity to the DOE heat transfer correlations (Case 2)

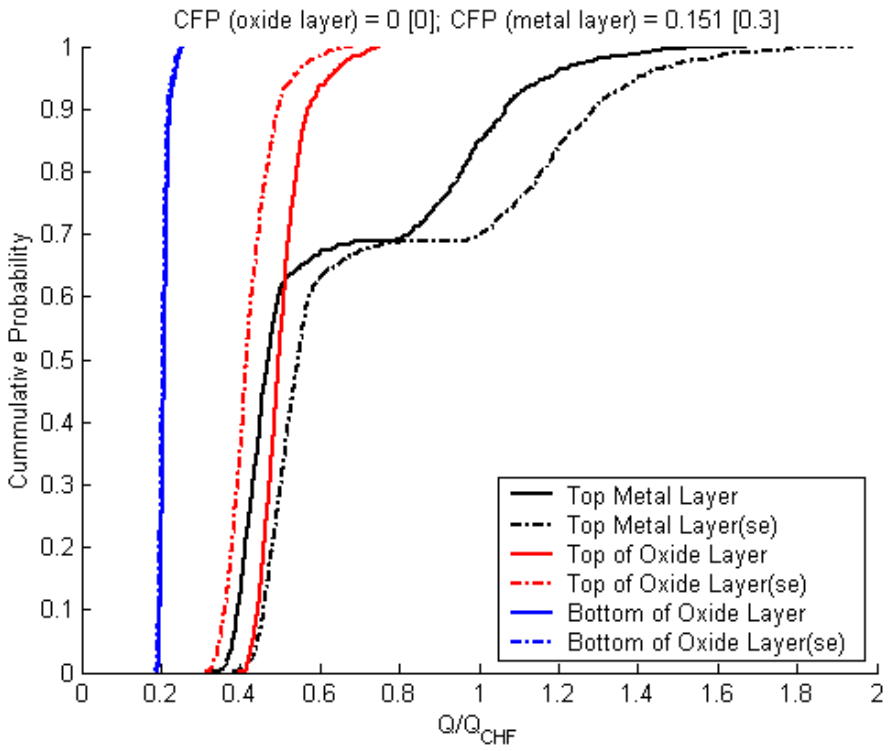

Figure 4.6 Sensitivity to the heat transfer correlations as used in the INEEL study (Case 3)

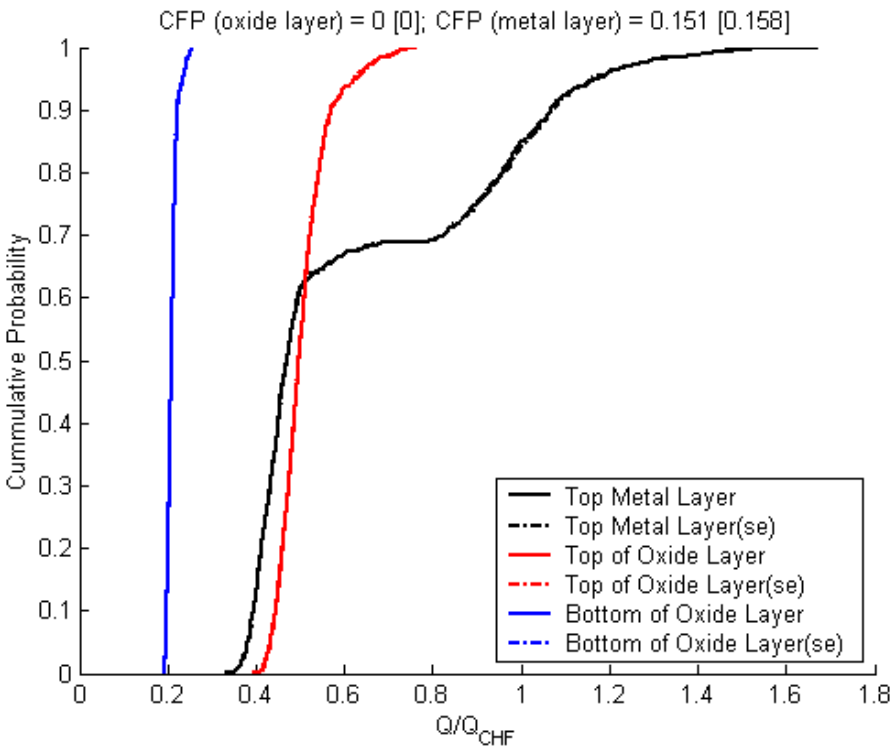

Figure 4.7 Sensitivity to the material properties (Case 4)

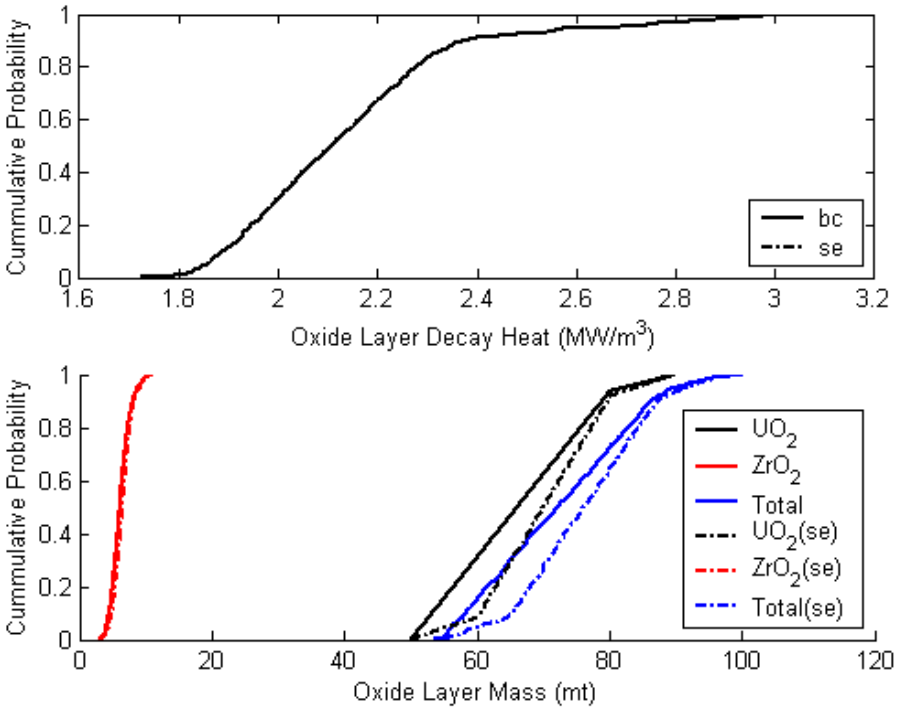

Figure 4.8a Sensitivity to the lower plenum debris mass distribution (Case 5)

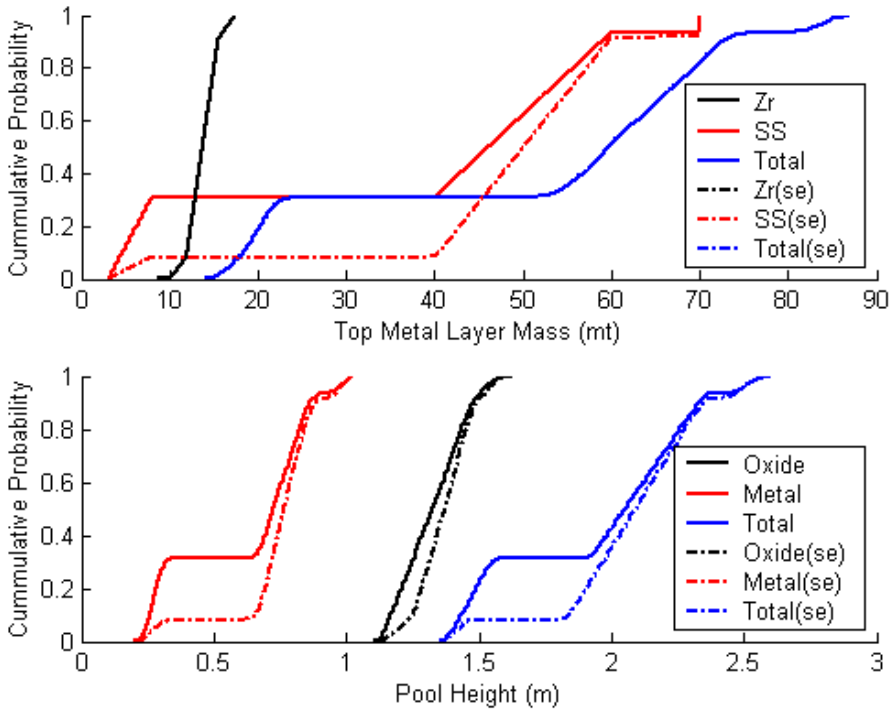

Figure 4.8b Sensitivity to the lower plenum debris mass distribution (Case 5) (continued)

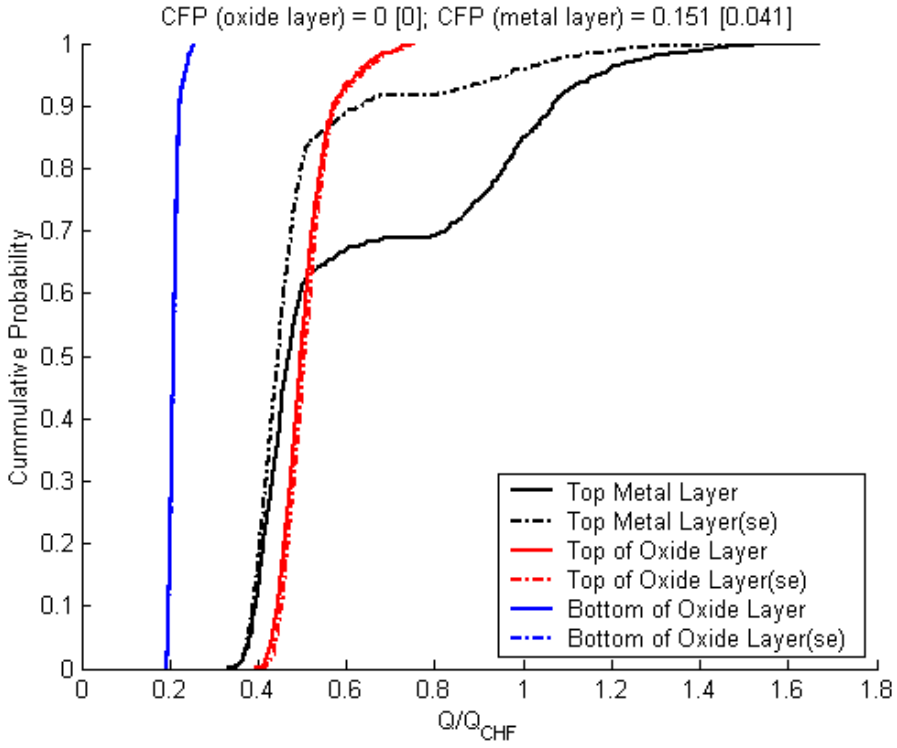

Figure 4.8c Sensitivity to the lower plenum debris mass distribution (Case 5) (continued)

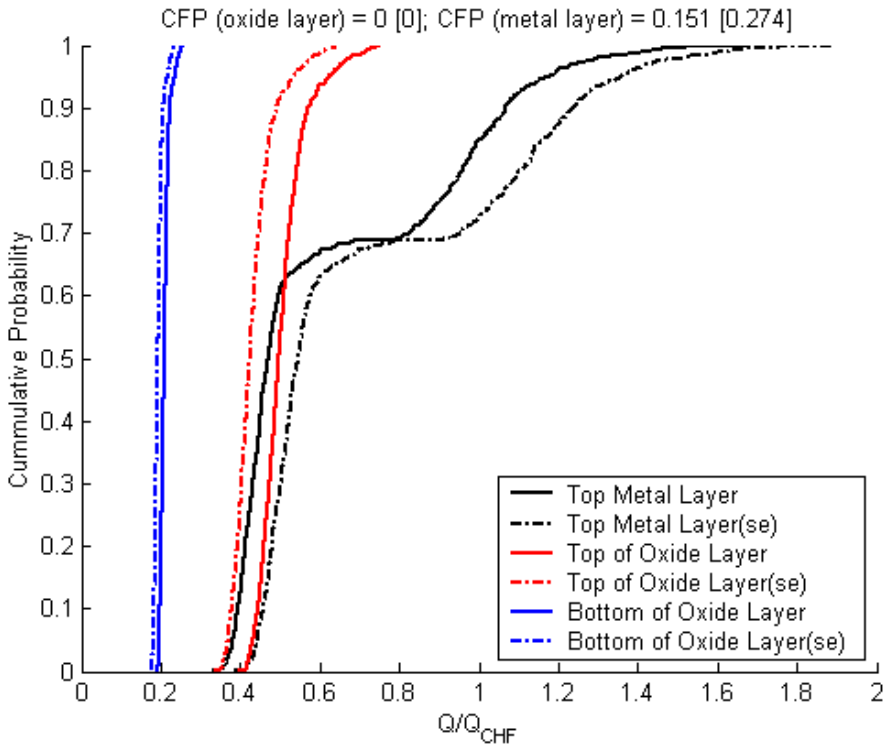

Figure 4.9 Sensitivity to decay heat in the top light metal layer (Case 1D)

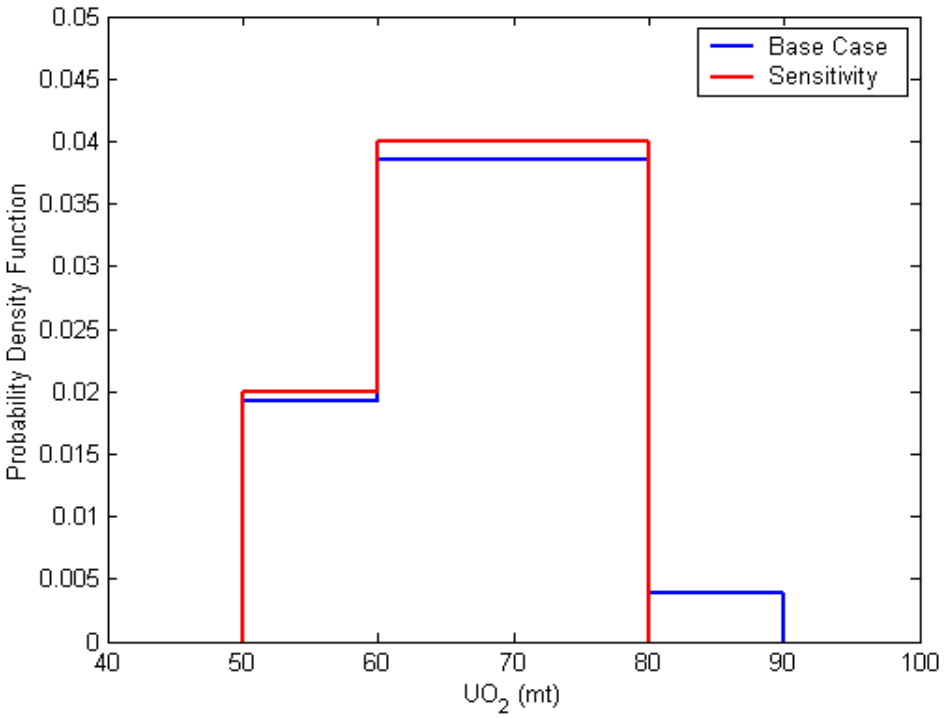

Figure 4.10 Comparison of the distributions of UO_2 for AP1000 (Cases 1 and 6)

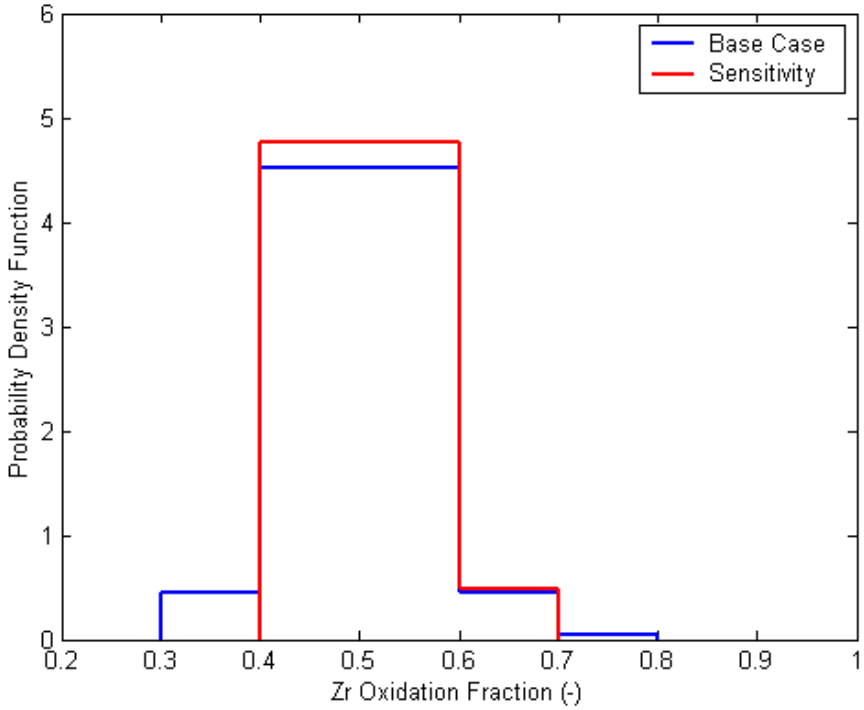

Figure 4.11 Comparison of the distributions of Zr oxidation for AP1000 (Cases 1 and 6)

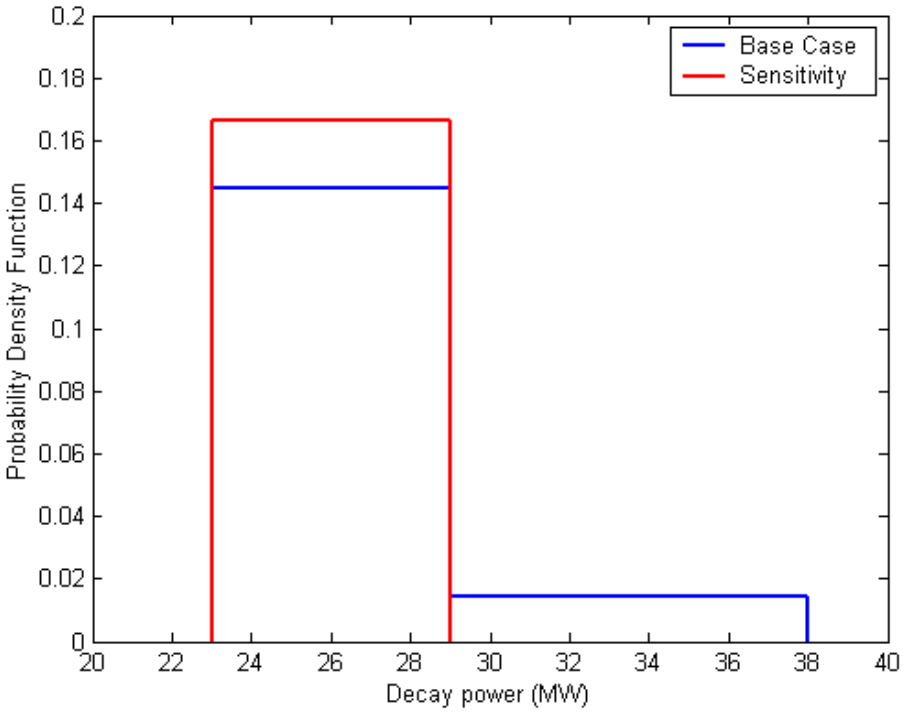

Figure 4.12 Comparison of the distributions of decay power for AP1000 (Cases 1 and 6)

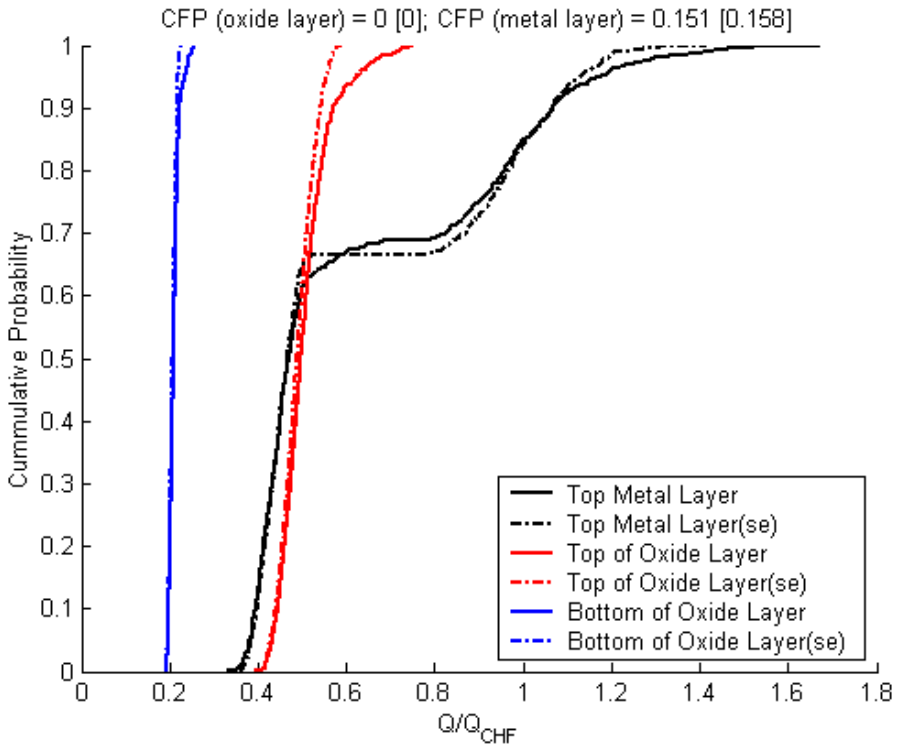

Figure 4.13 Sensitivity to the initial conditions distributions for base case without decay heat in the light metal layer (Cases 1 and 6)

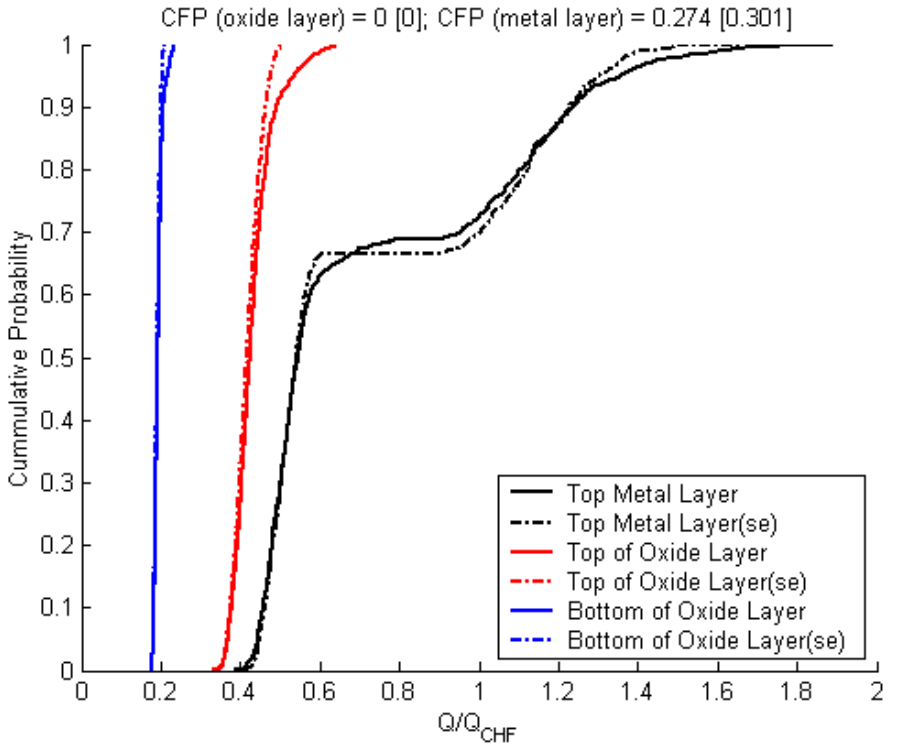

Figure 4.14 Sensitivity to the initial conditions distributions with decay heat in the light metal layer (Cases 1D and 5D)

The second additional sensitivity involves the assessment of the impact of the critical heat flux on the calculated lower head failure probability, even though the uncertainties associated with the measured critical heat flux has not been reported by Westinghouse. This sensitivity calculation involves an arbitrary ±10% variation (see Figure 2.2) in critical heat flux (i.e., Cases 7 and 6D). The calculated results based on this assumed variation are shown in Figures 4.15 and 4.16. As indicated, the uncertainties in the critical heat flux can have a significant impact on the calculated likelihood of lower head failure, and it ranges from 0.08 to 0.25 for the case without any decay heat in the light metal layer (Case 7), and from 0.20 to 0.31 for the case that includes the contribution of decay heat in the light metal layer (Case 6D).

The third additional sensitivity involves the assessment of the impact of the heat transfer coefficient between the ceramic pool and the light metallic layer by arbitrarily increasing the existing Churchill and Chu heat transfer correlation [30] by 25% (i.e., Cases 8 and 7D). Figures 4.17 and 4.18 show the results, where it is seen that the impact on the calculated conditional failure probability is minimal. The calculated failure probability increases from 0.15 (Case 1) to about 0.17 (Case 8) for the case without any decay heat, and from 0.27 (Case 1D) to about 0.29 (Case 7) for the case with decay heat in the light metallic layer, respectively.

The variations in the failure probabilities for these three cases are within the range of values for the other sensitivity cases as listed in Table 4.2. Therefore, even in the absence of material interactions (e.g., Fe-Zr reaction), the side failure of the lower head is likely.

4.4 Results for Melt Configuration II

Experiments performed at the OECD MASCA facility have shown the potential for partitioning of the major constituents (Zr, Fe, U) between oxide and metallic phases and the migration of metals though corium debris. This partitioning has also been studied at larger ratio of steel to corium mass content [39]. The potential for melt partitioning has also been discussed by Powers [40].

Therefore, consistent with these observations, Configuration II involves a molten oxide layer between a heavier metal layer at the bottom, and a lighter metal layer at the top. It is important to recognize that the density of the bottom layer composed of U-Zr-SS must be greater than the density of the oxide layer. Since the density ratio is the limiting factor, it is only possible to perform parametric calculations for this configuration by ensuring that the density ratio is greater than 1 and the mass fraction of the uranium remains below the maximum value of 0.40[4] [18-19]. It should also be noted that there is no experimental database for the heat transfer in this configuration.

The parametric calculations involve point estimate mean values of the masses from Configuration I as discussed in the previous sections. For simplicity, the mass fraction of uranium is fixed at 0.4 [19], and only the fraction of uranium is allowed to vary. The fraction of uranium that is in the oxide form (f_U) is defined as:

$$f_U = 1 - \frac{m_U}{M_{UO_2}} \frac{270}{238} \tag{4.2}$$

where M_{UO_2} is the total mass of UO_2, and m_U is the mass of uranium in the bottom layer. Therefore, the mass of U in the bottom heavy metal layer, and the mass of UO_2 in the ceramic layer are then given by:

$$\begin{aligned} m_U &= \left[(1 - f_u) M_{UO_2}\right] \frac{238}{270} \\ m_{UO_2} &= f_u M_{UO_2} \end{aligned} \tag{4.3}$$

The mass of ZrO_2 in the oxide layer is fixed, and the mass of steel in the bottom heavy metallic layer is only the lower plenum energy absorbers (3,000 kg). The mass of Zr in the bottom layer, and the mass of Zr in the top layer are[5]:

$$\begin{aligned} m_{Zr-bot} &= 1.5 m_U - 3000 \\ m_{Zr-top} &= M_{Zr} - m_{Zr-bot} \end{aligned} \tag{4.4}$$

Here, M_{Zr} is the total mass of Zr.

Table 4.3 shows the conditions for the parametric calculations.

---

[4] Based on the comments as discussed in References [18] and [19].

[5] Since the mass fraction of U is 0.40:

$$\frac{m_U}{m_{Total}} = 0.40$$

and

$$m_{Total} = m_{Zr-bot} + m_{Fe} + m_U$$

Therefore:

$$m_{Zr-bot} = 1.5 m_U - m_{Fe} = 1.5 m_U - 3000$$

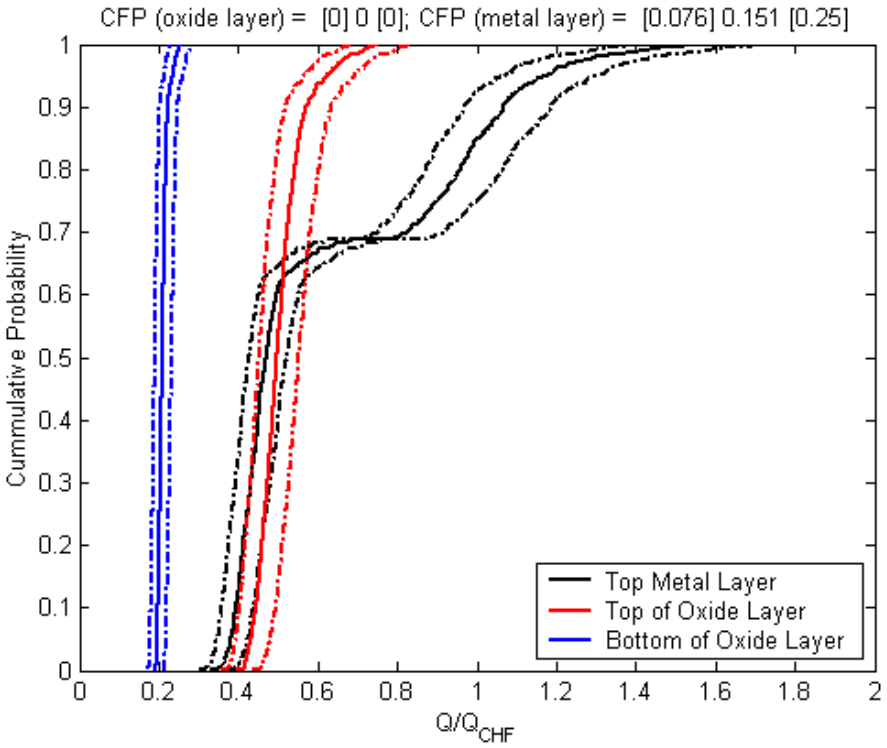

Figure 4.15 Sensitivity to the uncertainties in the critical heat flux for the base case without decay heat in the light metal layer (Case 7)

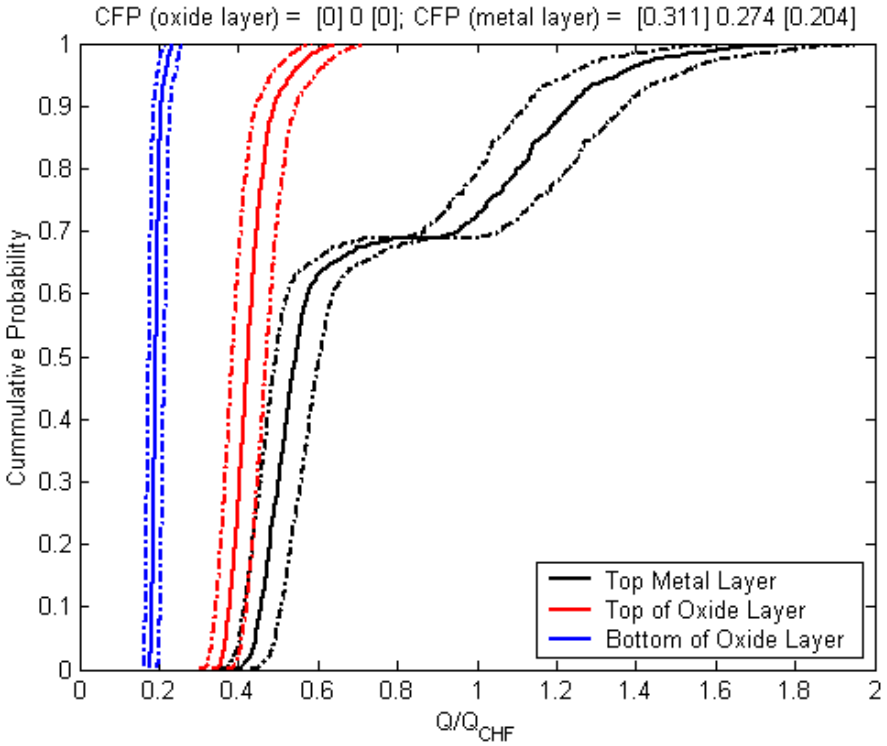

Figure 4.16 Sensitivity to the uncertainties in the critical heat flux with decay heat in the light metal layer (Case 6D)

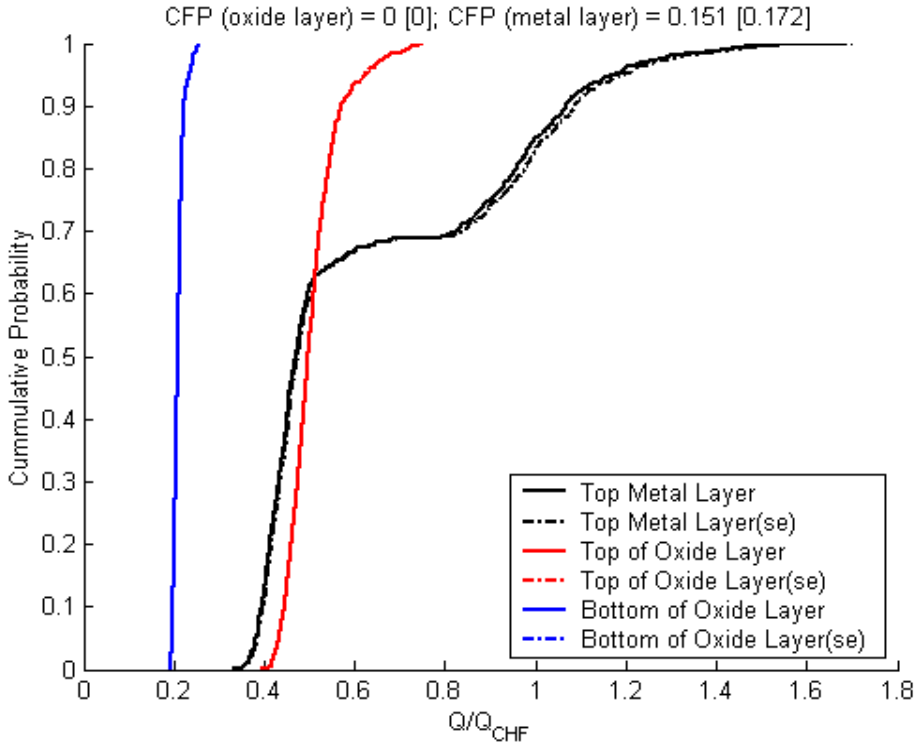

Figure 4.17 Sensitivity to the Churchill and Chu correlation without decay power in the metal layer (Case 8)

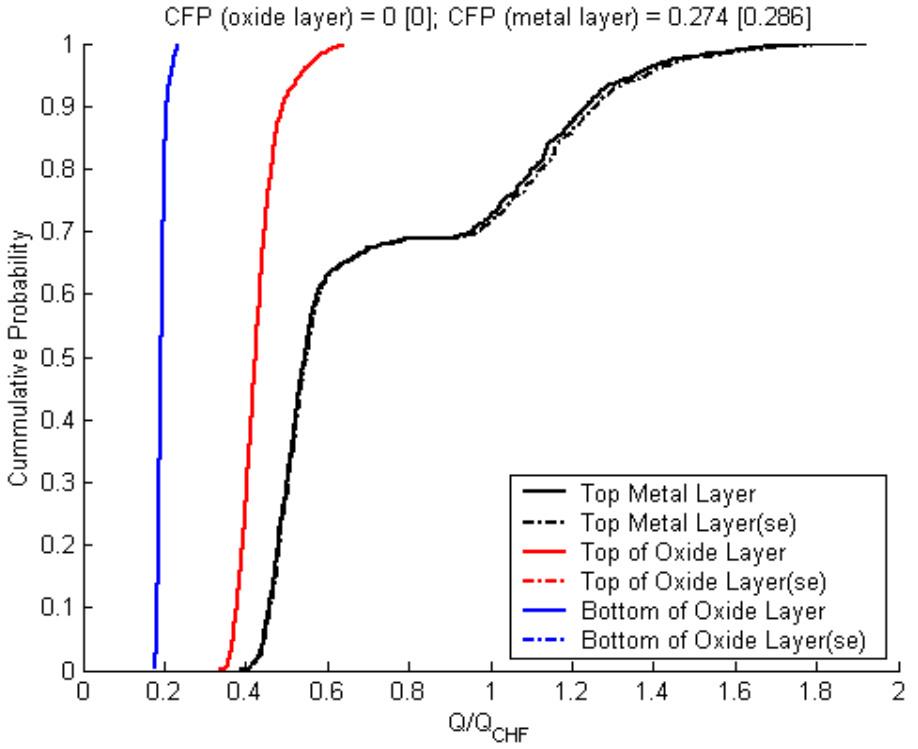

Figure 4.18 Sensitivity to the Churchill and Chu correlation with decay power in the metal layer (Case 7D)

Table 4.3 Melt quantities in each layer for Configuration II

Layer	U	UO_2	Zr	ZrO_2	Fe
Top metal (kg)	-	-	Eq. (4.4)	-	34,366
Middle oxide (kg)		Eq. (4.3)	-	6,211	-
Bottom metal (kg)	Eq. (4.3)	-	Eq. (4.4)	-	3,000
Total (kg)	-	66,266	13,714	6,211	37,366

Table 4.4 Results of parametric calculations for Configuration II

f_U	0.95		0.9		0.85	
m_U(kg)	2,921		5,841		8,762	
m_{UO2} (kg)	62,953		59,639		56,326	
ρ_h (kg/m^3)	8909		8584		8481	
ρ_o (kg/m^3)	8392		8377		8358	
V_h (m^3)	0.820		1.701		2.583	
$A_{h,b}$ (m^2)	4.69		6.86		8.56	
$\Delta h_{h,b}$ (m)	0.373		0.546		0.681	
V_o (m^3)	8.240		7.861		7.481	
Decay heat	Eq (2.30)	Eq (2.31)	Eq (2.30)	Eq (2.31)	Eq (2.30)	Eq (2.31)
Q_h (MW/m^3)	1.126	1.029	1.084	0.9915	1.071	0.978
Q_o (MW/m^3)	2.127	2.137	2.112	2.132	2.096	2.128
Q/Q_{CHF}	0.22	0.20	0.30	0.28	0.36	0.33

The results of the calculations are shown in Table 4.4. It is seen that the calculation of the partitioning of the decay heat between the ceramic and the heavy metal pools using Equations (2.30) and (2.31) yield results that are very similar. The heat flux ratio for all the calculations is well below 1.

Therefore, in the absence of inter-metallic reactions, it appears that the lower head is not expected to fail at the bottom location, if partitioning of the heavy metals from the ceramic pool is conjectured. This conclusion is consistent to that of Reference [33].

4.5 Potential Impact of Inter-metallic Reactions

In Section 4.4 it was shown that the partitioning of U-Zr-SS could result in the formation of a heavy metal layer in contact with the bottom portion of the reactor pressure vessel. Analyses performed in Section 4.4 showed that the thermal failure of the lower head is not likely due to the significant margin to critical heat flux. However, these analyses did not consider the potential for inter-metallic reactions [40], including the reaction of molten Zr with the molten stainless steel resulting in significant heat generation, which at sufficiently high Zr mole fractions, the heat of mixing can result in a self-propagating attack on the lower head [40]. It is noted that the additional steel that is ablated from the lower head tends to mitigate this self-propagating effect (by reduction in the heat of mixing due to a reduction in the mole fraction of Zr in the mixture). Furthermore, the conditions that can result in the segregation of the heavy metals from the ceramic pools may not be sustainable [39].

Therefore, since the potential for vessel failure at the bottom location cannot be dismissed at this time, the failure of RPV at the bottom location is conjectured as part of specifications in Section 5 that are analyzed in Section 6.

5. INITIAL CONDITIONS FOR ANALYSIS OF EX-VESSEL FUEL COOLANT INTERACTION

The delineation of the initial conditions involves the specification of the quantity, the composition, and the temperature of the molten debris in the lower plenum at the time of vessel breach; the mode, the size, and the location of the lower head failure; the RCS and the containment pressures at vessel breach; and the depth and the temperature of water in the reactor cavity.

5.1 Melt Initial Conditions in the Lower Plenum at Vessel Breach

The quantification of molten debris mass, composition and temperature in the lower plenum at vessel breach depends primarily on the accident scenario. The time scale for FCI is very short (less than a second) and would not involve the entire mass of the molten debris in the lower plenum.

A discussion of the initial conditions for the melt in the lower plenum was provided in Section 3. Based on the results of Section 4, the most likely failure of the RPV lower head is expected to occur in the light metallic layer due to the focusing effect that results in the local heat flux to exceed the critical heat flux.

The best estimate melt temperature for the metallic layer is about 2167K based on the results of the IVR model as described in Section 2. This temperature is achieved for a low steel mass of 3,000 kg. For a higher steel mass of 8,000 kg, the bulk temperature is 1960 K. Therefore, the base case analysis assumes a melt pour temperature of 2060K (i.e., ~[2167+1960]/2).

5.2 Cavity Condition at Vessel Breach

The AP1000 containment design transfers all primary system liquid inventories into the In-containment Refueling Water Storage Tank (IRWST) compartment or the reactor cavity during accident conditions. Under LOCA-type conditions, the water that enters the loop compartments (e.g., Steam Generator rooms) is separated from the remainder of the containment regions by the compartment walls. However, water can flow along the compartment floor (2.5 m above vessel zero) through the cavity man-way to the cavity floor (1.0 m below vessel zero). Under transient (non-LOCA) conditions, water drainage into the cavity follows a different path. Assuming loss of passive residual heat removal system, the primary system fluid is discharged to the IRWST through the depressurization spargers located within the IRWST. The IRWST water can overflow to the refueling room, and water from the refueling room drains to the cavity through a normally opened refueling canal valve (the drain line is located at the elevation of 2.95 m above vessel zero). For this drainage to occur, the normal water level in the IRWST (17.4 m above vessel zero) should rise to the 17.62 m to overflow the water to the refueling room.

Water delivery directly from the IRWST to the cavity region (without injection into the RPV or the refueling room) can also be achieved through operator action by opening the motor operated valves on the two IRWST drain lines. The Passive Containment Cooling System (PCS) is designed to serve as the ultimate heat sink for the AP1000 under accident conditions; therefore, any steam generated due to heat removal from the core debris is expected to condense along the containment shell where it is directed back into the IRWST for recirculation into the RPV and/or reactor cavity.

The bottom of the RPV is located 1 m above the cavity floor [9]. If the entire inventory of RCS, Core Makeup Tanks (CMTs) and accumulators are deposited into the steam generator compartments and the cavity region, the height of water pool in the cavity would be about 3.2 m above the cavity floor, and the RPV lower head will be fully submerged. In addition, if IRWST cavity injection were successful, the height of the water pool in the cavity would be 1.2 m above the hot leg centerline; resulting in the submergence of the RPV.

The water level inside the cavity increases rapidly for scenario 3BE [35] resulting in the submergence of the hemispherical lower head in a very short time frame (0.03 hour). Reference [35] also shows that at the time of core relocation into the lower plenum, the depth of the water in the cavity is about 5.72 m (i.e., full submergence of the RPV).

5.3 Location, Mode and Size of Vessel Breach

The failure location impacts the dynamic pressures and the impulsive loads on the cavity wall and the reactor pressure vessel, especially if the failure location is on the side of the vessel lower head and in the vicinity of the cavity wall. According to the results of calculations in Section 4, the best-estimate location of failure is on the side of the lower head in the light metallic region.

The size of failure cannot be estimated with any degree of certainty. The results of the in-vessel retention analysis discussed previously shows that the thickness of the metallic layer can be over 0.35 m before the critical heat flux is exceeded (for 80 mt of UO_2 from

Figure 3.3 and decay heat of 29 MW from Figure 3.1). Therefore, as a best estimate, a failure hole diameter of 0.4 m is assumed for the base case calculation. Using the upper bound values of 90 mt of UO_2 from Figure 3.3 and decay heat of 38 MW from Figure 3.1, the metallic melt layer thickness can be as high as 0.53 m before the critical heat flux is exceeded. Therefore, a sensitivity to a larger hole size of 0.6 m is also considered.

Furthermore, to assess the potential impact of RPV failure at the bottom location (e.g., due to materials interactions effects), a sensitivity case that involves RPV failure at the bottom of the reactor pressure vessel (assuming a failure size of 0.4 m) is also considered.

5.4 Containment Pressure and Temperature at Vessel Breach

The results of the MELCOR calculations for scenario 3BE [35] indicate that the containment pressure is about 2 bar and the cavity water is subcooled at a temperature of about 343K following core relocation into the lower plenum. This calculation shows that the cavity water remains subcooled for several hours following ceramic pool relocation into the lower plenum. The summary of the base case conditions is provided in Table 5.1.

5.5 Ex-Vessel FCI Calculation Matrix

For the AP600 ex-vessel fuel coolant interaction analysis, three levels of RPV submergence were considered, a low reactor cavity water level of 1.3 m (unsubmerged RPV), medium reactor cavity water level of 2.5 m (partially submerged RPV), and high reactor cavity water level of 9 m (fully submerged RPV). For the AP1000 analysis, only the case of the deeply flooded cavity is considered (5.72 m for scenario 3BE) since this case is expected to be most challenging. The melt discharge is assumed to be gravity-driven. The melt discharge velocity is estimated based on the thickness of the melt layer that results in the critical heat flux. A light metal layer thickness of 0.35 m would result in a pour discharge velocity of about 1.7 m/s.

There are a number of uncertainties in severe accident progression and fuel coolant interaction modeling. The uncertainties can be classified into the following two groups:

- **Variability in melt progression (initial conditions)**: The variability in melt progression impacts the melt pour composition and the RPV failure size. In the present analysis, it is assumed that a failure of the lower head can lead to a pour of both metallic and ceramic components as a result of failure for thin light metallic layers. Therefore, it is quite possible that the initial pour could involve both metallic and ceramic components. A bottom failure of the lower head representing Configuration II is also postulated as part of the sensitivity calculations.

- **Variability in modeling of fuel coolant interactions**: In the present study, the FCI processes are modeled using the two-dimensional PM-ALPHA [3] and ESPROSE.m [4] computer codes. Uncertainties exist in modeling particle breakup during the premixing phase, and particle fragmentation during the explosion propagation phase. The variability in modeling fuel coolant interactions in the present study is demonstrated by including the parametric effect of particle fragmentation during the escalation phase of the interaction. Table 5.2 lists the sensitivity cases that are intended to assess the impact of variabilities in the particle fragmentation on the calculated dynamic loads.

Table 5.1 Base case conditions

Parameter	Value
Pour Composition	100% Metallic
Lower head failure hole diameter	0.4 m
Pour Temperature	2060K
Pour velocity	1.7 m/s
Containment pressure	2 bar-a
Cavity water temperature	343K

Table 5.2 Summary of the base case and sensitivity calculations

Case	Variation from the base case	Comments
1	Base case scenario	Metallic pour at 2060K, lower head failure size of 0.4 m, melt particle diameter of 0.01 m, and the maximum fragmentation rate per particle of 4 kg/s.
2	Ceramic composition at 3150K	Pour involves ceramic material
3	Failure size of 0.6 m	Larger hole size
4	Particle diameter of 0.10 m and maximum fragmentation rate per particle of 400 kg/s	Larger particle diameter and fragmentation rate
5	Bottom failure of the lower head	Metallic pour (U-Fe-Zr) at 2300K, lower head failure size of 0.4 m, melt particle diameter of 0.01 m, and the maximum fragmentation rate per particle of 4 kg/s.

6. RESULTS OF EX-VESSEL FUEL COOLANT INTERACTION ANALYSIS

The RPV is modeled as an "obstacle" shown in Figure 6.1 that also shows the problem nodalization, the representation of the hemispherical lower head with a number of horizontal and vertical lines, signifying the presence of the obstacles. Only a narrow annular region of thickness 0.4 m is available for the propagation of the explosion around the cylindrical portion of the RPV.

The insulation that surrounds the RPV lower head may potentially affect the fuel coolant mixing process and the subsequent explosion propagation/expansion. The presence of the insulation may have two important effects. During the mixing phase, the insulation could alter the flow of the molten material and prevent efficient fuel coolant mixing. It would restrict the amount of water that could mix with the fuel and actually increase the void fraction of the vapor present in the region near the vessel wall. In addition, after the metallic melt has melted through the insulation, the residual passages in the insulation could trap vapor and provide a certain degree of compliance to the rigid boundary of the RPV outer wall. These two effects of altering the mixing process and providing a larger degree of “boundary compliance” to the RPV wall could diminish the focusing effects of this surface and thereby reduce the dynamic pressures in the local region. However, it is difficult to quantify the impact of the thermal insulation on the dynamic pressure using the available computer codes, especially in light of the uncertainties that are inherent in the fuel coolant interaction phenomena.

For the PM-ALPHA calculation, the melt inlet location is about 2 m above the cavity floor; therefore, the size of the computational domain is 2 m in the vertical direction (20 nodes) and 3 m in the horizontal direction (15 nodes). The last node in the vertical direction represents a steam gap. PM-ALPHA requires the inlet to be at the boundaries of the computational domain, and does not accept an inlet below the surface of the water pool. The PM-ALPHA calculation is only performed to obtain the conditions for the ESPROSE.m explosion propagation simulation. The entire RPV including the cylindrical portion up to a distance of 6 m from the cavity floor is modeled as an obstacle. An additional 1 m of steam gap is also included to allow for the venting of the explosion. The depth of the water pool in scenario 3BE was 5.72 m. It was decided to only model a 5 m pool in the interest of computational time.

6.1 Base Case

The initial distribution of the vapor void fraction and the melt volume fraction based on the ESPROSE.m calculation are shown in Figures 6.2 and 6.3, and as indicated, the water pool subcooling leads to suppression of the vapor void fraction. These conditions are conducive to high pressurization. The duration of the premixing was 1 second to allow the melt to reach the cavity floor before the explosion is triggered.

The propagation of the pressure in the cavity around the RPV is shown at different times in Figure 6.4 (the pressure is in MPa). The water subcooling leads to high pressures in the explosion zone. However, the pressure venting from the top of the water pool around the gap ultimately leads to a reduction in pressure in the water pool.

The explosion is triggered at the bottom of the vessel, and it takes about 1 msec for the pressure to propagate to the lower head. By 2 msec, the pressure in the pool reaches about 80 MPa, and the wave is propagating downward toward the cavity floor and away from the explosion zone. At 5 msec, the pressure wave has already reached the cavity wall away from the explosion zone. The maximum pressure in the cavity pool, and the pressures on the cavity wall are shown in Figures 6.5 and 6.6. The maximum impulse load on the cavity wall is about 85 kPa-s as shown in Figure 6.7. It should be noted that this calculations was run for only 6 msec. The number of nodes for AP1000 calculation is substantially increased because the pool depth is 5 m, and longer time periods involved increased computational resources at minimal benefit. It is clear from the maximum pressure in the pool that by this time, the explosion is slowly dissipating. The pressure traces on the cavity wall at different axial locations show a complicated pattern of multiple reflections and pressure peaks as a result of interaction with the RPV lower head structure.

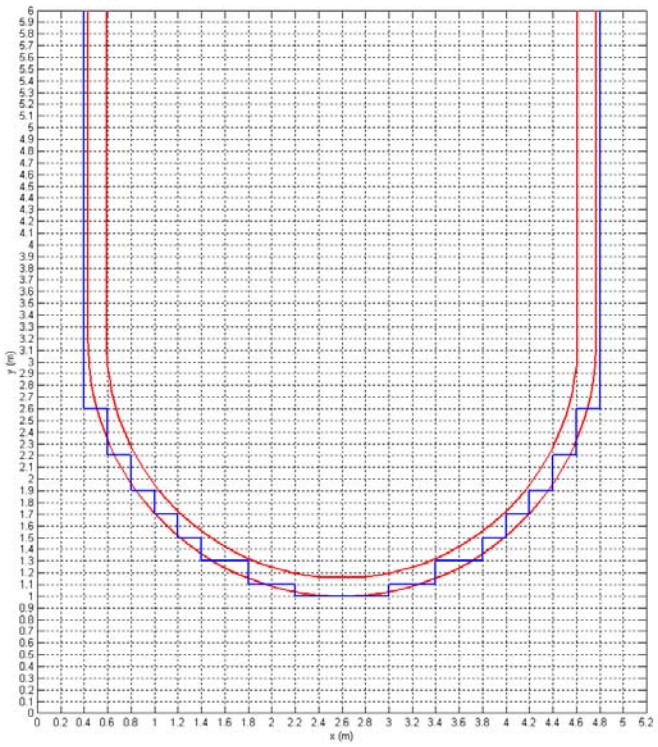

Figure 6.1 Schematic of the lower head nodalization

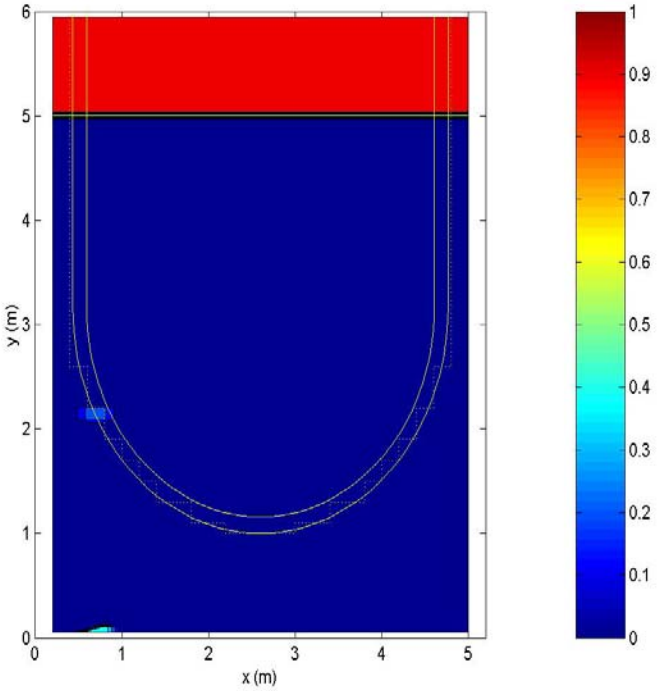

Figure 6.2 Predicted vapor void fraction at 1 second (Base Case)

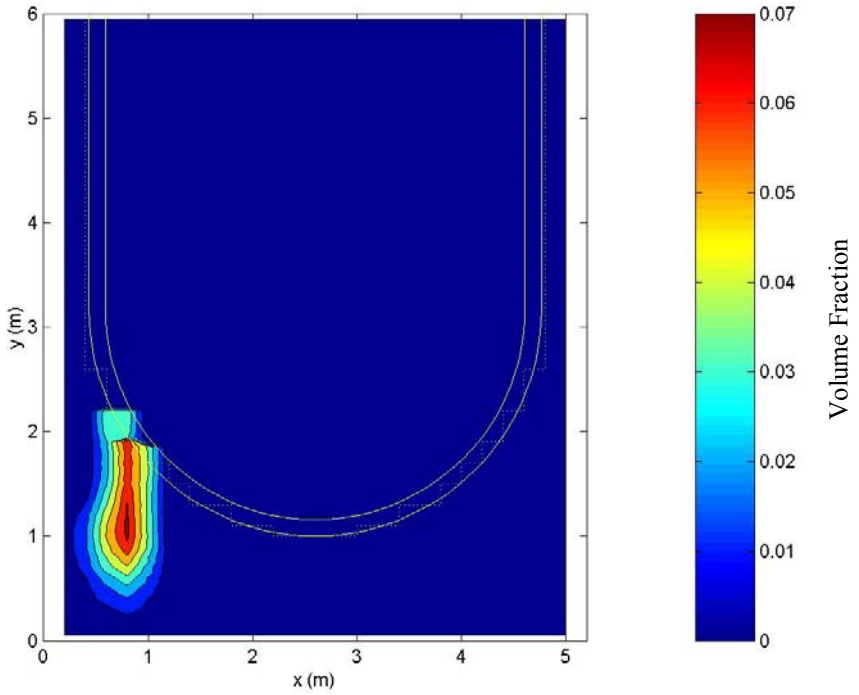

Figure 6.3 Predicted melt volume fraction at 1 second (Base Case)

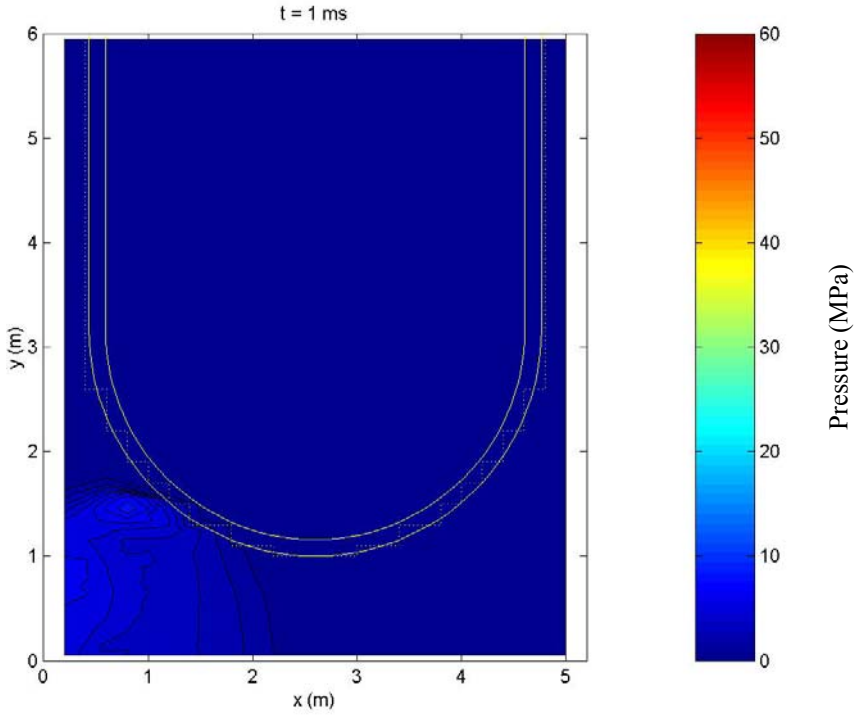

Figure 6.4a Predicted pressure distribution in the cavity at 1 ms (Base Case)

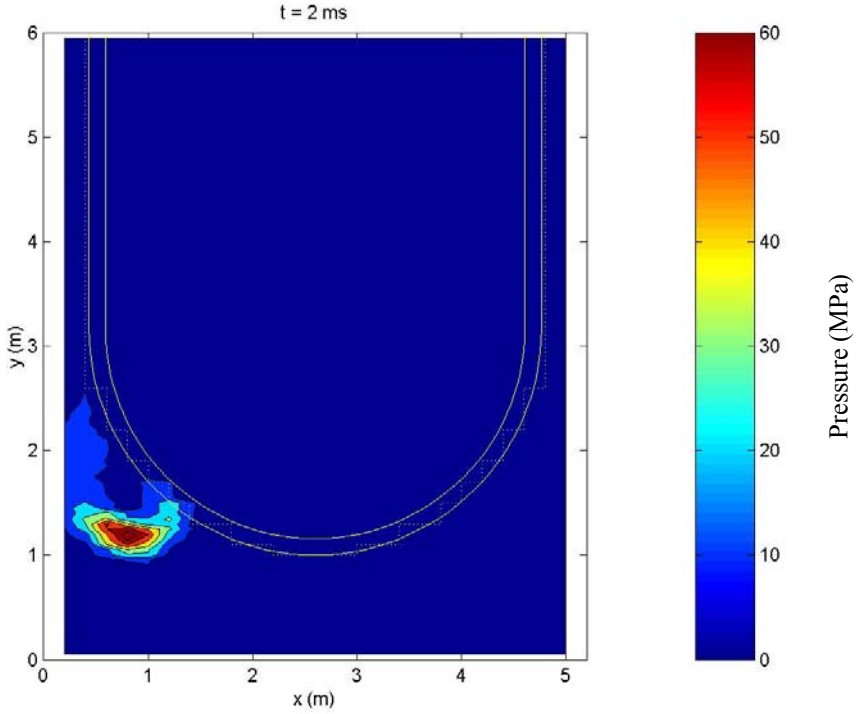

Figure 6.4b Predicted pressure distribution in the cavity at 2 ms (Base Case)

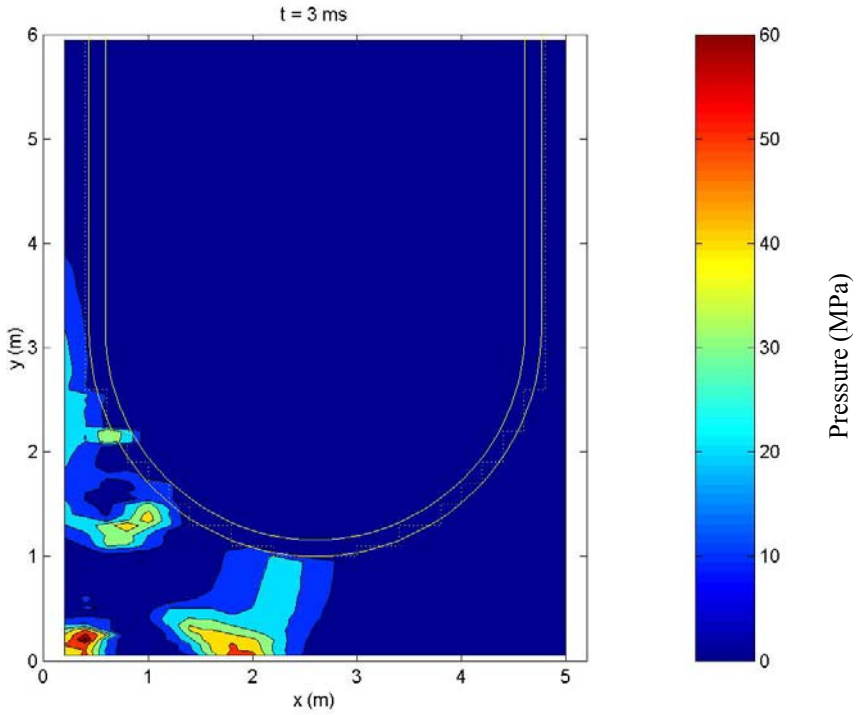

Figure 6.4c Predicted pressure distribution in the cavity at 3 ms (Base Case)

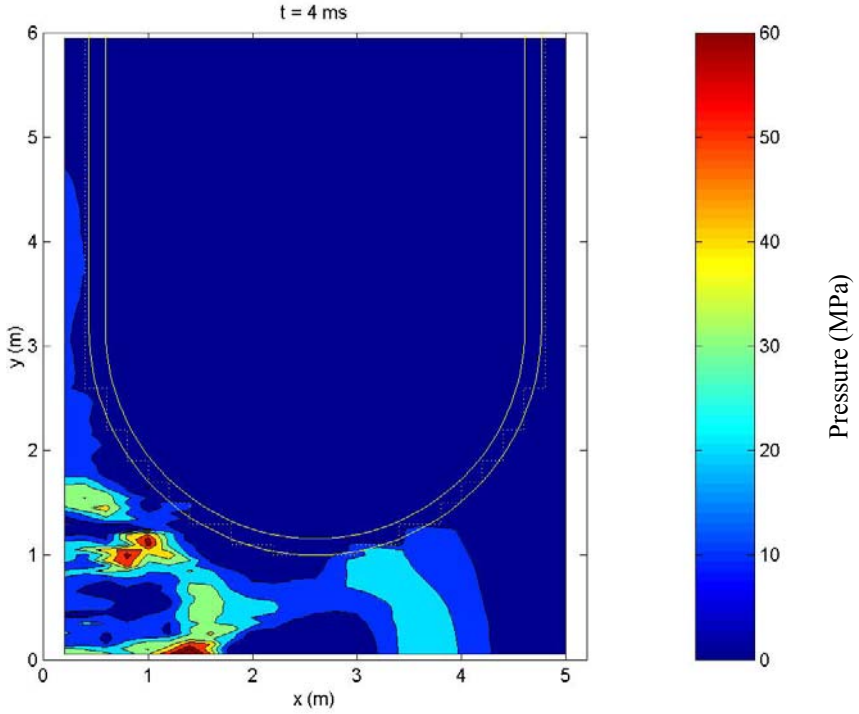

Figure 6.4d Predicted pressure distribution in the cavity at 4 ms (Base Case)

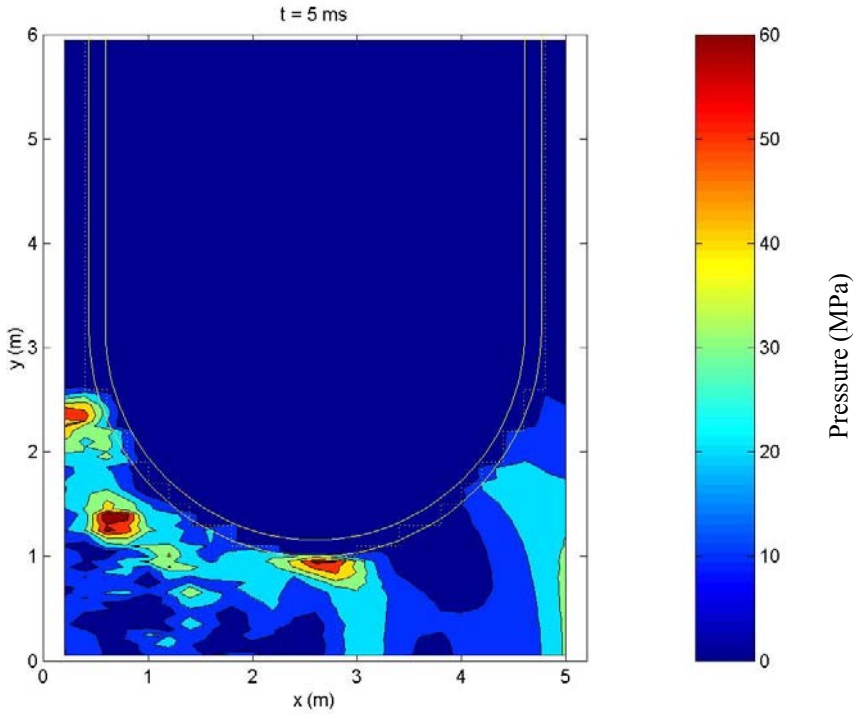

Figure 6.4e Predicted pressure distribution in the cavity at 5 ms (Base Case)

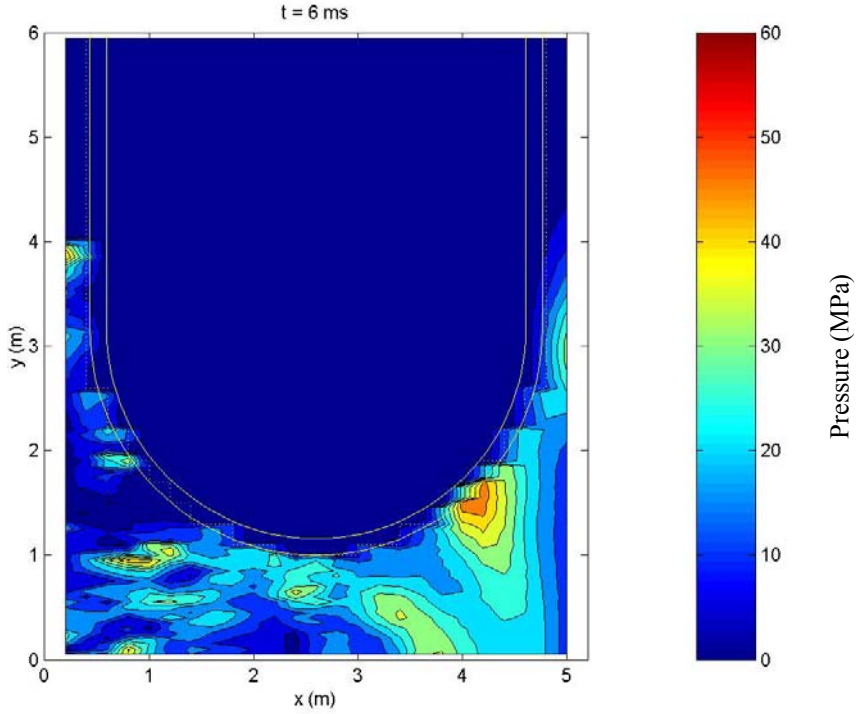

Figure 6.4f Predicted pressure distribution in the cavity at 6 ms (Base Case)

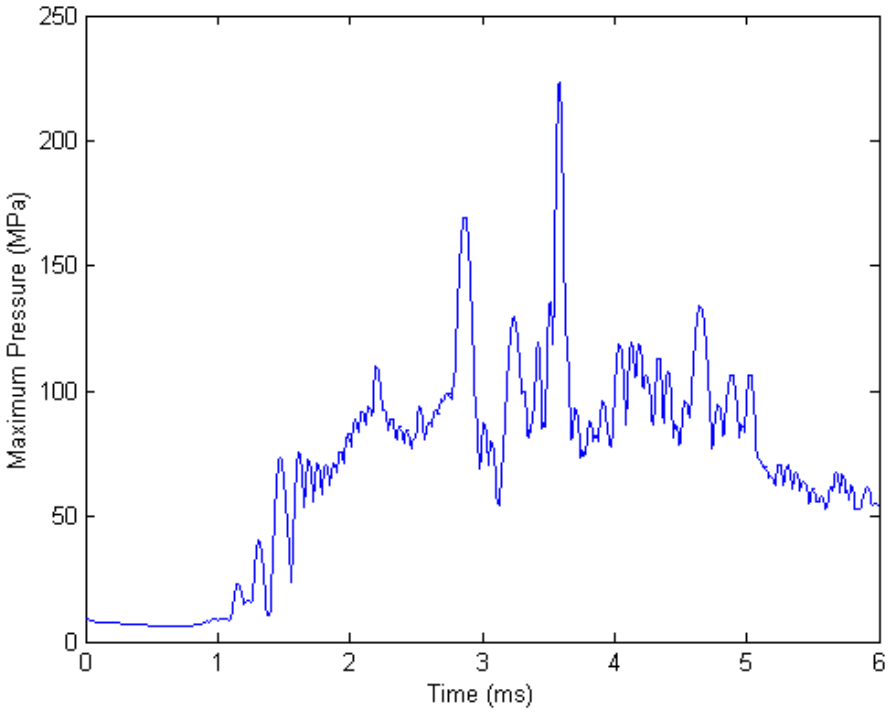

Figure 6.5 Predicted maximum pressure in the pool (Base Case)

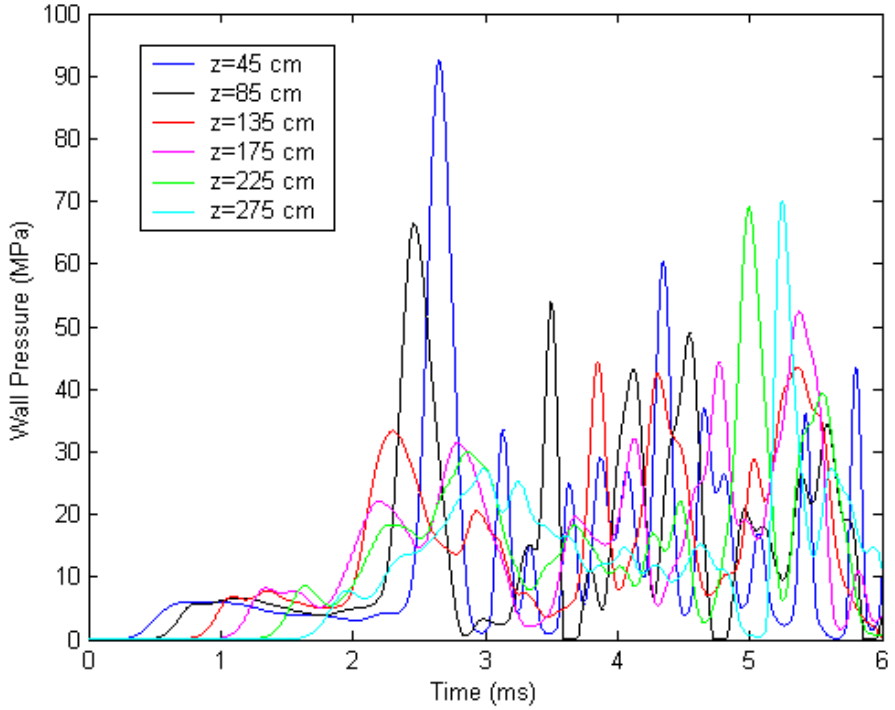

Figure 6.6 Predicted cavity wall pressures at various axial locations (Base Case)

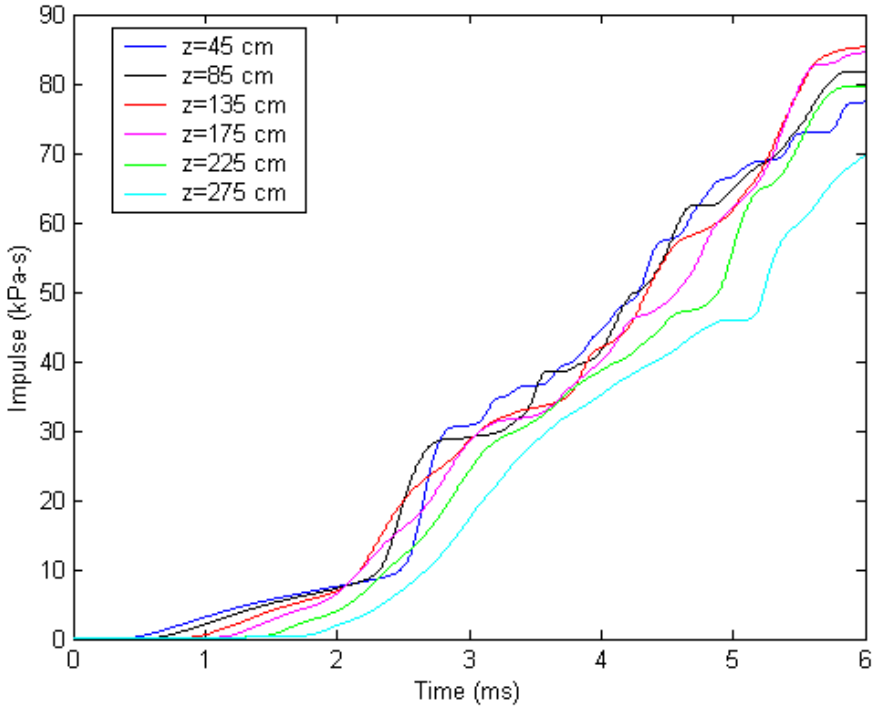

Figure 6.7 Predicted cavity wall impulse loads at various axial locations (Base Case)

6.2 Sensitivity Studies

The results of the sensitivity calculations for AP1000 are discussed in this section. The choice of the sensitivity calculations is based on the results of the AP600 fuel coolant interaction calculations [1] that showed greater sensitivity to certain initial conditions and model parameters. The main difference between the AP600 calculations [1] and the present AP1000 calculations is the assumption of a metallic pour in AP1000 and a ceramic pour in AP600. Because of the focusing effect, a vessel failure is expected to result in relocation of a predominantly metallic material from the lower plenum into the cavity water. The other differences that could possibly affect the explosion energetics are the smaller distance between the bottom of the vessel and the cavity floor in AP1000, and the initial melt pour velocity. Due to the closer proximity of the RPV from the cavity floor, and because the explosions are triggered when the melt reaches the floor, the initial condition for the calculations would involve a lower melt mass (as compared with AP600) participating in the explosion. In addition, the initial melt pour velocity in AP600 [1] was estimated to be 2.9 m/s, whereas for the present AP1000 study, the velocity is 1.7 m/s. Since the pour rate is directly proportional to the velocity, the AP1000 pour rate is estimated to be lower than AP600. Overall, these differences are expected to result in lower pressurization and impulse loading on the cavity wall.

6.2.1 Ceramic Pour

In this sensitivity calculation, the melt composition is assumed to be oxidic. This situation may arise as a result of the side failure of the vessel for a very thin layer of steel where the failure size is large enough so that mostly oxidic material leaves the vessel. As far as ex-vessel fuel coolant interaction is concerned, the oxidic melt composition at a higher temperature (and thus at a higher energy) could pose more severe loads as compared to the base case with the metallic pour and at a lower temperature. The initial melt temperature is estimated at 3150K based on the results of the in-vessel retention analysis for the mean values of the parameters.

It is interesting to compare the results of the AP1000 with the AP600 results (Scenario III with subcooled pool and the RPV modeled as shown in Table 1.1). The AP600 calculations for the case of deeply flooded cavity were run for 10 msec and involved fewer grid points. For AP1000, the number of grid points was increased to allow a deeper pool and to adjust for the smaller distance from the bottom of the RPV to the cavity floor. Therefore, the computation time is the limiting factor for AP1000, and the ex-vessel fuel coolant interaction simulation is performed for only 6 msec. For comparison purposes, only the 6 msec of interaction in AP600 is shown.

Figures 6.8 and 6.9 show the predicted maximum pressure in the cavity water pool as a function of time. Apart from a higher peak of nearly 1000 MPa for AP1000 in Figure 6.8, the maximum pool pressure is higher in the AP600 calculation between 1 and 3 ms. As mentioned previously, the higher pressure in AP600 calculation may be due to higher initial melt velocity and a higher distance from the cavity floor.

The higher pressures on the cavity wall in the AP600 calculation shown in Figure 6.11 (AP1000 pressure are shown in Figure 6.10) are consistent with the higher maximum pool pressure in Figure 6.9. The pressure time response behaviors show some differences; however, the calculated pulse durations are similar.

Figures 6.12 and 6.13 show the impulse loads on the cavity wall for AP600 and AP1000. Because of higher pressures in the AP600 calculation, the impulse load is also higher. The maximum impulse load for AP600 at 6 ms is about 500 kPa-s while the maximum impulse load for AP1000 is 300 kPa-s. Therefore, it appears that the impulse loads calculated for AP600 are bounding.

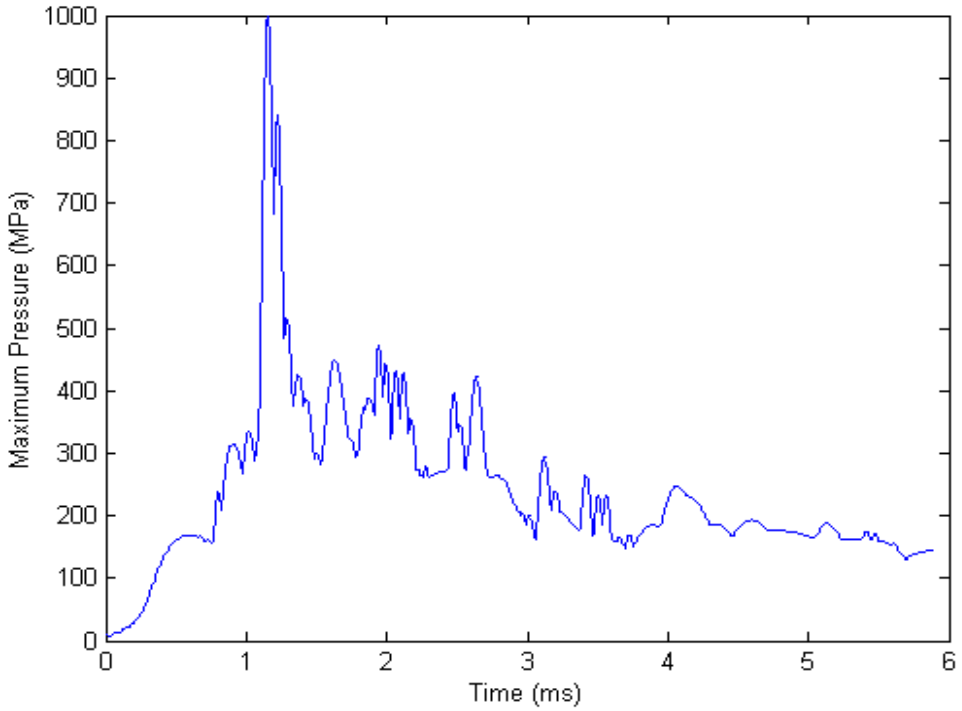

Figure 6.8 Predicted maximum pressure in the pool (Ceramic)

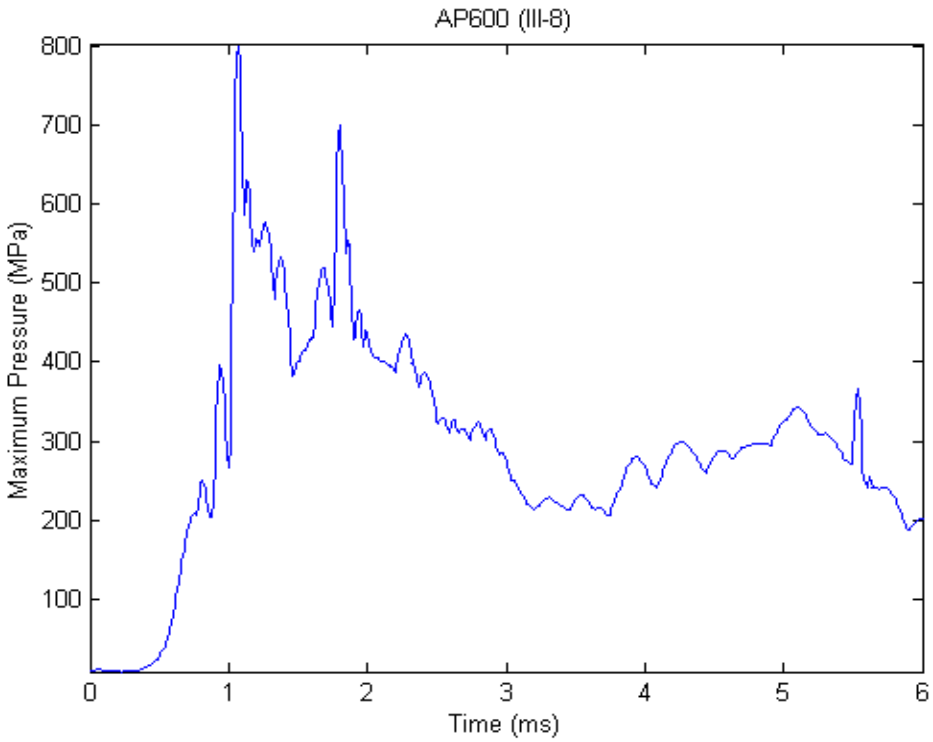

Figure 6.9 Predicted maximum pressure in the pool for AP600 (Ceramic)

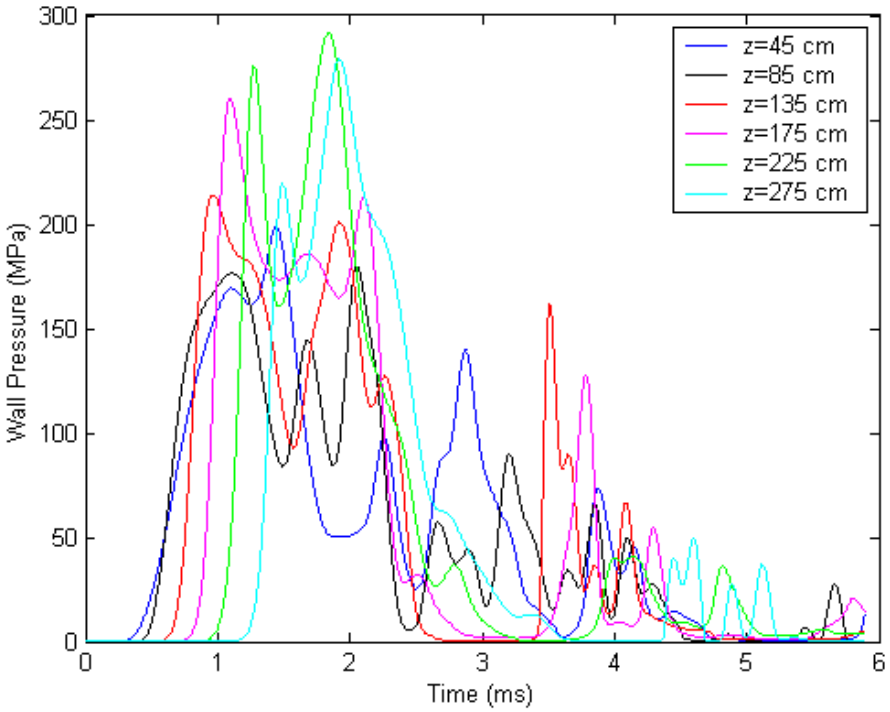

Figure 6.10 Cavity wall pressures at various axial locations (Ceramic)

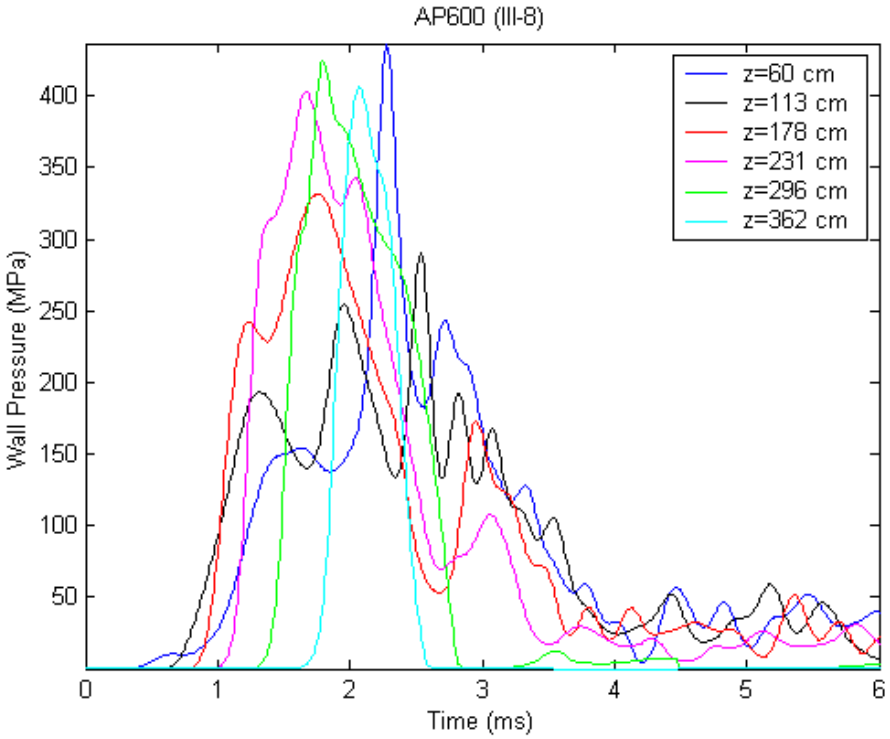

Figure 6.11 Cavity wall pressures at various axial locations for AP600 (Ceramic)

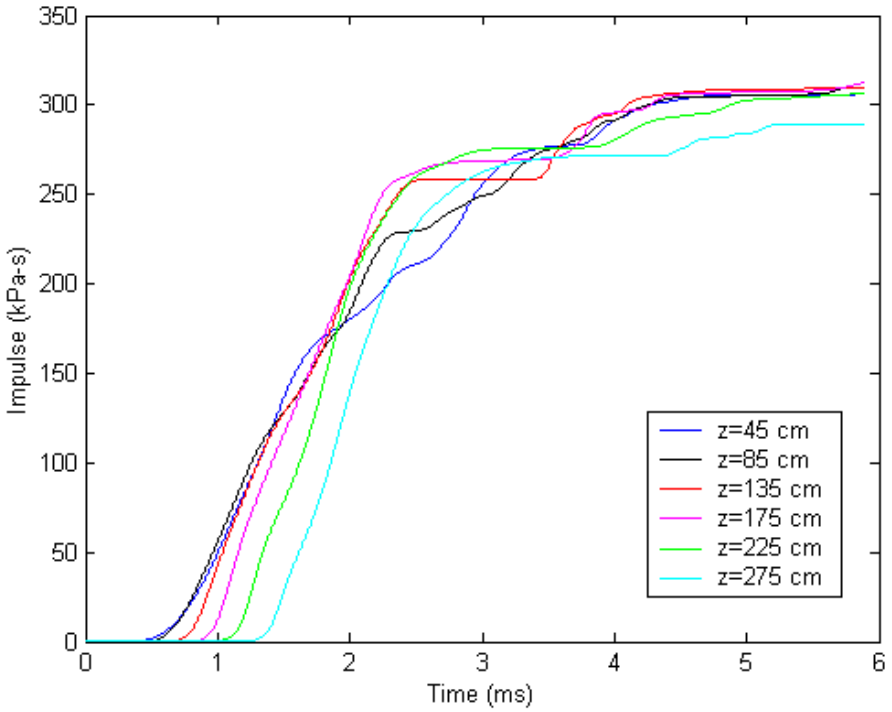

Figure 6.12 Cavity wall impulse loads at various axial locations (Ceramic)

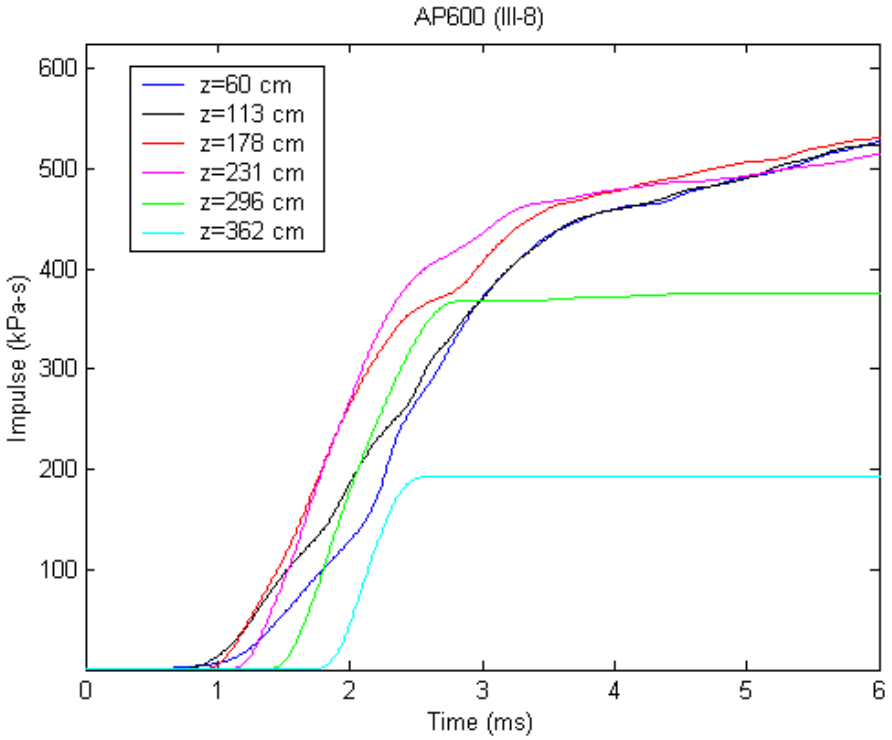

Figure 6.13 Cavity wall impulse loads at various axial locations for AP600 (Ceramic)

6.2.2 Larger Failure Hole Size

The impact of the failure hole size on the energetics of the explosion is considered using a sensitivity case involving a hole size of 0.6 m. Referring to Figure 6.1, the initial hole involved three grid points in the x-direction from 0.6 m to 1.2 m. For the AP600 calculation [1], the failure size was 0.8 m, but that calculation was terminated due to numerical instabilities. Therefore, in the present sensitivity calculation, it was decided to use a smaller initial hole size.

The maximum pressure in the pool for a hole size of 0.6 m is plotted as a function of time in Figure 6.14. The maximum wall pressure and the impulse load are higher than the base case as shown in Figures 6.15 and 6.16. The maximum calculated wall pressure is nearly 140 MPa, and the maximum impulse load on the wall is about 150 kPa-s. The calculated impulse loads are nearly a factor of two larger than the base case.

6.2.3 Larger Initial Particle Diameter and Maximum Fragmentation Rate

The fragmentation model parameters significantly impact the dynamics of the explosion. In the ESPROSE.m model, the initial particle diameter and the maximum rate of fragmentation per particle affect the resulting explosion pressure and the impulse loads on the cavity wall. A particle diameter of 0.01 m was assumed for the base case calculation, and the maximum rate of fragmentation per particle was 4 kg/s. The initial particle diameter of 0.01 m and the corresponding maximum fragmentation rate of 4 kg/s per particle are the same as those provided in Reference [1].

The particle diameter was increased from 0.01 m to 0.1 m, while increasing the maximum fragmentation rate per particle to 400 kg/s. The fragmentation model discussed in Appendix C of Reference [1] is used to predict the rate of fragmentation per particle; however, if the particle fragmentation rate exceeds the maximum fragmentation rate per particle during a time step, the ESPROSE.m code uses the latter value. Since the rate of particle fragmentation per particle is approximately proportional to the particle surface area, increasing the particle diameter and keeping the maximum rate of fragmentation per particle constant at 4 kg/s will inevitably lead to lower pressures as shown in the previous sensitivity calculation.

Therefore, in this sensitivity calculation, the maximum fragmentation rate per particle is increased in proportion to the increased surface area, i.e., the maximum fragmentation rate per particle is increased to 400 kg/s.

The calculated maximum pressure in the water pool is much smaller for this case as compared with the base case. The maximum pressure in the pool and on the cavity wall as well as the impulse load on the cavity wall near the explosion zone are plotted as a function of time in Figures 6.17 through 6.19. The calculated impulse load on the cavity wall closest to the RPV (i.e., the near wall) is ~12 kPa-s, and approximately a factor of seven smaller than the impulse for the base case.

6.2.4 Bottom Failure of the Lower Head

The impact of the lower head bottom failure is studied in this sensitivity calculation. This failure location is postulated for Configuration II, because a bottom failure of lower head for Configuration I is extremely unlikely. Therefore, the composition of the melt would be metallic (i.e., U-Fe-Zr). Using the results of Section 4.4 for the material properties of the melt, and assuming a well-mixed heavy bottom layer, the temperature of the melt is estimated at 2300K.

In the PM-ALPHA calculation for the mixing phase of the FCI, the extent of the domain in the x-direction is 5.2 m, and in the y-direction, it is 1 m (see Figure 6.1). Therefore, only a small section of the computational mesh is used in the mixing phase to allow for the inlet boundary condition at the center of the computational domain. The distribution of the vapor void fraction and the melt volume fraction are shown in Figures 6.20 and 6.21. The duration of the premixing was 0.25 second to allow the melt to reach the cavity floor.

The propagation of the pressure in the cavity around the RPV is shown at different times in Figure 6.22. Note that the trigger cell is located at the bottom of the water pool at about x=1 m as shown in Figure 6.20. The initial pressurization in Figure 6.22a at 1 msec is mainly due to the effect of the trigger cell. The maximum pressure in the cavity pool, and the pressures on the cavity wall are shown in Figures 6.23 and 6.24. The maximum impulse load on the cavity wall is about 9 kPa-s as shown in Figure 6.25. Therefore, the FCI energetic is rather benign for this case.

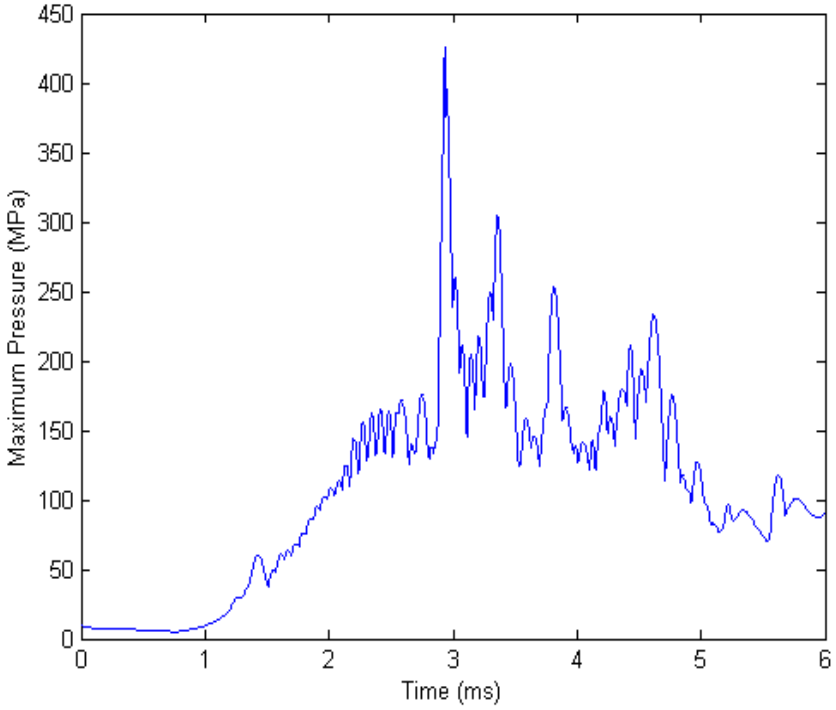

Figure 6.14 Predicted maximum pressure in the pool (0.6 m hole)

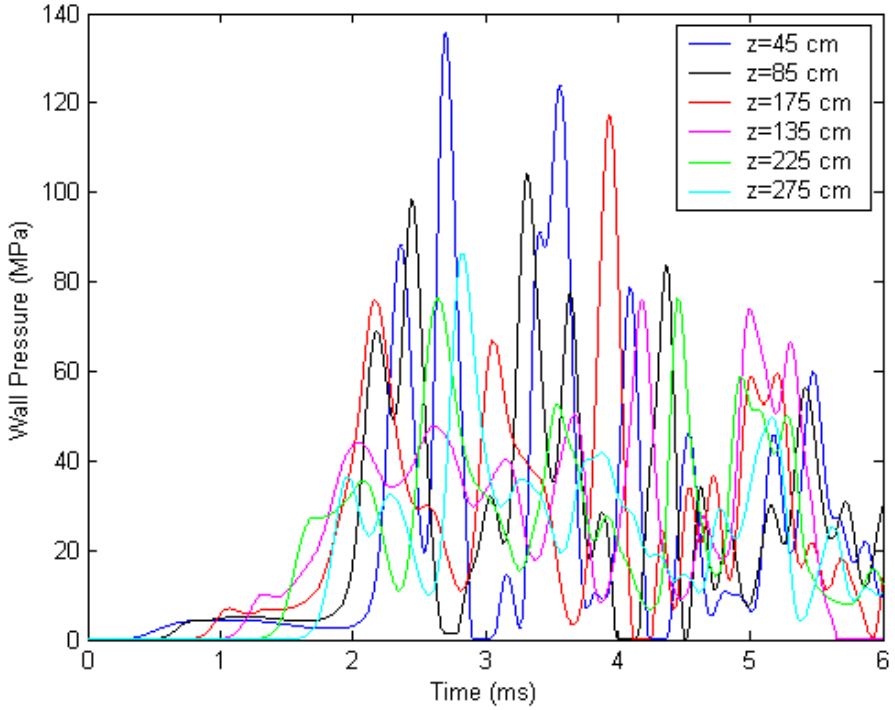

Figure 6.15 Predicted cavity wall pressures at various axial locations (0.6 m hole)

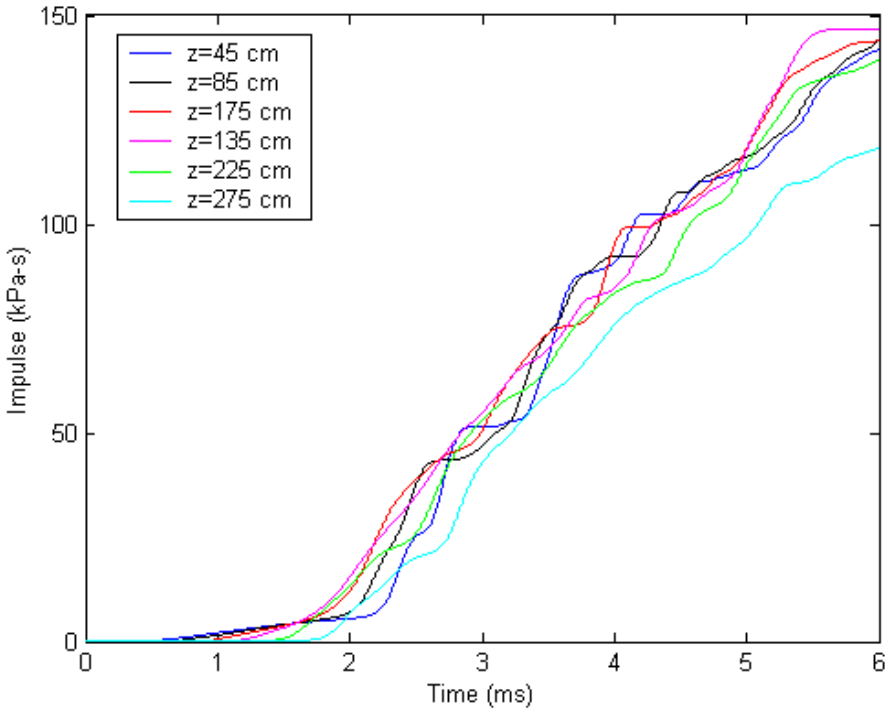

Figure 6.16 Predicted cavity wall impulse loads at various axial locations (0.6 m hole)

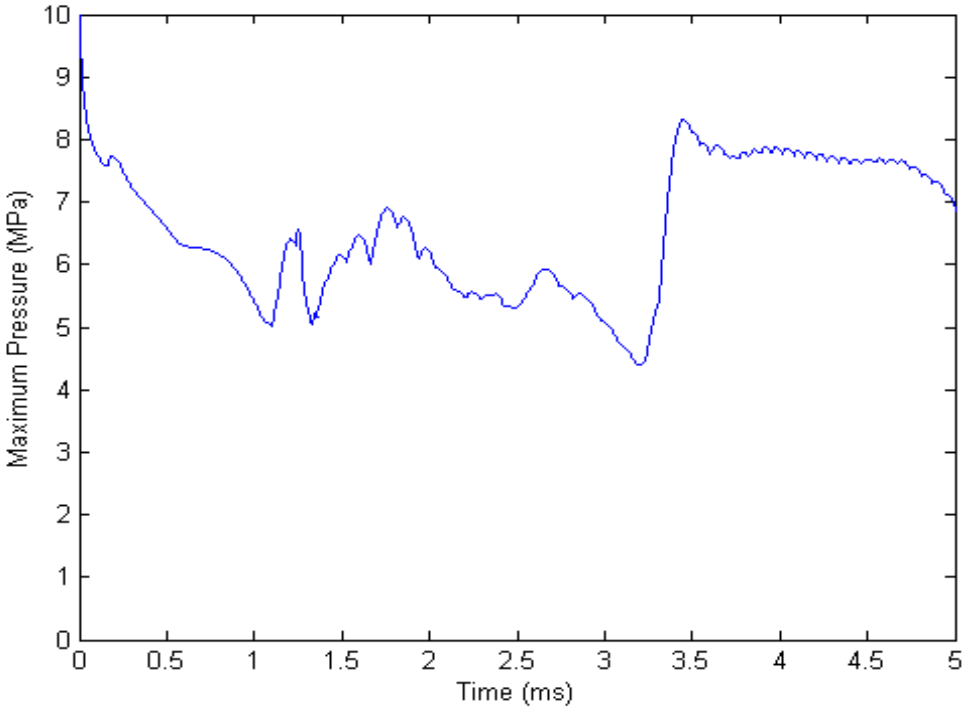

Figure 6.17 Predicted maximum pressure in the pool (model parameters)

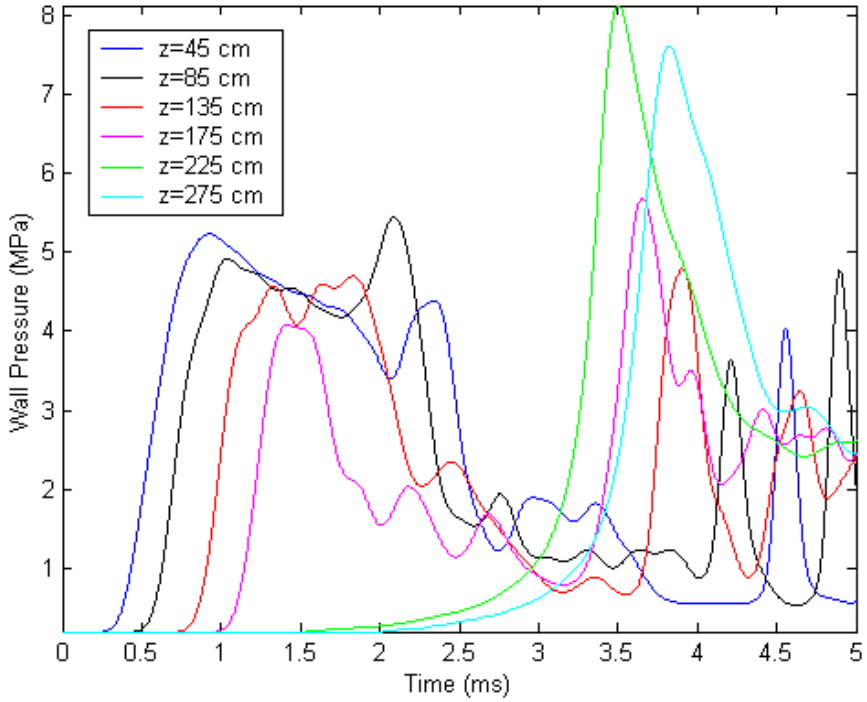

Figure 6.18 Cavity wall pressures at various axial locations (model parameters)

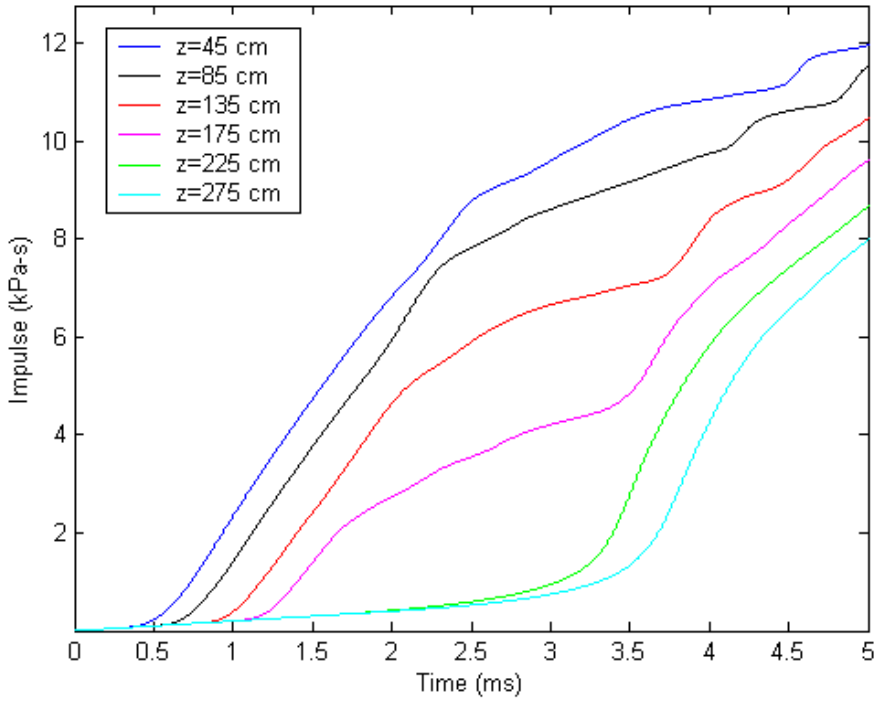

Figure 6.19 Cavity wall impulse loads at various axial locations (model parameters)

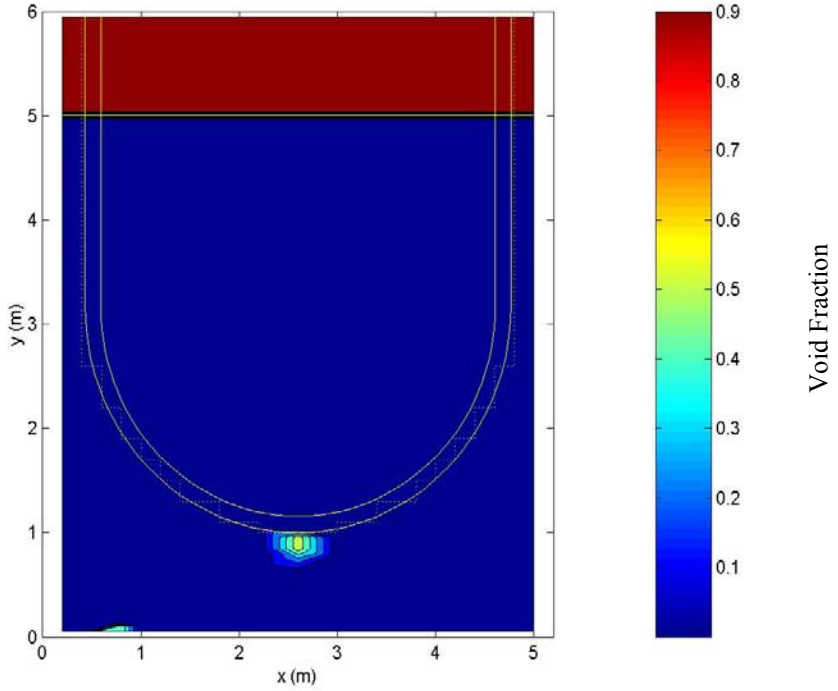

Figure 6.20 Predicted vapor void fraction at 0.25 second (bottom failure)

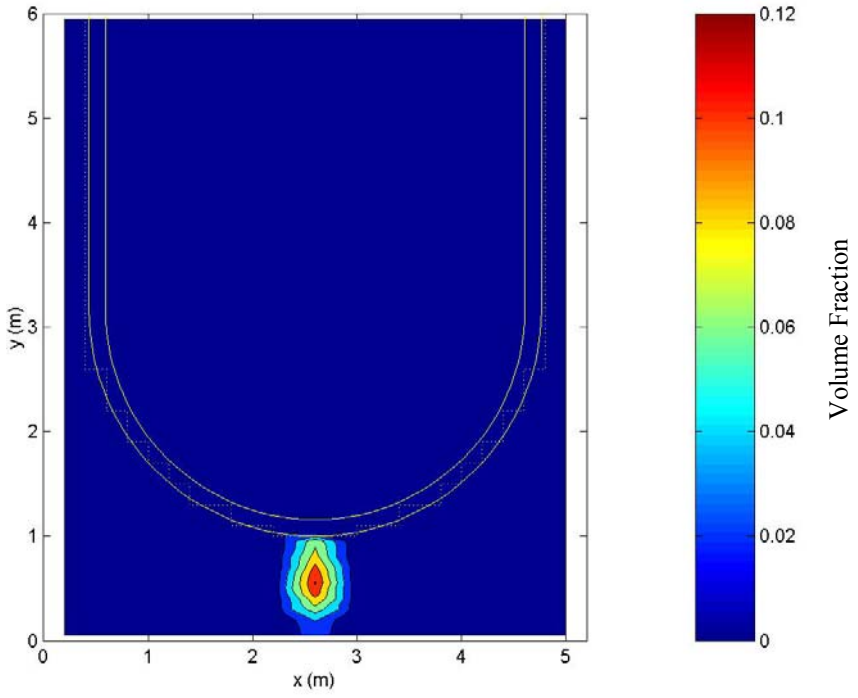

Figure 6.21 Predicted melt volume fraction at 0.25 second (bottom failure)

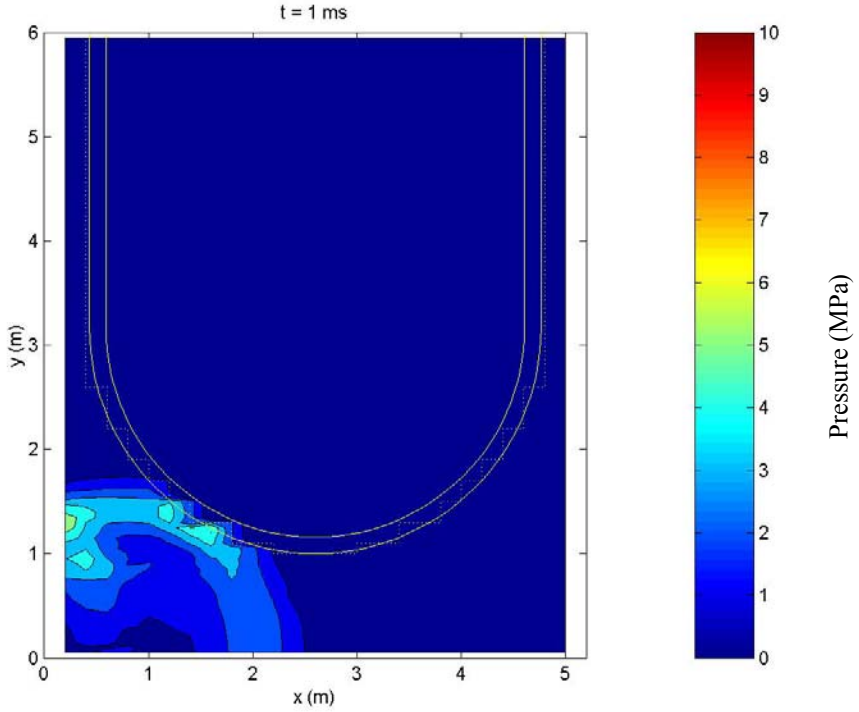

Figure 6.22a Predicted pressure distribution in the cavity at 1 ms (bottom failure)

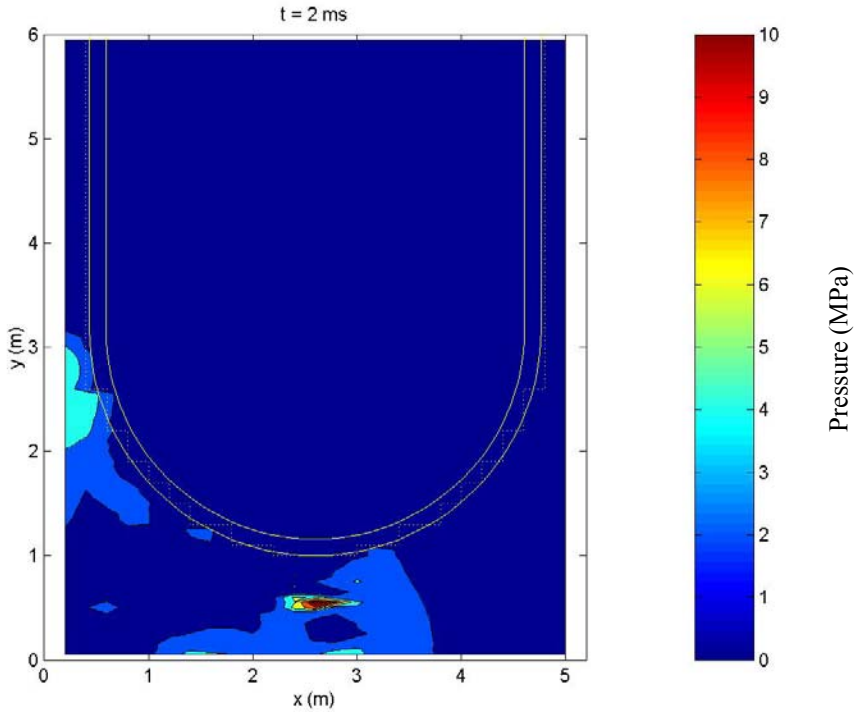

Figure 6.22b Predicted pressure distribution in the cavity at 2 ms (bottom failure)

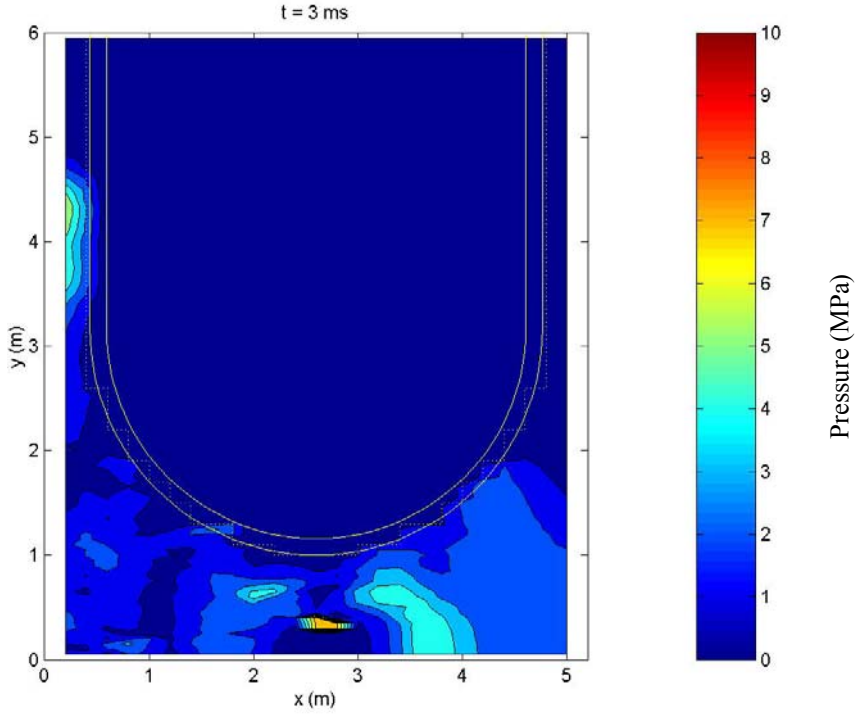

Figure 6.22c Predicted pressure distribution in the cavity at 3 ms (bottom failure)

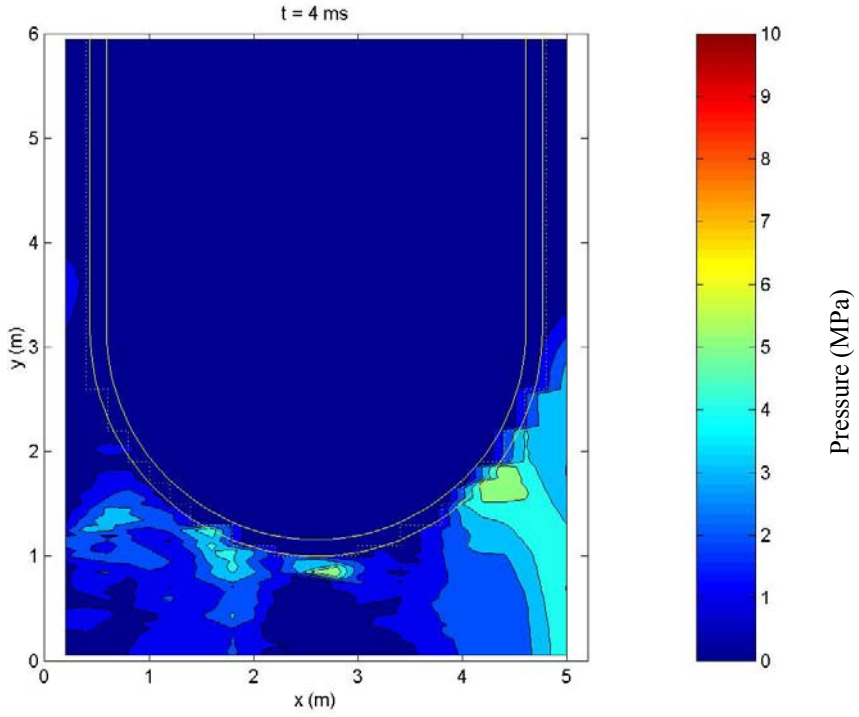

Figure 6.22d Predicted pressure distribution in the cavity at 4 ms (bottom failure)

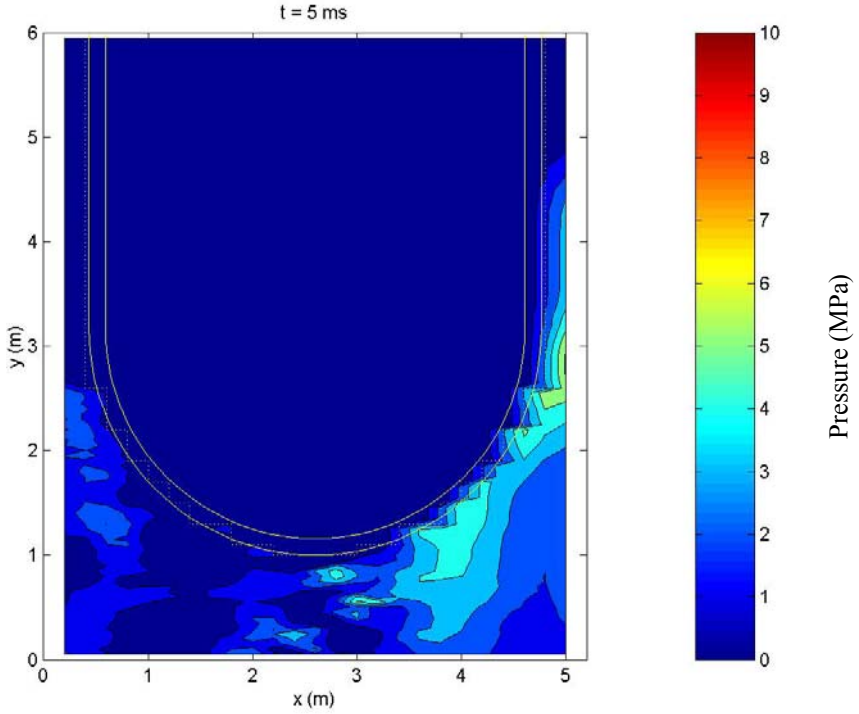

Figure 6.22e Predicted pressure distribution in the cavity at 5 ms (bottom failure)

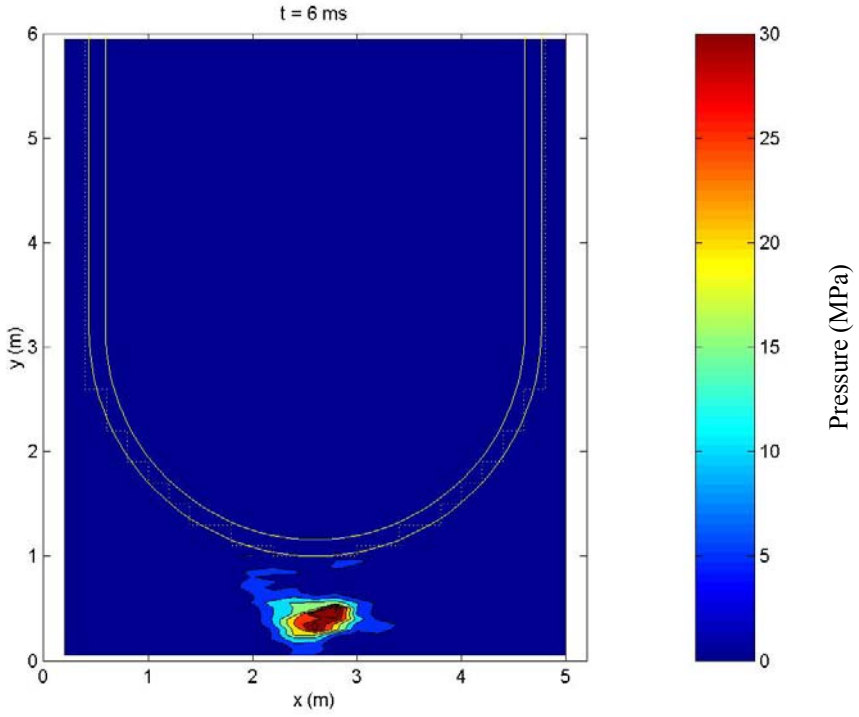

Figure 6.22f Predicted pressure distribution in the cavity at 6 ms (bottom failure)

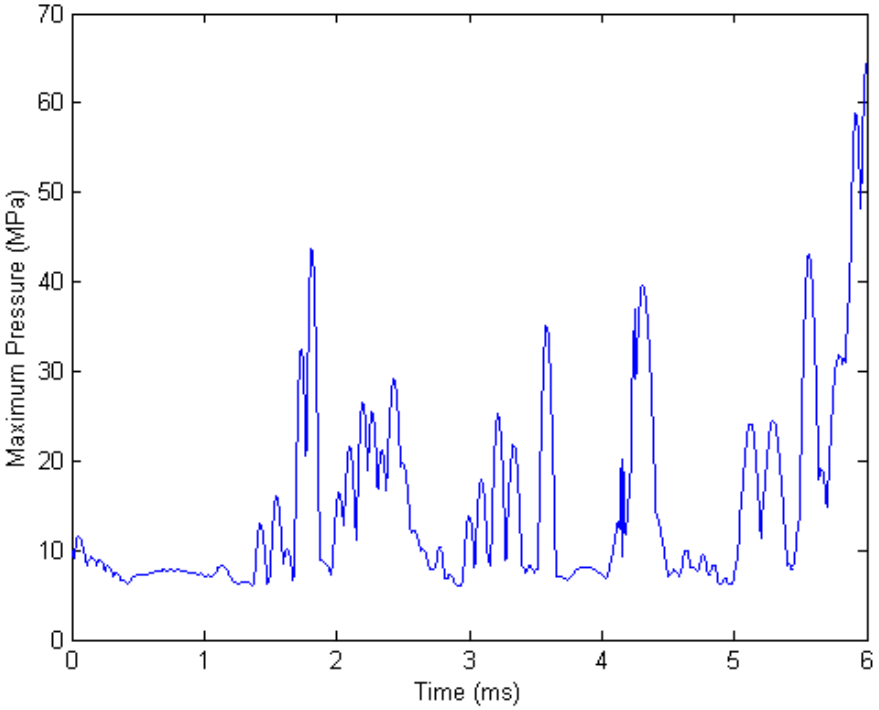

Figure 6.23 Predicted maximum pressure in the pool (bottom failure)

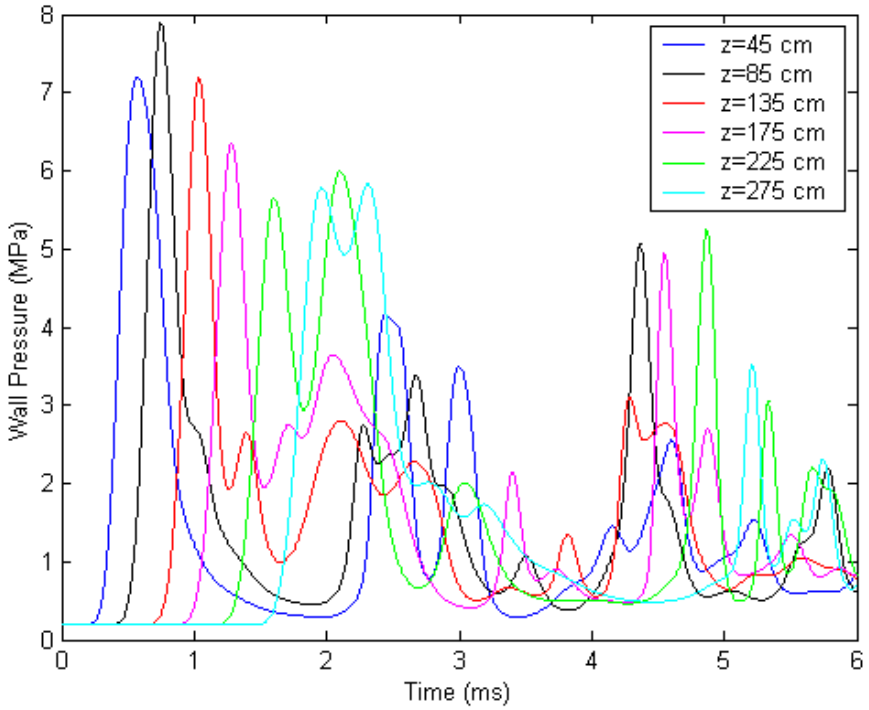

Figure 6.24 Cavity wall pressures at various axial locations (bottom failure)

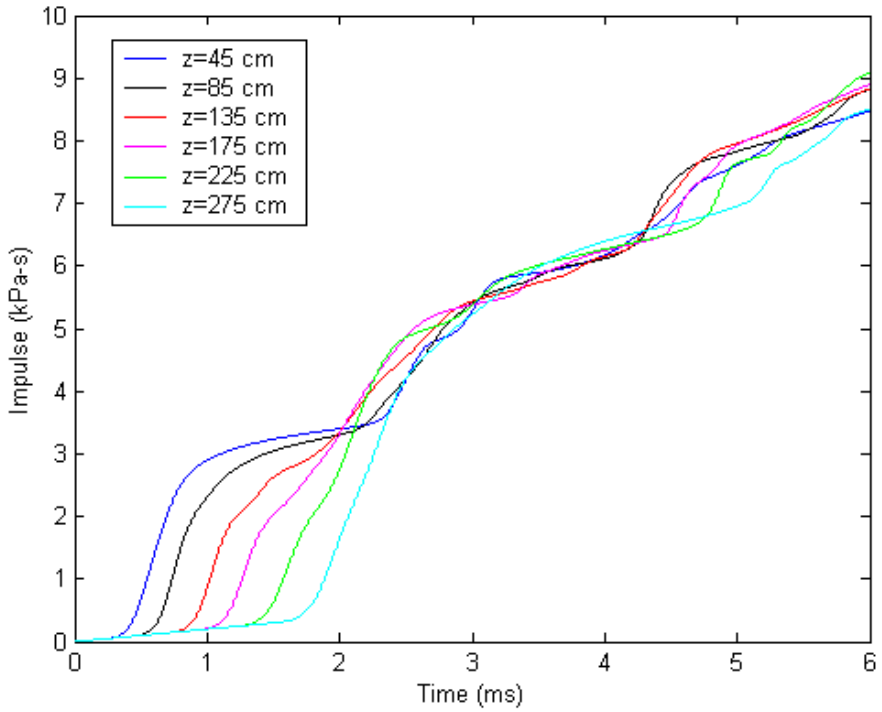

Figure 6.25 Cavity wall impulse loads at various axial locations (bottom failure)

7. SUMMARY AND CONCLUSIONS

7.1 Summary

An assessment of the likelihood and the most likely location of the RPV lower head failure following low-pressure severe accident scenarios in AP1000 has been made, as a basis to derive the various scenarios that could result in energetic interactions of the molten core material and cavity water, and the subsequent assessment of the ex-vessel FCI dynamic loads.

The thermal response of the lower head was examined by assuming two bounding melt configurations. The first melt configuration involved a metallic layer on top of the molten oxide pool (Configuration I), and the second melt configuration allowed for the presence of an additional heavy metal layer below the oxide pool (Configuration II). A one-dimensional heat transfer model was used to assess the thermal response of the lower head for AP1000. The major uncertainties included the mass of UO_2 relocating from the core into the lower head, the fraction of Zr oxidation, the decay heat in the molten pool, and the mass of steel in the upper light metallic layer, and were quantified based on the results of various studies for AP600, and recent analyses for AP1000. The uncertainties were propagated using 1000 random samples to produce the distribution for the heat flux ratio (ratio of the local heat flux to the critical heat flux), which was considered as the figure-of-merit relevant to the assessment of RPV integrity and in-vessel melt retention (i.e., once the local heat flux exceeds the critical heat flux, the temperature excursion in the vessel wall would be expected to result in the failure of the lower head). The uncertainty distributions were characterized for Configuration I only; however, the parametric calculations were performed for Configuration II.

The results of the base case calculation for melt Configuration I showed that the local heat flux remained below the critical heat flux limit in the molten ceramic region; however, in some cases, the local heat flux in the light overlying metallic layer was found to exceed the critical heat flux due to the focusing effect associated with the presence of thin light metal layers. For thin light metallic layers, part of the heat flux from the ceramic pool is focused on a small area on the vessel sidewall that can exceed the critical heat flux limit at that location. The thin light metallic layers are associated with smaller quantities of the molten ceramic debris in the lower plenum following their initial relocation from the core region into the lower head. If the volume of the molten ceramic pool in the lower plenum is not sufficient to submerge the core support plate, the expected quantity of steel that would form a stratified layer on top of the ceramic pool would be minimal. In the present study, the amount of steel in the top light metallic layer is correlated with the mass of UO_2 that is relocated into the lower head.

A number of parametric calculations were performed to examine the sensitivity of the calculated results to the assumed initial conditions that included the heat transfer correlations in the molten oxide pool, lower probability of low UO_2 mass (thus mitigating the focusing effect), the material properties, and partitioning of the decay heat to the top metal layer. For the base case (see Table 7.1), it was estimated that the conditional failure probability of the vessel wall as a result of critical heat flux limitation was about 0.15 (i.e., due to the uncertainties associated with the late phase melt progression, the failure of the RPV lower head cannot be ruled out). The results of the parametric calculations showed that the lower head failure probability can range from 0.04 to 0.3 depending on the likelihood that is assigned to the initial melt relocations that would involve smaller quantities of ceramic material into the lower plenum, and the heat transfer correlations that are used in calculations.

Cases 1 through 8 assume no heat generation in the top metal layer, while for Cases 1D to 7D, a normal distribution is assumed between the lower bound of 0.1 and the upper bound of 0.2 for the fraction of the decay heat in the top metal layer (the rest of the decay heat is in the oxide layer).

The results showed that a combination of the focusing effect and the additional power in the metal layer can increase the likelihood of failure by a factor of 2 for Case 1D, and 1.5 for Case 2D. However, for the Case 3D, there is no significant increase in the conditional failure probability. This result is not surprising, because for Cases 3 and 3D, the fraction of upward heat transfer in the molten oxide pool is greater than for Cases 1 and 1D. At some point, increasing the decay power in the metal layer does not necessarily increase the conditional failure probability because of the reduction in the decay heat in the molten oxide pool (and thus reducing the upward heat flux from the molten oxide pool to the top metal layer).

In response to the peer review comments, three additional sensitivity calculations were also performed. The first sensitivity case involved the assessment of the impact of the tails of the uncertainty distributions on the calculated likelihood of vessel failure (Cases 6 and

Table 7.1 Comparison of lower head conditional failure probabilities (CFP)

Case	Description	Ceramic Layer CFP	Metal Layer CFP
WITHOUT DECAY HEAT IN THE LIGHT METAL LAYER			
1	Base case	0	0.15
2	DOE heat transfer correlations	0	0.20
3	Heat transfer correlations used in the INEEL study	0	0.30
4	Material properties	0	0.16
5	Reduce probability of low UO_2 mass	0	0.04
6	"Tails" of uncertainty distributions	0	0.16
7	Assumed ±10% uncertainty in CHF correlation	0	0.08-0.25
8	25% increase in heat transfer coefficient (oxide to light metal layer)	0	0.17
WITH DECAY HEAT IN THE LIGHT METAL LAYER			
1D	All other conditions are identical to Case 1	0	0.27
2D	DOE heat transfer correlations	0	0.30
3D	Heat transfer correlations used in the INEEL study	0	0.31
4D	Reduce probability of low UO_2 mass	0	0.07
5D	"Tails" of uncertainty distributions	0	0.30
6D	Assumed ±10% uncertainty in CHF correlation	0	0.20-0.31
7D	25% increase in heat transfer coefficient (oxide to light metal layer)	0	0.29

5D). For the case without decay heat in the light metal layer, the failure probability increased from 0.15 (Case 1) to 0.16 (Case 6), and for the case with decay heat in the light metal layer, the failure probability increased from 0.27 (Case 1D) to 0.30 (Case 5D). The second sensitivity case involved the assessment of the impact of the critical heat flux (i.e., by an arbitrary ±10% variation in critical heat flux) on the calculated likelihood of vessel failure. The uncertainties in the critical heat flux have a significant influence on the calculated failure probability that can range from 0.08 to 0.25 for the case without decay heat (Case 7) in the light metal layer, and from 0.20 to 0.31 for the case with decay heat (Case 6D) in the light metal layer. The third sensitivity case involved the assessment of the impact of arbitrarily increasing the heat transfer coefficient between the ceramic pool and the stratified light metallic layer by 25%. The impact of this enhancement in heat transfer coefficient on the calculated likelihood of vessel failure was shown to be minimal. The failure probability was found to increase from 0.15 (Case 1) to about 0.17 (Case 8) for the case without decay heat in the metal layer, and from 0.27 (Case 1D) to 0.29 (Case 7D) for the case with decay heat in the metal layer, respectively. The variations in the failure probabilities for these three cases are within the range of other variations also listed in Table 7.1; therefore, the overall conclusions regarding the likelihood of in-vessel retention through external cooling of the lower head, remain unchanged.

Additional parametric calculations were performed for melt Configuration II by varying the mass of uranium in the bottom heavy metallic layer, but assuming conservatively that the mass fraction of uranium is 0.4. The mass of steel in the bottom heavy metallic layer was fixed and it involved only the lower plenum energy absorbers, but the mass of Zr in the metallic layers was adjusted to ensure that the bottom layer is heavier than the oxide layer and to maintain the maximum uranium mass fraction. The parametric calculations were performed for various fractions of uranium that is in oxide form. It was assumed conservatively that the heat flux from the bottom layer to the vessel wall included only the heat generation in the bottom layer. The results of the calculations showed that the heat flux ratio remained well below the critical value of 1 using the assumed critical heat flux variation for AP1000 Configuration V based on the results of the recent critical heat flux experiments. However, even if the vessel fails at the bottom of the lower head, the melt column in the water pool is shorter than the melt column for a side failure of the vessel (i.e., melt reaches the cavity floor sooner when the explosion is assumed to be triggered). Because of the distance of the explosion zone to the cavity wall, the pressures on the cavity wall are expected to be lower than the side failure.

Based on the in-vessel retention analysis, the base case for the ex-vessel FCI was assumed to involve a side failure of the vessel and a metallic composition. For the AP1000 analysis, the entire lower head of the vessel was modeled based on the insights from the earlier AP600 study [1]. Modeling of the RPV structure within the computational domain significantly impacted the

maximum impulse loads on the cavity wall for AP600 depending on the water depth in the cavity [1]. For a fully submerged RPV in the AP600 analysis [1], the maximum impulse load on the cavity wall was almost doubled. In addition, the impulse loads on the RPV were similar to those on the cavity wall due to proximity of the explosion zone to both the RPV and the cavity wall.

A number of sensitivity calculations were also performed for AP1000 based on the results of the AP600 study [1]. The sensitivity calculations and the predicted loads from the FCI simulations are summarized in Table 7.2.

The composition of the melt has a significant impact on the calculated impulse loads on the cavity wall. Note that the present study does not consider the effects of chemical energy augmentation due to the presence of large metallic constituents. Chemical energy augmentation could have a significant impact on the dynamics of the explosion. Increasing the RPV failure size, and thus the quantity of the melt pour into the cavity water pool, increases the local pressures and the impulse loads on the cavity wall. Uncertainties in the fragmentation model parameters have a considerable impact on the energetics of fuel coolant interactions. In ESPROSE.m, the particle diameter and the maximum rate of fragmentation per particle can substantially impact the predicted pressures and the impulse loads. Increasing the assumed initial particle diameter from 0.01 m to 0.1 m, and the maximum fragmentation rate to 400 kg/s per particle, the maximum predicted impulse load was 12 kPa-s compared with 85 kPa-s for the base case. For the bottom failure of the lower head, the amount of melt in the pool before the explosion is triggered is limited due to the proximity of the lower head to the cavity floor. The result of this calculations showed that the impulse load on the cavity wall is rather benign.

7.2 Concluding Remarks

The uncertainties associated with late phase melt progression can result in the stratification of small quantities of metals over a ceramic pool and the focusing of the decay heat generated within the ceramic pool into a thin metallic layer having a small contact area with the vessel sidewall, that can exceed the critical heat flux at that location. The estimated likelihood of lower head failure ranges from a few percent to about 30%, given a low-pressure core melt accident.

Notwithstanding the uncertainties in the underlying phenomena associated with the fuel coolant interaction, based on two-dimensional computer code calculations, the present study has demonstrated the potential for large impulse loads on the cavity and the RPV structures (and subsequently the containment penetrations) in the AP1000.

The results of the ex-vessel fuel coolant interaction analyses for AP1000 have shown that the impulse loads on the cavity wall remain below the calculated loads for AP600. In the AP600 analysis, the base case involved a mostly ceramic melt pour, while in the present AP1000 analysis the base case melt pour is metallic. However, the sensitivity calculations for the most severe case of a deeply flooded cavity in AP1000 clearly showed that the AP600 impulse load predictions are bounding.

Table 7.2 Summary of the maximum loads resulting from energetic FCIs

Case	Impulse Load (kPa-s)	Wall Pressure (MPa)	Pool Pressure (MPa)
Base case	85	90	220
Ceramic Melt	305	290	1000
Hole diameter of 0.6 m	145	135	425
Particle diameter of 0.1 m and maximum fragmentation rate of 400 kg/s per particle	12	8	10
Bottom failure of the lower head	9	8	60

8. REFERENCES

1. H. Esmaili, R. Vijaykumar, M. Khatib-Rahbar, H. Wagage, "An Assessment of Ex-Vessel Steam Explosions in the AP600 Advanced Pressurized Water Reactor," Energy Research, Inc., ERI/NRC 95-211, September 1996.

2. H. Esmaili, S. Ali, R. Vijaykumar and M. Khatib-Rahbar, "Evaluation of Debris Coolability by External Cooling of the Lower Head for AP600 Using MELCOR," Energy Research, Inc., ERI/NRC 96-201, January 1996.

3. W. W. Yuen and T. G. Theofanous, "PM-ALPHA: A Computer Code for Addressing the Premixing of Steam Explosions," DOE/ID-10502, May 1995.

4. W. W. Yuen and T. G. Theofanous, "ESPROSE.m: A Computer Code for Addressing the Escalation/Propagation of Steam Explosions," DOE/ID-10501, April 1995.

5. M. F. Young, "The TEXAS Code for Fuel-Coolant Interaction Analysis," Proceedings of ANS/ENS LMFBR Safety Topical Meeting," Lyon-Ecully, France, 1982.

6. C. C. Chu, "One-Dimensional Transient Fluid Model for Fuel-Coolant Interaction Analysis," PhD Thesis, University of Wisconsin, Madison, WI, 1986.

7. J. Tang, "Modelling of the Complete Process of One-Dimensional Vapor Explosions," PhD Thesis, University of Wisconsin, Madison, WI, 1993.

8. U. S. Nuclear Regulatory Commission, "AP600 Final Safety Evaluation Report Related to the Certification of the AP600 Design," NUREG-1512, 1998.

9. Westinghouse Electric Company, "AP1000 Probabilistic Risk Assessment," Revision 0, March 2002.

10. B. D. Turland and J. Morgan, "Thermal Attack of Core Debris on a PWR Reactor Vessel," Proceedings of the International Meeting on Light Water Reactor Severe Accident Evaluation, Cambridge, MA, August 28-September 1, 1983.

11. H. Park and V. K. Dhir, "Steady State Analysis of External Cooling of a PWR Vessel Lower Head," AIChE Symposium Series 87, 283, 1-12, 1991.

12. J. E. O'Brien and G. L. Hawkes, "Thermal Analysis of a Reactor Lower Head With Core Relocation and External Boiling Heat Transfer," AIChE Symposium Series 87, 283, 159-168, 1991.

13. R. Henry and H. Fauske, "External Cooling of a Reactor Vessel Under Severe Accident Conditions," Nuclear Engineering and Design 139, 31-43, 1993.

14. B. D. Turland, "In-Vessel Phenomena Relevant to the Achievement of Debris Coolability by Ex-Vessel Flooding for a PWR," Proceedings of the OECD/CSNI/NEA Workshop on Large Molten Pool Heat Transfer, Gernoble, France, March 9-11, 1994.

15. T. G. Theofanous, et al, "Critical Heat Flux Through Curved, Downwards Facing, Thick Wall," Proceedings of the OECD/CSNI/NEA Workshop on Large Molten Pool Heat Transfer, Gernoble, France, March 9-11, 1994.

16. T. G. Theofanous, et al, "Experience From the First Two Integrated Approaches to In-Vessel Retention Through External Cooling," Proceedings of the OECD/CSNI/NEA Workshop on Large Molten Pool Heat Transfer, Gernoble, France, March 9-11, 1994.

17. F. J. Asfia and V. K. Dhir, "An Experimental Study of Natural Convection in a Volumetrically Heated Spherical Pool Bounded on Top with a Rigid Wall," Nuclear Engineering and Design 163, 333-348, 1996.

18. T. G. Theofanous, et al, "In-Vessel Coolability and Retention of a Core Melt," DOE/ID-10460, Volume I, October 1996.

19. J. L. Rempe et al., "Potential for AP600 In-Vessel Retention through Ex-Vessel Flooding,"

Technical Evaluation Report, INEEL/EXT-97-00779, December 1997.

20. O. Kymfilfiinen, H. Tuomisto and T.G. Theofanous, "In-vessel Retention of Corium at the Loviisa Plant," Nuclear Engineering and Design 169, 109-130, 1997.

21. T. G. Theofanous and S. Angelini, "Natural Convection for In-vessel Retention at Prototypic Rayleigh Numbers," Nuclear Engineering and Design 200, 1–9, 2000.

22. B. R. Sehgal, et al., "Assessment of Reactor Vessel Integrity (ARVI)," Nuclear Engineering and Design 221, 23–53, 2003.

23. J. M. Seiler, et al, "Analysis of Corium Recovery Concepts by the EUROCORE Group," Nuclear Engineering and Design 221, 119-136, 2003.

24. F. Mayinger, et al, "Examination of Thermohydraulic Processes and Heat Transfer in a Core Melt," BMFT RS 48/1, Institute für Verfanhrenstechnic der TU, Hanover, Germany, 1976.

25. C. M. Allison, J. L. Rempe, and S. A. Chavez, "Design Report on SCDAP/RELAP5 Model Improvements – Debris Bed and Molten Pool Behavior," INEEL-94/0174, November 1994.

26. W. M. Rohsenow, "A Method of Correlating Heat Transfer Data for Surface Boiling of Liquids," Transactions of ASME, 74, 969, 1952.

27. H. Park and V. K. Dhir, "Effect of Outside Cooling on the Thermal Behavior of a Pressurized Water Reactor Vessel Lower Head," Nuclear Technology, 100, 331, 1992.

28. T. N. Dinh, T. P. Tu, T. Salmassi, T. G. Theofanous, "Limits of Coolability in the AP1000-Related ULPU-2400 Configuration V Facility," Proceedings of the 10th International Topical Meeting on Nuclear Reactor Thermal Hydraulics (NURETH-10), Seoul, Korea, October 5-9, 2003.

29. S. Globe and D. Dropkin, "Natural Convection Heat Transfer in Liquid Confined by Two Horizontal Plates and Heated from Below," Transactions of ASME, 81C, 24, February 1959.

30. S. W. Churchill and H. H. S. Chu, "Correlating Equations for Laminar and Turbulent Free Convection from a Vertical Plate," International Journal of Heat and Mass Transfer, 18, 1323, 1975.

31. F. A. Kulacki and A. A. Emara, "High Rayleigh Number Convection in Enclosed Fluid Layers with Internal Heat Sources," U. S. Nuclear Regulatory Commission, NUREG-75/065, 1975.

32. T.G. Theofanous, et al, "The First Results from the ACOPO Experiment," Proceedings of the International Topical Meeting on Probabilistic Safety Assessment (PSA '96), Park City, Utah, September 1996.

33. J. H. Scobel, "The Potential for AP1000 Reactor Vessel Failure Induced by a Stratified Debris Bed with a Bottom Metal Layer during IVR," Proceedings of the 2003 International Congress on Advances in Nuclear Power Plants, Córdoba, Spain, May 4-7, 2003.

34. Westinghouse Response to the Request for Additional Information (RAI) #720.088 by U. S. Nuclear Regulatory Commission, March 2003.

35. M. Zavisca, Z. Yuan and M. Khatib-Rahbar, "Analysis of Selected Accident Scenarios for AP1000," Energy Research, Inc., ERI/NRC 03-201, April 2003.

36. Z. Yuan, M. Zavisca and M. Khatib-Rahbar, "Impact of the Reactor Pressure Vessel Insulation on the Progression of Severe Accidents in AP1000," Energy Research, Inc., ERI/NRC 03-205, September 2003.

37. M. M. Pilch, et al., "Resolution of the Direct Containment Heating Issue for all Westinghouse Plants with Large Dry Containments or Subatmospheric Containments," NUREG/CR-6338, February 1996.

38. R. L. Iman and M. J. Shortencarier, "A FORTRAN 77 Program and User's Guide for the Generation of Latin Hypercube and Random Samples for Use with Computer Models," NUREG/CR-3624, 1984.

39. V. Asmolov and V. Strizhov, "Overview of the Progress in the OECD MASCA Project,"

Presentation at the CSARP Meeting, Marriott Crystal Gateway, May 3-4, 2004.

40. D. Powers and A. Behbahani, “Density Stratification of Core Debris,” Presentation at the OECD MASCA Seminar, Paris, France, June 2004.

41. K. Y. Bang and M. L. Corradini, "Stratified Vapor Explosion Experiments," Nuclear Science and Engineering, 110, No. 2, May 1991.

42. K. Y. Bang and M. L. Corradini, "Stratified Vapor Explosion Experiments," Chemical Engineering Communication, 86, 31-42, 1989.

APPENDIX A: MATERIAL PROPERTIES

The material properties are calculated in accordance with the approach in Reference [19] as described in this appendix.

A.1 Thermal Conductivity

Metallic Layer:

$$k = f_{m-Zr}k_{Zr} + f_{m-ss}k_{ss} - 0.72 f_{m-Zr} f_{m-ss} \left| k_{Zr} - k_{ss} \right| \quad \text{(A.1)}$$

Oxide Layer:

$$k = f_{N-UO_2}k_{UO_2} + f_{N-ZrO_2}k_{ZrO_2} - 0.4 f_{N-UO_2} f_{N-ZrO_2} \quad \text{(A.2)}$$

where

$f_{m\text{-}ss}$ Stainless steel mass fraction
$f_{m\text{-}Zr}$ Zirconium mass fraction
$f_{N\text{-}UO2}$ Mole fraction of UO_2
$f_{N\text{-}ZrO2}$ Mole fraction of ZrO_2
k_{ss} Thermal conductivity for stainless steel, W/m-K
k_{Zr} Thermal conductivity for zirconium, W/m-K
k_{UO2} Thermal conductivity of UO_2, W/m-K
k_{ZrO2} Thermal conductivity of ZrO_2, W/m-K

The thermal diffusivity is defined as:

$$\alpha = \frac{k}{C_p \rho} \quad \text{(A.3)}$$

A.2 Dynamic Viscosity

The dynamic viscosities for the oxide and the metal layer are functions of temperature:

Metallic Layer:

$$\mu = 1.1081 \times 10^{-4} \exp\left(\frac{5776}{T_{bulk}}\right) \quad \text{(A.4)}$$

Oxide Layer:

$$\mu = 1.5868 \times 10^{-4} \exp\left(\frac{10430}{T_p}\right) \quad \text{(A.5)}$$

where, T_{bulk} is the metallic pool bulk temperature, and T_p is the oxide pool maximum temperature (in degrees K).

A.3 Specific Heat Capacity

The specific heat capacities of the molten metal and oxide layers are based on mass fractions of the constituents.

Metallic Layer:

$$C_p = f_{m-Zr}C_{p-Zr} + f_{m-ss}C_{p-ss} + f_{m-U}C_{p-U} \quad \text{(A.6)}$$

Oxide Layer:

$$C_p = f_{m-UO_2}C_{p-UO_2} + f_{m-ZrO_2}C_{p-ZrO_2} \quad \text{(A.7)}$$

where:

C_{p-UO_2} UO_2 specific heat capacity, J/kg-K
C_{p-ZrO_2} ZrO_2 specific heat capacity, J/kg-K
C_{p-Zr} Zr specific heat capacity, J/kg-K
C_{p-U} U specific heat capacity, J/kg-K
C_{p-ss} Stainless steel specific heat capacity, J/kg-K
f_{m-Zr} Zr mass fraction
f_{m-ss} Stainless steel mass fraction
f_{m-U} U mass fraction
f_{m-UO_2} UO_2 mass fraction
f_{m-ZrO_2} ZrO_2 mass fraction

A.4 Thermal Expansion Coefficient

The thermal expansion coefficient is evaluated based on the volume fraction:

Metallic Layer:

$$\beta = f_{v-Zr}\beta_{Zr} + f_{v-SS}\beta_{SS} + f_{v-U}\beta_U \quad \text{(A.8)}$$

where:

β_{Zr} Zr volumetric coefficient of thermal expansion, K^{-1}
β_{SS} Stainless steel volumetric coefficient of thermal expansion, K^{-1}
β_U U volumetric coefficient of thermal expansion, K^{-1}
f_{v-Zr} Zr volume fraction
f_{v-ss} Stainless steel volume fraction

f_{v-U} U volume fraction

Oxide Layer:

In Reference [19] a mean pool volumetric coefficient of volumetric expansion equal to 1.05 x 10^{-4} K^{-1} is used.

A.5 Density

The density for the metallic and the oxide layers are given below.

Metallic Layer:

$$\rho = f_{v-Zr}\rho_{Zr} + f_{v-ss}\rho_{v-ss} + f_{v-U}\rho_{U} \quad \text{(A.9)}$$

Oxide Layer:

$$\rho = f_{v-UO_2}\rho_{UO_2} + f_{v-ZrO_2}\rho_{ZrO_2} \quad \text{(A.10)}$$

where:

ρ_{UO_2} UO_2 density, kg/m^3
ρ_{ZrO_2} ZrO_2 density, kg/m^3
ρ_{Zr} Zr density, kg/m^3
ρ_{U} U density, kg/m^3
ρ_{ss} Stainless steel density, kg/m^3
f_{v-Zr} Zr volume fraction
f_{v-ss} Stainless steel volume fraction
f_{v-U} U volume fraction
f_{v-UO_2} UO_2 volume fraction
f_{v-ZrO_2} ZrO_2 volume fraction

Individual constituent properties used in quantifying the metallic layer and oxidic pool properties are summarized in Table A.1.

Table A.1 Material properties

Constituent	Property	Symbol	Value*
Zr	Density (kg/m^3)	ρ_{Zr}	6130 (180)
U		ρ_{U}	17,500 (1750)
ZrO_2		ρ_{ZrO_2}	5990 (100)
UO_2		ρ_{UO_2}	8740 (200)
SS		ρ_{SS}	7020 (90)
Zr	Thermal conductivity (W/m-K)	k_{Zr}	36.0 (5)
U		k_{U}	49.0 (4.9)
ZrO_2		k_{ZrO2}	3.25 (1.85)
UO_2		k_{UO2}	5.6 (1.1)
SS		K_{SS}	24.1 (4.8)
SS	Specific heat capacity (J/kg K)	C_{p-ss}	835 (25)
Zr		C_{p-Zr}	458 (14)
U		C_{p-U}	157 (8)
ZrO_2		C_{p-ZrO_2}	815 (16)
UO_2		C_{p-UO_2}	485 (5)
SS	Thermal expansion coefficient (K^{-1})	β_{SS}	1.2x10^{-4} (0.17x10^{-4})
Zr		β_{Zr}	0.54x10^{-4} (0.11x10^{-4})
U		β_{U}	8.61x10^{-4} (0.60x10^{-4})

* The first number is the mean value, and the numbers in the parentheses are the standard deviations assuming a normal distribution as discussed in Reference [19]

APPENDIX B: RESPONSES TO PEER REVIEW COMMENTS

B.1 Review Comments by Dr. F. Moody and ERI Responses

SUMMARY COMMENTS

The study performed by Energy Research, Inc., has employed reasonable, carefully selected parameter ranges and computational models from state-of-the-art and historical documents for predicting the likelihood of vessel breach and Fuel-Coolant-Interaction (FCI), following a postulated severe accident in AP1000.

ERI RESPONSE:

No Comment.

If it is ever desirable to reduce conservatism in debris-vessel-cavity water heat transfer predictions, *multi-dimensional* heat transfer modeling should be considered. A more realistic, parabolic temperature profile (a flat profile was employed in this study) in the top metal layer would force more decay heat from its upper surface to reactor internals, reducing heat transfer to the adjacent vessel wall. The result could be a modest lowering of the predicted wall temperature, and a prolonging of vessel breach.

ERI RESPONSE:

The behavior of molten debris inside the lower head is a relatively complex problem, and even though additional insights would be gained by resorting to multi-dimensional heat transfer calculations; nevertheless, additional uncertainties can also emerge (e.g., code validation, applicability of turbulence models to natural convection conditions with internal heat generation, etc.).

Although experience has shown that most steam explosion demonstrations require an external trigger, it is necessary, at this stage of the technology, to assume that if molten core debris enters cavity water, some level of FCI is triggered. The study notes that predicted FCI forces are based on controversial inputs for premixing and fragmentation of the molten debris. Predicted impulse loads were obtained from relatively current computer models. These loads are presented with uncertainty disclaimers, but they are of sufficient magnitude and sensitivity to inputs to conclude that the potential exists for large impulse loads on the RPV and cavity walls.

ERI RESPONSE:

No Comment.

BACKGROUND

Energy Research, Inc. performed a study to assess the likelihood and potential location of the RPV lower head failure, following low-pressure severe accident scenarios in AP1000, and to assess the energetics of ex-vessel fuel – coolant interaction (FCI). The RPV failure study considers layered properties of molten debris in the lower plenum, cooling effects of external water that covers the submerged vessel bottom head, and localized melting of the vessel wall to allow melt discharge. The FCI study employs computer models to predict coolant interaction with molten debris, involving the stages of premixing, triggering, rapid steam formation, and the resulting pressure impulses exerted on the vessel and cavity walls.

Since statistical ranges exist for debris composition, mass, sequence and timing of relocation, and vessel external cooling mechanisms, the study provides a probabilistic framework for RPV lower head failure and the resulting potential FCI forces. Vessel failure is associated with the likelihood of exceeding the critical heat flux (CHF) on the vessel submerged outer surface. The sudden reduction in wall heat removal causes temperature rise and melting from the inner surface, finally breaching the vessel and permitting molten debris to be discharged into the cavity water.

Impulse loads from FCI were predicted from current models, even though technical controversy still exists over the dynamics of debris particle breakup and fragmentation, due to lack of convincing experimental validation. The study does not claim validated FCI impulse predictions. It does, however, demonstrate the potential for large impulse loads on the cavity and RPV in AP1000.

Both traditional and current correlations and computational methods have been employed by this study to assess severe accident results for AP1000, making use of earlier assessments for AP600.

ERI RESPONSE:

No Comment.

DISCUSSION

Likelihood and Potential Location of the RPV Lower Head Failure

The distribution of melt composition and internal heat generation in the lower plenum, and thermal resistance at the outer wall, primarily determine vessel breach timing and location. The study includes two melt distribution configurations:

Configuration I: A molten ceramic pool with an overlaying molten light metallic layer, and

Configuration II: A molten ceramic pool sandwiched between a bottom heavy metallic layer and a top light metallic layer.

The study notes that these configurations are likely to be bounding, based on their impact on the lower head integrity of AP1000, and an earlier INEEL study, which employed Configuration I.

One-dimensional heat transfer modeling for the molten layers, upper in-vessel heat sinks, the vessel wall, and external heat transfer regimes, were employed to predict where the critical heat flux would be reached on the outer submerged surface. The heat transfer correlations used are both classical and current, and should provide a defensible range of boundary conditions for all aspects of the study.

It is noted that Configuration I achieved a "focusing effect" in the metal layer, where the ceramic heat transfer upward, combined with internal heat generation, led to a state of critical heat flux, and consequent vessel wall melting in the top metallic layer near the molten oxide layer.

The decay heat fraction partitioned between the oxide and metal regions was varied in the analysis to include the effect on the conditional failure probability (CFP). There is always a temptation to wonder if there is some "optimum" partitioning or other combination of parameters, although physically reasonable, that would produce a "worst" possible vessel failure size and location. Rather than attempt a mathematical exercise of doubtful value, the study has used 1000 random samples of parameter combinations to arrive at failure probabilities. The probabilistic approach is more reasonable, because even if a single worst combination were identified, it is expected that its probability would be extremely small.

ERI RESPONSE:

We agree with the reviewer. In the probabilistic approach, it is more reasonable to assign the best estimate and bounding values for the probability distributions rather than perform a few point estimate calculations based on the bounds of the initial and boundary conditions.

The study notes that the size of the vessel wall failure could not be estimated with any degree of certainty. However, concluding that the metallic layer can be between 0.35 m and 0.53 m before reaching CHF, a failure hole diameter of 0.4 m was assumed for the base case. A probable upper bound of 0.6 m also was assumed.

ERI RESPONSE:

The reviewer is correct. There is much uncertainty regarding the size of the lower head failure, but the analysis in the report tries to bound the range of possible hole sizes.

The heat transfer models employed were one-dimensional from the bottom of the vessel to the top of the metal layer. Uniform temperatures were assumed in the layers, with sideways heat transfer through the vessel wall. Heat transfer to the vessel wall from the top metal layer will be slightly increased if that part of the vessel wall just above the metal layer is recognized to be a "fin", which conducts some additional fraction of the heat away from the hottest section of the vessel inner wall. A simple fin model shows that at the top of the metal layer, the ratio of vessel wall axial heat transfer to through-wall heat transfer is

$$\frac{q_{axial,wall}}{q_{througwall}} = \frac{\delta}{H}\frac{1}{h_\infty}\sqrt{\frac{hk}{\delta}}$$

where δ is the vessel wall thickness, H is the metal layer thickness, h_∞ is the wall external convection coefficient opposite the metal layer, h is the external convection coefficient above the metal layer (may be the same as h_∞), and k is the wall thermal conductivity. For boiling on the outer surface, a 15 cm wall thickness, 93 cm metal layer, and a wall thermal conductivity of 25 W/m-^{o}K , axial heat flow is only 1 or 2 percent of the wall heat flow. This ratio increases substantially for decreased values of convection coefficients or metal layer thickness. Although the fin effect probably has a minimal effect on wall melting, it works in a direction to lengthen the time until vessel breach.

ERI RESPONSE:

For the decreased value of the metal layer thickness, the challenge to the vessel wall integrity is the local heat flux in excess of the critical heat flux associated with the focusing effect. The heat transfer coefficients are relatively well established and known. In our earlier study with AP600 [2], it was shown that there is little difference between the 1D and 2D calculations as far as temperature gradients in the vessel wall are concerned.

The heat transfer study is based on uniform temperature in each layer. Actually, multi-dimensional effects will be present in each layer. If a molten layer has negligible internal circulation, two-dimensional heat transfer in the radial and axial directions works in a direction to reduce vessel wall temperature. This result can be supported by considering the temperature field in steps.

For the first step, heat transfer rates from the top and bottom surfaces of the metal layer are neglected. A constant volumetric heat generation rate throughout the layer would result in a steady parabolic temperature field with its peak at the vertical centerline. Temperature at the outer radius, *T(R)* , would be determined primarily by the convection coefficient for heat transfer to the surrounding water. Whether the molten layer temperature is parabolic or flat (as assumed in the study) the total heat production in the layer would be the same, and all generated heat would be transferred at the outer radius, resulting in the same wall temperature, *T(R)*, regardless of the internal temperature profile. The parabolic profile would appear as a parabola, built on the flat temperature profile.

The second step starts with the parabolic temperature profile and considers heat transfer from the top surface of the layer, which was neglected in the first step. Since the parabolic profile has higher temperature values than the flat profile, heat transfer from the top surface is higher. The approximate ratio of parabolic and flat heat transfer rates is given by:

$$\frac{q_{top,parabolic}}{q_{top,flat}} \approx 1 + \frac{h_{eq} R}{4k}$$

where h_{eq} is an equivalent convection coefficient to allow for radiation. For example, a parabolic temperature profile with an equivalent heat transfer coefficient of *50 W/m^2-^{o}K* would result in twice the top surface heat transfer rate than the flat temperature profile. Since more of the decay heat would exit from the top of the molten layer with a parabolic temperature profile, a smaller amount of heat would be transferred at the vessel wall. It follows that two-dimensional heat transfer effects result in a vessel wall temperature that is lower than the wall temperature associated with a flat temperature profile. Internal circulation caused by temperature gradients in the melt would tend to make the temperature profile less parabolic, but the trend toward lower wall temperatures would still be expected.

The assumption of uniform temperature in the layered regions, employed in this study, introduces conservatism in vessel wall temperature calculations. It also results in lower temperature of the melt that would be discharged into the pool if a vessel breach occurs. If it ever becomes desirable to reduce conservatisms in estimated vessel melting and breach probabilities, two-dimensional heat transfer models in the melt layers could play a dominant role.

ERI RESPONSE:

Note that the temperature profile in the metal layer is not very important because, the heat transfer in the metal layer is dominated by natural convection (since the bottom surface of the metal layer is hotter [with or without internal heat generation]). However, we agree with the reviewer that numerical/experimental analysis can capture the multidimensional effects associated with the heat transfer processes in the light metallic layer and provide additional insights.

<u>The Energetics of Ex-Vessel Fuel Coolant Interaction (FCI)</u>

The study notes that when molten core debris is discharged into the cavity water, predicted pressure loads from FCI involve significant uncertainties in modeling particle breakup and fragmentation, and the associated impulse. The pressure transient from FCI is largely determined by the rate of heat transfer from the molten debris, which also depends on the debris surface area. It is current practice in safety analyses to assume that some level of FCI must occur when molten debris enters water. Analytically, it can be shown that enough energy is available from both the kinetic energy of debris mass falling through water and impacting structures, and the rapid expansion of steam from water heated by contact with debris, to create substantial molten debris surface area as numerous droplets are formed. The accelerated surface area production and heat transfer to water can produce high pressure vapor, which undergoes explosive expansion. It is assumed in this study that a steam explosion will be triggered, even though it has been nearly impossible

to produce a laboratory explosion without artificial triggering, for example, by an exploding wire (according to Sandia experiments in the 1980's). It seems that FCI impulse predictions will be constrained by conservatism and controversy until controlled experiments reduce the ranges of uncertainty in premixing and fragmentation.

The study includes a range of parameters for the computerized prediction of FCI premixing, particle fragmentation, and explosion. Predicted pressure spikes and impulse loads are obtained from available computer models, which employ uncertain, but purposely selected conservative input parameters. The calculated impulse results could, in the extreme, lift the AP1000 pressure vessel about 55 ft. Earlier predictions showed that even though the AP600 had input parameters that would lead to higher FCI impulses (greater distance between the bottom head and the cavity floor) than in AP1000, the containment steel liner would remain intact.

Controversy still exists over mechanisms for steam explosions and impulse loads. The main conclusion is that the AP1000 study showed that there is a potential for large impulse loads on the cavity and RPV structures.

ERI RESPONSE:

The reviewer is correct. There are significant underlying uncertainties regarding FCI phenomena. The present study attempts to provide estimates of the FCI loads on the cavity wall for AP1000 using an approach that is consistent to an earlier study for AP600 [1]. As stated in the report, the results of the ex-vessel fuel coolant interaction analyses for AP1000 have shown that the impulse loads on the cavity wall remain below the calculated loads for AP600. The sensitivity calculations for the most severe case of a deeply flooded cavity in AP1000 clearly showed that the earlier impulse load predictions for AP600 [1] are bounding.

B.2 Review Comments by Dr. M. Corradini and ERI Responses

Enclosed are my review of the ERI report, ERI/NRC-03-202, entitled **Analysis of In-Vessel Retention and Ex-Vessel Fuel-Coolant Interactions for AP-1000.** In general, I found the report to be well written and quite comprehensive in providing a background to this technical issue. The report provides an excellent exposition for the analysis of the in-vessel retention and ex-vessel FCI explosion phenomena.

ERI RESPONSE:

No Comment.

In-Vessel Retention Modeling Approach:

The modeling approach developed seems quite reasonable and justified based on past work by the Westinghouse investigators and the NRC contractors. In fact, the exposition of the models used by all past investigators and the ERI staff is well written and facilitated comparison and further analyses.

ERI RESPONSE:

No Comment.

Critical Heat Flux from a Downward-Facing Surface:

The report notes that the current insulation design configuration (Configuration V) for AP1000 is not the same as past design configurations; i.e., it has been improved with respect to its ability to allow for a larger surface heat flux for cooling. Table 2.3 provides the Westinghouse CHF correlation parameters for Configuration III but not for IV or V. The report notes that the CHF limit for AP-1000 was taken to be 1.44 times the predicted values for Configuration III, based on the flow circulation CHF enhancements empirically measured in experiments by Westinghouse investigators. This physical effect seems qualitatively reasonable, but there are no data presented that justify this multiplicative factor.

ERI RESPONSE:

The CHF data for data the current insulation design configuration (Configuration V) for AP1000 has been requested by NRC; however, at this time, Westinghouse has not provided the data.

Benchmarking Analyses:

The ERI analyses were compared to Westinghouse (DOE) and INEEL (NRC) as a way to benchmark the methodology to be used for in-vessel retention analyses. Figures 2.2 to 2.7 provide a complete set of benchmark comparisons and the ERI analysis with DOE heat transfer correlations/models or with ERI-recommended correlations/models shows good agreement. This comparison clearly indicates that the ERI analysis methodology is acceptable.

ERI RESPONSE:

No Comment.

Initial and Boundary Conditions for In-Vessel Retention Analysis:

The in-vessel retention analysis requires that initial and boundary conditions be prescribed for key parameters, such as the decay heat, the amount of zirconium oxidation, the amount of molten urania discharged to the lower plenum etc. Figures 3.1 to 3.4 provide the frequency distributions to be used for the key parameters in the analysis. The justification for the range of values used is judged to be reasonable. There are certain ranges of values that may be questioned, but the probability of attaining these values is quite small (with the discretized Monte Carlo technique), thus the overall approach and values used seem acceptable. One possible way to verify that the "wings" of the distributions are not significant contributors to the overall conclusion, would be to eliminate them and redo the analysis; e.g., eliminating or reducing the probability of the large fraction of zirconium oxidation (>60%) and the large masses of molten urania released (>80%).

ERI RESPONSE:

This sensitivity case has been considered as suggested by the reviewer. The new input distributions are provided in Figures B.1 through B.3. The results are shown in Figures B.4 and B.5 for the base cases with and without the decay power in the metal layer. As expected the tails of the uncertainty distributions for the key initial conditions does not significantly affect the calculated conditional probability of lower head failure.

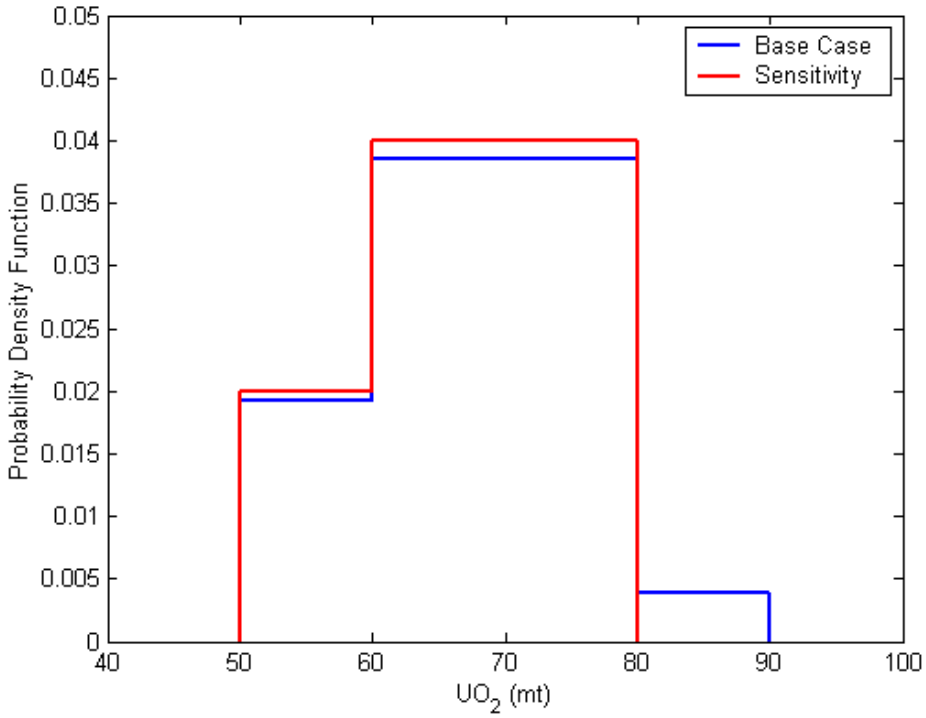

Figure B.1 Comparison of the distributions of UO_2 for AP1000

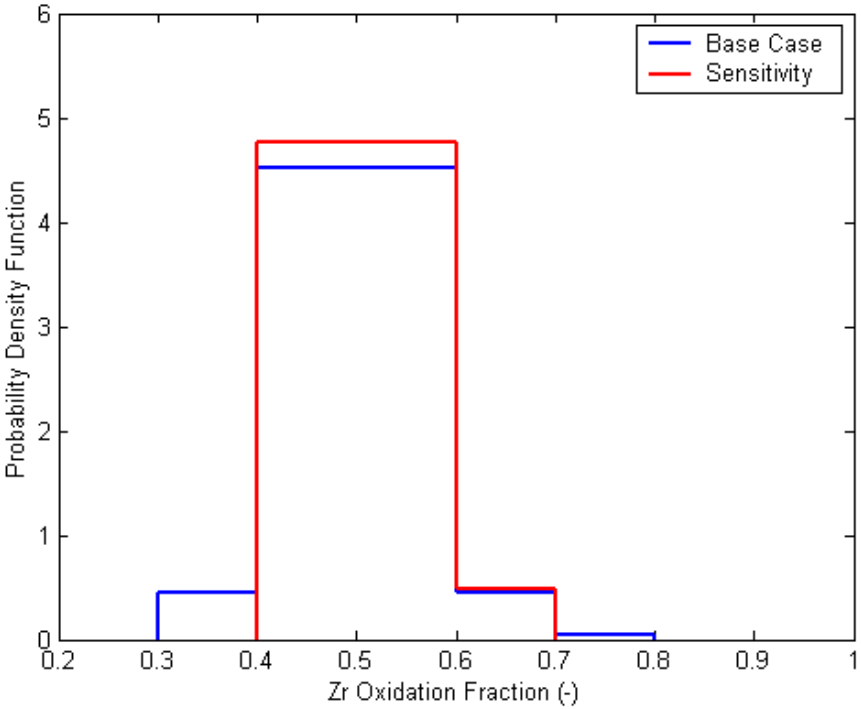

Figure B.2 Comparison of the distributions of Zr oxidation for AP1000

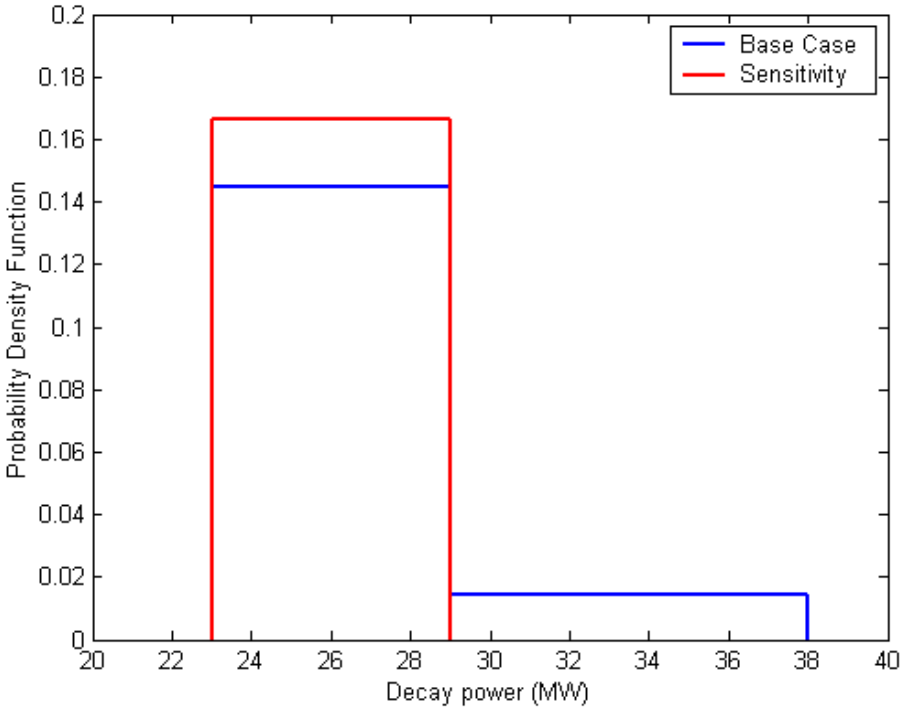

Figure B.3 Comparison of the distributions of decay power for AP1000

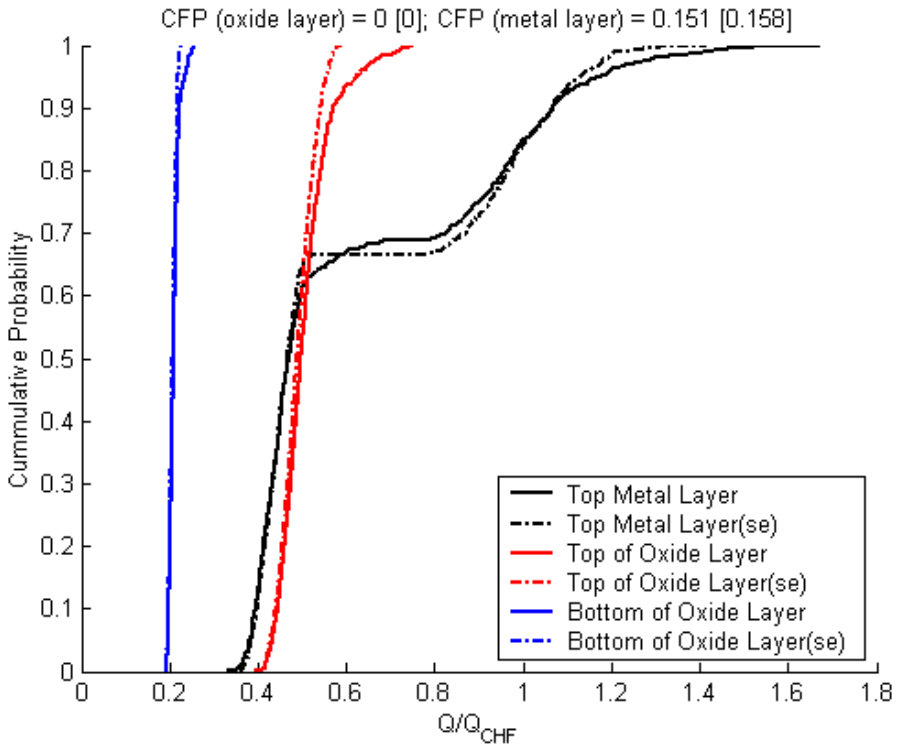

Figure B.4 Sensitivity to the initial conditions distributions for base case without decay power in the metal layer

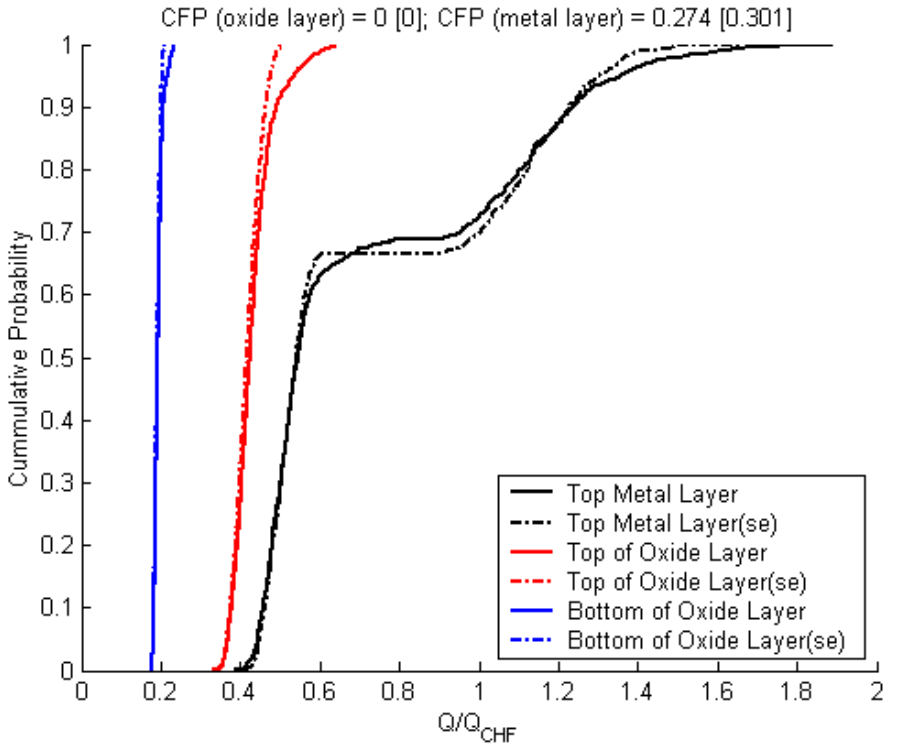

Figure B.5 Sensitivity to the initial conditions distributions for base case with decay power in the metal layer

Results of In-Vessel Retention Analysis:

The ERI analysis estimated the probability of failure of the RPV lower plenum wall due to molten corium heating around the periphery of the steel wall. The base case analysis was performed along with a number of sensitivity calculations to examine the impact of the initial and boundary conditions, as well as heat transfer correlations on the conditional failure probability of the vessel lower head. The results of the nominal base case as well as the list of the sensitivity calculations are given below. These results seem reasonable given the initial and boundary conditions used in the ERI analysis.

The largest impact on the conditional failure probability is due to the focusing effect associated with the low mass of molten oxidic and metallic debris in the lower plenum. The CFP is decreased by a factor of four from 0.15 to 0.04 for a five-fold reduction in the probability. For the case of the material properties in the sensitivity calculation, the point estimate mean values are used. The material properties distributions have minimal impact on the estimated CFP. The sensitivity case involving the heat transfer correlations show that the CFP is within 30% of that using the base case correlations. In addition, the results show that a combination of the focusing effect and the addition of additional power in the metal layer can increase the likelihood of failure by a factor of 2 for case 6, and 1.5 for case 7. However, for the case with the INEEL heat transfer correlations (case 8), there is no significant increase in the CFP. Also, increasing the decay power in the metal layer does not necessarily increase the CFP because of the reduction in the decay heat in the molten oxide pool.

ERI Analysis Table 4.2 Comparison of Lower Head Conditional Failure Probabilities (CFP)

Analysis Cases	Description	Ceramic Layer CFP	Metal Layer CFP
1	Base Case	0	0.15
2	DOE heat transfer correlations [18]	0	0.20
3	INEEL heat transfer correlations [19]	0	0.30
4	Material Properties	0	0.16
5	Reduce probability of low UO2 range from 0.0193 to 0.0046 in Figure 3.3	0	0.04
6	Base Case + Decay heat in the top metal layer	0	0.27
7	DOE heat transfer correlations [18] + Decay heat in the top metal layer	0	0.30
8	INEEL heat transfer correlations [19] + Decay heat in the top metal layer	0	0.31
9	Reduce probability level of low UO2 range from 0.0193 to 0.0046 in Figure 3.3 + Decay heat in the top metal layer	0	0.07

ERI RESPONSE:

No Comment.

Initial and Boundary Conditions for Ex-Vessel FCI Analyses:

The ERI investigators determined that the conditional probability of RPV lower plenum wall was non-negligible; i.e., 0.04 – 0.31. Because of this non-negligible magnitude, the ERI investigators developed an analysis methodology that estimated the consequences of dynamic pressures from an energetic fuel-coolant interaction due to a molten corium pour into the reactor cavity. The analysis method was to use the computer models PM-ALPHA and ESPROSE-m to model the processes of fuel-coolant mixing and the subsequent vapor explosion. The key initial and boundary conditions utilized in the analysis are reproduced below from a Table in the report.

ERI Table 5.1 Ex-Vessel FCI Base Case Conditions

Parameter	Value
Pour Composition	100% Metallic
Lower head failure hole diameter	0.4 m
Pour Temperature	2060K
Pour velocity	1.7 m/s
Containment pressure	2 bar-a
Cavity water temperature	343K

These initial and boundary conditions chosen seem reasonable, based on the explanation provided. In addition, four sensitivity calculations were performed as given in the table below. These sensitivities were chosen to bound the effects of uncertainties in the initial conditions as well as modeling uncertainties (for Case 5). Again, the sensitivities also seem reasonable

given the uncertainties of the FCI phenomena. However, there are two items that should be noted.

ERI Table 5.2 Summary of the base case and sensitivity calculations

Case	Variation from the base case	Comments
1	Base case scenario	Metallic pour at 2060K, lower head failure size of 0.4 m, melt particle diameter of 0.0 m, and the maximum fragmentation rate per particle of 4 kg/s.
2	Ceramic composition at 3150K	Pour involves ceramic material
3	Failure size of 0.6 m	Larger hole size
4	Bottom failure of the lower head	Metallic pour (U-Fe-Zr) at 2300K, lower head failure size of 0.4 m, melt particle diameter of 0.01 m, and the maximum fragmentation rate per particle of 4 kg/s.
5	Particle diameter of 0.10 m and maximum fragmentation rate per particle of 400 kg/s	Larger particle diameter and fragmentation rate

ERI RESPONSE:

No Comment.

First, the ERI report makes a point of the modeling of the RPV vessel boundary a semi-rigid structure that restricts the expansion from any energetic FCI once triggered below it in the reactor cavity region. This observation is quite correct and must be accounted for in some qualitative/quantitative manner. However, no mention is made about the insulation that surrounds the RPV lower plenum wall and how it affects the fuel-coolant mixing process and the subsequent explosion propagation/expansion. It seems that the presence of the insulation may have two important effects. Initially during the fuel-coolant mixing phase, the insulation could alter the flow of the molten material and hamper efficient fuel-coolant mixing. It would restrict the amount of water that could mix with the fuel and actually increase the void fraction of the vapor present in the region near the vessel wall. In addition, after the metallic melt has "cut" through the insulation by melting a hole in it, the residual passages in the insulation could trap vapor and provide a certain degree of compliance to the "rigid" boundary of the RPV outer wall. These to effects of altering the mixing process and provide a larger degree of "boundary compliance" to the RPV wall, may diminish the focusing effects of this surface and may reduce the dynamic pressures in the local region. This sort of effect is not specifically discussed in the analysis presented and this may be important in reducing the effect of dynamic pressurization.

ERI RESPONSE:

We agree with this observation, and statements have been added to the revised report to reflect this observation since it is important to note the significance of the insulation around the RPV, even though its impact cannot be quantified with available tools.

Second, the final sensitivity case (Case #5) investigates changing the initial particle diameter for mixing from 0.01 meter to 0.1 meter while increasing the fragmentation rate per particle from 4 to 400 kg/sec. These combined effects seem to reduce the energetics of the FCI, and the reasoning is unclear. This may be specific to the PM-ALPHA/ESPROSE-m models but it is not apparent based on the explanations provided. The other sensitivity cases and their behaviors seem very reasonable and explainable based on the ERI report.

ERI RESPONSE:

This sensitivity calculation for AP1000 was similar to that reported in Reference [1] for AP600. For a melt jet diameter of 0.4 m for the base case, the particle break up can lead to a particle size distribution when the melt reaches the bottom of the cavity. For the AP600, the TEXAS calculations provided estimates of the particle size where a dynamic mixing breakup was included in the code. In the PM-ALPHA code, the particle break up is parametric. Since the conditions for AP1000 were approximately similar to AP600 for the deeply flooded case, it was decided to perform the sensitivity to the initial particle size as had been performed previously for AP600.

The reason for increasing the maximum fragmentation rate is that the initial particle diameter is now also increased. The fragmentation rate is calculated internally by the ESPROSE code, but if the rate is higher than the user-specified value, the latter value is imposed. Since the rate of fragmentation should be

proportional to the particle surface area, the maximum fragmentation rate is increased accordingly. Note that it is possible that local fragmentation rate would be lower than the maximum user-specified value. This is somewhat similar to the empirical user-specified fragmentation time that is used in the TEXAS code.

B.3 Review Comments by Dr. V. K. Dhir and ERI Responses

The report is very well written, and the authors deserve to be congratulated. Uncertainty in specification of various parameters is correctly propagated to determine the conditional probability of vessel failure. I have organized my comments in the areas identified in the scope of the work.

1. Phenomenological portrayal of molten debris behavior and potential interactions with the lower head structures and cavity water.

   In general the authors have done a good job in providing phenomenological description of the potential interaction of molten core debris with vessel lower head. My specific comments are:

   a. The time of relocation of molten core debris, the amount, the temperature, the composition, decay heat, and manner in which relocation occurs depends on the accident conditions that are imposed. No supporting information is given for the values used in the base case or to show that the variations considered over the base case are indeed bounding.
   b. No information is given as to how one gets to the steady state (quasi) configuration after the core material starts to relocate. Is relocation of molten material in the form of a jet after failure of the crucible formed in the core totally ruled out? Significant damage to the vessel lower head is possible during the initial relocation of the material. This in turn may affect subsequent integrity of the vessel.
   c. In the assumed configurations of the relocated molten debris, crust of uniform thickness is assumed to exist along the vessel wall. It has been shown theoretically by Park [27] and subsequently experimentally by Asfia[6] that crust thickness varies along the vessel wall. Is assumption of constant thickness of the crust along the vessel wall conservative? If yes, on what basis?
   d. The mass of steel in the molten ceramic pool is assumed to have some proportionality with the mass of UO_2, I do not know the basis for this. As stated in item 'a,' the amount of steel that relocates to the vessel lower head will be dependent on the accident scenario and time into the accident.
   e. It is not clear as to how the composition of horizontal crusts separating different layers is determined. Why is the formation of crust at the top of the pool not considered?

ERI RESPONSE:

(a) As stated in Section 3 of the report, the quantification of the initial and boundary conditions is based on the results of plant-specific MELCOR calculations by ERI, and MAAP calculations by Westinghouse. In addition, the insights from the plant-specific SCDAP/RELAP5 calculations by INEEL for AP600 are also used, where appropriate. The important accident classes used in the report are based on the AP1000 PRA as explained in Section 3 of the report.

(b) Both the ERI and the Westinghouse analysis for the molten jet impact on the vessel wall indicated that vessel failure due to initial jet relocation is not likely.

(c) We have not imposed any assumption regarding the crust thickness. The non-uniform crust thickness along the inner surface of the vessel wall is part of the problem solution. This is clearly evident in Figure 2.3 as part of the benchmarking calculations.

(d) We have provided our rationale for steel melt distribution in Section 3.1.4 of the report. In general, there is proportionality between the ceramic mass and the steel mass inside the lower head. If the ceramic mass is sufficient enough to submerge the thick core support plate, then the steel mass will be expected to be significant (due to the melting of the submerged core support plate). On the other hand, if the ceramic mass that enters the lower plenum is small enough that would not result is the submergence of the lower core support plate, accordingly, the steel mass is expected to be substantially smaller (i.e., only the lower steel internals would be expected to melt and subsume in the molten pool.

[6] F. J. Asfia and V. K. Dhir, "Investigation of Natural Convection in a Volumetrically Heated Spherical Cavity Wall," Presented at the ASME Winter Meeting, 1995.

(e) We have considered the existence of lower and upper crusts in the molten pool, but no crust is assumed for the stratified metallic layer because, the metallic layer temperatures are generally higher than the metal melting temperature.

2. Heat transfer models and associated closure relations:

   a. Figure 2.1 shows a crust at the bottom of the light metal layer whereas on the top of page 8 of the report (limitation 2), it is stated that there is no crust.
   b. C_{sf} in eq. (2-11) is taken to be 0.013. This value is for saturated water. What is the basis for use of this value when the bulk liquid in the cavity is sub-cooled? Large variations in the value of C_{sf} can occur from surface to surface. No sensitivity study with respect to this variable has been performed. For example, a factor of 2 reductions in C_{sf} can lead to a factor of 8 reductions in the nucleate boiling heat transfer coefficient.
   c. What are the five unknowns that are being solved by for using equations (2·13) (2·17). One can only guess. It is important to specify as to which variables are assumed to be known.
   d. Since crust thickness and vessel wall thickness are not small, surface areas in the direction of heat flow can substantially change. Although a one dimensional model is employed, surface area correction could easily be included.
   e. An insulated top is considered for the heavy metallic layer. Could there not be heat transfer from the middle ceramic layer to the bottom layer?
   f. What is the rationale for increasing the CHF by a factor of 1·44 for AP- 1000. Enhancement or degradation factors will strongly depend on the liquid sub-cooling and flow conditions that develop in the insulation and cavity.
   g. Churchill and Chu correlation gives average heat transfer coefficient on a vertical wall. Local heat transfer coefficient just below the free surface of light metal layer could be substantially higher. Why is the consequence of this or vessel failure probability not included?
   h. In the ERI correlation for the ceramic pool—why is the effect of ratio of pool height to pool radius not included? Also, a clarification should be given with respect to the definition of heat transfer coefficient when volumetric heating exists in the layer. Some of the correlations reported in the literature are based on the maximum temperature in the pool and not the bulk.
   i. In Table 2·3, no basis is given for enhancement of CHF by 20-30% for AP-1000.
   j. It would be valuable if in table 2·4, the angular positions of the top of various layers were given. In the absence of this information, it is difficult to rationalize the results related to the upper portion of the pool.

ERI RESPONSE:

a. The crust shown in Figure 2.1 is the upper ceramic crust which is just below the light metallic layer. The limitation refers to a metal crust in the metallic layer.

b. The reviewer is correct. However, there is no significant impact regarding the nucleate boiling because the outer surface temperature is very close to the cavity water temperature. In fact, the analysis can be performed with a constant temperature assumption.

c. The 5 unknowns are the two heat fluxes at the inner and outer boundaries, and two temperatures at the inner and outer surfaces and the inner curst thickness. This is made clear in the revised report.

d. The surface area differences could be of the order of 15% based on the inner and outer radii of the lower head. In the ceramic layer, the heat flux remains below the critical heat flux; therefore, the inclusion of the variable surface area would not change the conclusion of the report. In the metal layer, the challenge to the vessel integrity is from the focusing effect associated with small metal masses. It is possible that the surface effects could slightly lower the failure probability for the base case. But other uncertainties (e.g., in heat transfer correlations) overshadow the differences in the surface area.

e. As explained in section 2.1.2.3 of the report, because of the internal heat generation in the bottom layer (due to decay heat), the top surface of the layer is expected to be hot because it is in contact with the molten ceramic pool, and the bottom layer is cool because of external cooling that leads to a thermally stable layer. Therefore, the conduction solution (assuming a flat plate with

internal heat generation) would result in a maximum temperature that occurs inside the bottom metallic layer, and the interface temperature between the bottom metallic and the ceramic layers is lower than the maximum temperature in the bottom metallic layer. Therefore, in the bounding configuration, it is assumed that all the heat that is generated in the bottom metallic layer is transferred to the vessel wall.

f. The rationale is the experimental evidence as explained in the footnotes to Table 2.3. However, we have performed a sensitivity calculation for a $\pm 10\%$ *variation in the critical heat flux and the results are shown in Figures B.8 and B.9 as will be explained later. Note that the uncertainties in the measured critical heat flux have not been reported by Westinghouse.*

g. The reviewer is correct. A multidimensional calculation would be needed which was beyond the scope of the present work. In addition, no experimental data is available to validate the model. A sensitivity calculation is performed by arbitrarily increasing the Churchill and Chu correlation by a factor of 1.25 (25% increase), and the results are shown in Figures B.6 and B.7. The impact on the CFP is minimal. It increases from about 0.15 to about 0.17 for the base case without decay heat in the metal layer, and from about 0.27 to 0.29 for the base case with decay heat in the metal layer.

h. We used the same correlation as for the AP600 analysis (ERI/NRC 95-211). In the AP600 analysis [1], it was shown that inclusion of the pool height reduces the Nusselt number by 10%. There are clearly larger differences between our default correlation and the ACOPO correlations. For the molten ceramic pool, the Grashof number is based on the maximum temperature as defined by Mayinger; however, the Nusselt number correlations in the literature are based on the Rayleigh number (with internal heat generation). In the present analysis, the energy balance in the molten ceramic pool yields the molten ceramic pool superheat. Since the ceramic pool is bounded by upper and lower crusts, only the molten pool superheat is used to calculate the heat transfer to the pool boundaries. In addition, without any loss of generality, the heat transfer correlations (based on internal Rayleigh number) along with the heat generation in the pool can be used directly to calculate the heat transfer partitioning to the lower and upper surfaces of the molten ceramic pool. For the upper steel layer, the heat transfer correlations are based on the bulk temperature. An energy balance in the metal layer yields the bulk temperature that is used to calculate the heat transfer to the top/bottom surfaces of the metal layer and to the vessel lower head. We will revise the definition for the heat transfer correlation as suggested by the reviewer.

i. The basis for the enhancement factor is experimental data for configuration V that has been reported by Westinghouse (the actual data and/or any resulting correlation has not been provided by Westinghouse to the NRC).

j. The angle for the ceramic pool is approximately 76°, which is evident in the results of the benchmark calculations (it is now stated specifically in Table 2.4). The metal layer extends to the cylindrical part of the vessel.

3. Initial and boundary conditions applicable to analysis of in-vessel retention:

   a. In AP1000, height and number of fuel assemblies is increased. There also exists internal structural changes in comparison to AP-600. Should not these changes affect the composition and temperature of the relocated core material?
   b. Was any attempt made to run SCDAP/RELAP to obtain the initial conditions for melt relocation in AP-1000?
   c. How long does it take to reach steady state configurations that are analyzed?
   d. Does the assumed decay power of 23-29 MW exclude that due to volatile fission products?
   e. I find it difficult to accept that system pressure has little effect on the progression and relocation phenomena.
   f. With a larger mass of the ceramic pool, it has been argued that focusing effect will be less. However, interaction with water of a larger mass could substantially increase the magnitude and duration of pressure pulse on the cavity wall.
   g. In equation (3·1), superscripts should be defined.
   h. Figure 3·4 shows that amount of stainless steel in the lower plenum increases from 40 to 60 mt when the amount of $U0_2$ is increased from 60 to 80 mt, but this is not what is stated in the text on page 34.

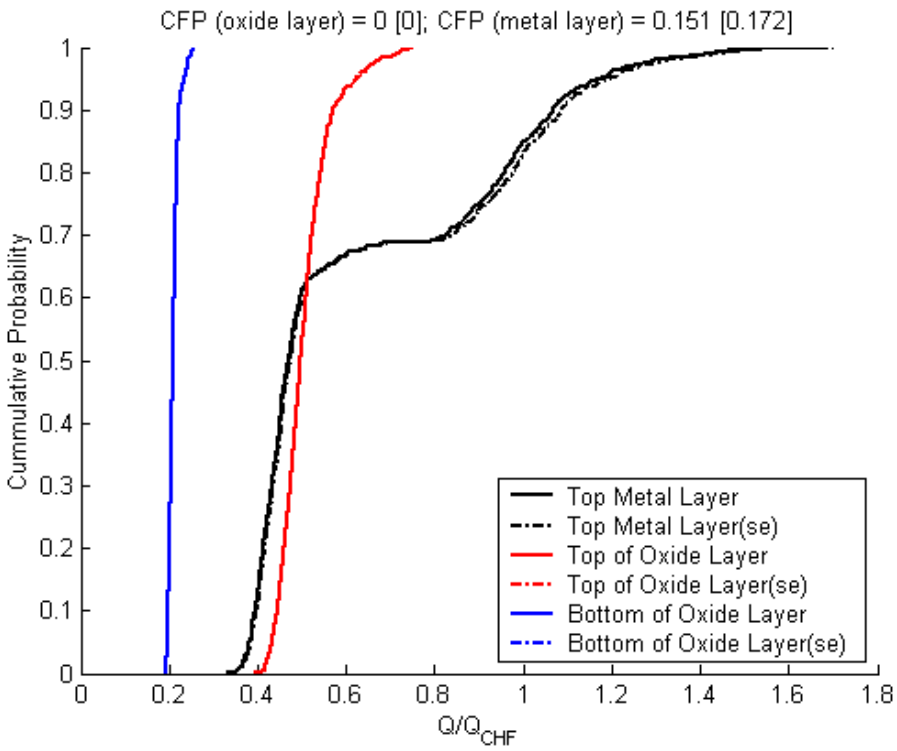

Figure B.6 Sensitivity to the Churchill and Chu correlation for base case without decay power in the metal layer

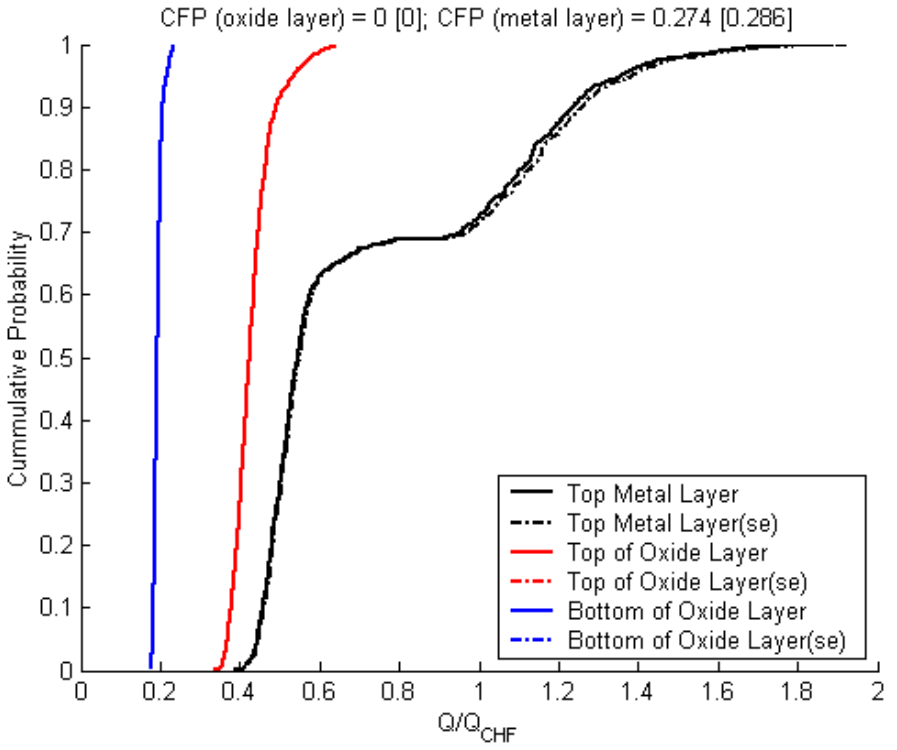

Figure B.7 Sensitivity to the Churchill and Chu correlation for base case with decay power in the metal layer

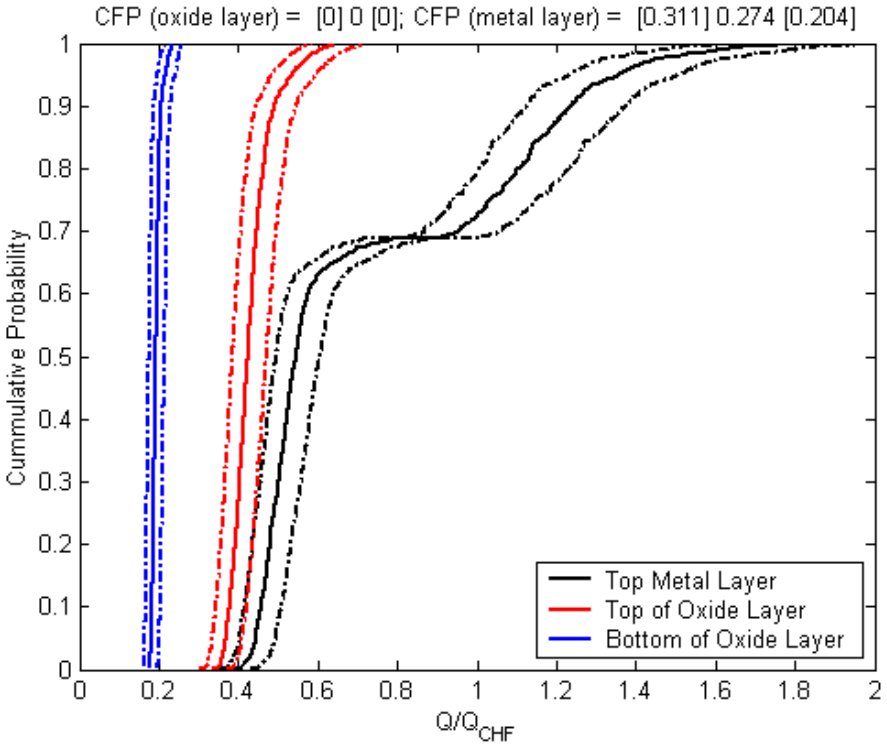

Figure B.8 Sensitivity to the uncertainties in the critical heat flux for the base case with decay power in the metal layer

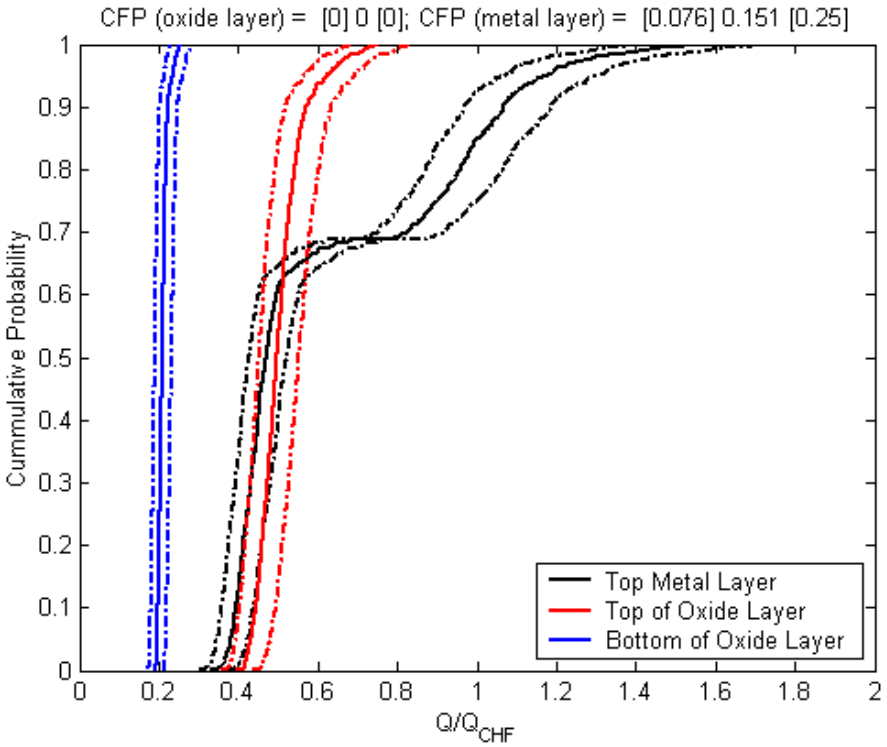

Figure B.9 Sensitivity to the uncertainties in the critical heat flux for the base case without decay power in the metal layer

ERI RESPONSE:

a. All plant-specific changes are taken into account for AP1000 in the report. These are explained in Section 3 where appropriate.

b. No attempt was made to perform SCDAP/RELAP calculations; however, a number of plant-specific MELCOR calculations were performed by ERI, and numerous MAAP calculations have been performed by Westinghouse as discussed in the report.

c. The time constant for the molten ceramic pool is of the order of minutes (~10 minutes).

d. Yes, the loss of volatile fission products is included.

e. System pressure has a first order effect during oxidation and core damage. It has a second order effect during the late phase melt progression because of the inherent uncertainties in the late phase melt progression. Calculations for other plants using MELCOR computer code have not shown any significant pressure-dependence on the prediction of in-vessel melt progression, other than some influence on the timing of key events and a small impact on Zr oxidation.

f. If the reviewer is referring to the FCI, the entire core mass would not mix with the water in the cavity. Following lower head failure, a limited amount of mass would be involved when the debris makes contact with the pool bottom.

g. Done.

h. This is clearly stated in the second paragraph.

4. Selected sensitivities and analysis results:

   a. Some basis for the mean values and standard deviation of the emissivities of metal and structure should be given.
   b. Amount of Zr for the case corresponding to Figure 4·4 is not given.
   c. If local heat flux in the light metal layer can be four to five times higher than the critical heat flux due to focusing effect, could this not lead to failure of the vessel lower head all along the boundary (circumferential failure).
   d. No discussion is given about the creep rupture failure of the vessel. Why is this possibility ignored?
   e. In the sensitivity analysis, what is the basis for the chosen size of the hole representing vessel failure?
   f. In the parametric calculations, on what basis is uranium mass fraction fixed at 0.4?
   g. It is not clear as to how mass of Zr in the bottom heavy layer was determined?
   h. In the parametric calculations, I would have liked to see the effect of variation of important thermophysical properties of the melt layers, the bounding crust and temperature of the structures in the vessel, on heat flux to water and thickness of crust.

ERI RESPONSE:

a. These are based on the DOE and INEEL analysis for AP600. The reference is now provided in the revised report.

b. This is added in the revised report.

c. This is exactly what is expected to take place, and the conditional lower head failure probability values that are estimated in the report, are based on this expectation. However, if the reviewer is referring to the FCI analyses, the available computer codes cannot permit the simulation of the consequential impact of this unzipping process.

d. Because of external cooling of the vessel wall, rupture is not possible as long as the critical heat flux is not exceeded. The same was true for AP600 [1].

e. The hole size are based on the thickness of the metal layer leading to lower head failure as explained in Section 5.3 of the report.

f. This is based on the peer review of AP600 analysis as outlined in the INEEL report.

g. It is given in Equation 4.4

h. The properties do not have a significant effect as shown in Table 4.2.

5. The calculated conditional probability associated with lower head failure (and location of failure):

   a. The calculated conditional probabilities seem reasonable; however, an example as to how the cumulative failure probability is calculated would have been helpful.

b. The calculated location of vessel failure is plausible, but other possibilities should be discussed, but may be ruled out because of their low probability.
c. It is difficult to discern as to how the size of the opening in the vessel was calculated. This will have a significant bearing on the propensity of subsequent FCI.
d. Uncertainty in the critical heat flux has not been propagated to obtain cumulative failure probability.

ERI RESPONSE:

a. The cumulative probability is calculated by sorting the result of the calculations for the 1000 samples.

b. We are not aware of other possibilities, other than failure at lower locations, and this has been considered by including an FCI sensitivity case that assumes lower head failure at the bottom location of the reactor pressure vessel.

c. The size of the opening was calculated based on the thickness of the metal layer that is required to exceed the critical heat flux as explained in Section 5.3 of the report.

d. *The actual CHF data has not been provided by Westinghouse; therefore, information is not available on the uncertainties in the measurement of critical heat flux. In response to the peer review comments, we have performed a sensitivity calculation that assumes ±10% variation in measured critical heat flux, and the results are shown in Figures B.8 and B.9. As indicated, the uncertainties in the critical heat flux can have a significant effect on the failure probability that can range from a maximum of 0.67 for the base case without decay power in the metal layer to a maximum of 0.26 for the base case with decay power in the metal layer.*

ASSESSMENT OF THE ADEQUACY AND TECHNICAL BASIS FOR OTHER AREAS:

1. Characterization of the initial conditions for ex-vessel fuel coolant interaction (FCI) analyses:

    a. The rate of ejection of molten material into the cavity is an important parameter. For a given driving head, the rate of ejection will depend on the size of the opening. For a shear cut along the vessel wall due to focusing effect, the ejection of all of the molten material into the vessel could occur very rapidly. This possibility has been excluded. It is not clear as to why.
    b. What is the basis for specification of pour velocity? Both acceleration due to gravity and driving head will determine the pour velocity.
    c. For bottom failure of the lower head, how was the failure size determined?

ERI RESPONSE:

a. We have considered a larger hole size as part of the sensitivity calculation. The results are consistent with those reported for AP600 [1]. The larger hole size is consistent with the upper bound of the distribution for the decay heat and the UO_2 mass as explained in Section 5.3 of the present report.

b. For the depressurized scenarios that are considered to be a relevant representation of core damage profile for AP1000, in the present analysis, only the gravity head is considered.

c. It is assumed to be the same as in the base case.

2. The approach/model used for mixing and the propagation of phases of ex-vessel FCI:

    a. The models for mixing and propagation of phases are documented elsewhere and it is not possible to critically evaluate the assumptions and approach used in developing the models. Also, it is outside of the scope of this work.
    b. The height of the computational domain in the vertical direction was chosen to be 2 meters in exercising PM-ALPHA. Since the melt release is calculated to occur at a height of 2 meters, water present in the cavity beyond 2 meters above the cavity floor should also be part of calculations of pressure pulse magnitude. It is stated that the calculations with PM-ALPHA are only performed to obtain conditions for ESPORSE, how are the fluid conditions obtained from one code transferred to the other?
    c. What dictated the choice of particle sizes of 0·01 and 0·1 m and fragmentation rates 4 kg/sec and 400 kg/sec?

ERI RESPONSE:

a. No Comment.

b. These are explained in the code manual. For the explosion calculations, there are basically six

distributions, namely (1) void fraction, (2) melt volume fraction, (3) melt temperature, (4) pressure, (5) water temperature, and (6) fraction of melt particles solidified.

c. *These were basically taken directly from the AP600 FCI analysis [1] where the TEXAS computer code was also used to obtain the particle breakup during the mixing process. The default fragmentation rate of 4 kg/s for 0.01 m particles was simply increased in direct proportion to the particle surface area.*

3. Selected parameter and sensitivities and the analysis results:

    a. Particle diameter and fragmentation rates and failure size have been varied. However, no calculations are performed by varying the liquid temperature in the cavity and pour velocity. Also, no information is given as to why the pour velocity in AP-1000 is lower than that for AP-600.
    b. How much mass of molten material interacts with water depends on hole size and jet velocity. To study the effect of internal pressure in the vessel, the jet velocity should have been varied parametrically.
    c. Why is the maximum pressure in the pool for AP-1000 (1000 MPa) higher than that for AP-600 (800 MPa), whereas for time periods between 1 and 3 ms the pressures are higher in AP-600? If it is the difference in thermal energy content of melt in the two cases, there is something hidden that I do not understand.
    d. It appears based on the experience with AP-600 that the maximum hole size is dictated by numerical instabilities rather than physical considerations.
    e. It is not clear as to why for the bottom failure of the vessel, pressure distribution in the pool at 1 ms and 2 ms is asymmetrical?

ERI RESPONSE:

a. There was no reason to parametrically vary the water temperature because the pool temperature was based on plant-specific MELCOR calculations. In addition, the pour velocity is based on the gravity head for the depressurized accident scenarios that are considered. The pour velocity is not expected to play a significant role, because for higher pour velocities, the melt reaches the cavity floor sooner. Therefore, as far as the total melt mass in the pool is considered, the results are not expected to be significantly impacted. We believe that the sensitivity to larger hole size adequately reflects the impact of higher melt mass.

b. Please see the previous response.

c. The nodal position of the maximum pressure in the pool varies as a function of time depending on the local conditions (melt volume fraction, void fraction, etc). In addition, the computational size was also slightly different between the two cases. However, most of the time the maximum pressure in the two cases are comparable.

d. No attempt was made to perform a calculation with a larger hole size. Our calculation for AP600 with a larger hole size of 0.8 m was not successful due to numerical problems. Our rationale for the choice of 0.4 m and 0.6 m hole sizes are explained in Section 5.3 of the report. The impulse loads for AP1000 calculations are consistently lower than AP600, and therefore, the AP600 results are bounding.

e. Usually to trigger the explosion, a trigger cell with high enough pressure is chosen. This is shown at the bottom of the pool at a distance of about 1 m. The asymmetry is due to the propagation of this initial pressure pulse. Otherwise, the explosion is rather benign.

4. The estimated loads and the resulting insights as related to AP-1000 containment integrity.

    a. Overall, the results appear to be reasonable.
    b. The conclusion that calculated loads for AP-1000 are less than those for AP-600 is a result of differences in base cases that have been used in the comparison. A discussion of what has led to the choice of different base cases would be enlightening.
    c. No consideration has been given to sequential pours, which are quite possible. Can it be stated safely that the results reported for a single pour case will be bounding for sequential pours?

ERI RESPONSE:

a. No Comment.

b. The differences are a combination of the design differences, plant-specific severe accident code calculations and the in-vessel retention analysis.

c. We do not understand what is meant by sequential pours. The duration of the FCI phenomena is less than 1 second that includes both the mixing phase and the explosion phase. A pour later in time is expected to behave in the same manner as long as the hole size, the pour velocity, etc. are similar.

APPENDIX C: RESPONSES TO ADDITIONAL PEER REVIEW COMMENTS

C.1 Additional Review Comments by Dr. F. Moody and ERI Responses

November 14, 2003

TO: Mohsen Khatib-Rahbar
Energy Research, Inc.
P. O. Box 2034
Rockville, MD 20847

FROM: F. J. Moody

SUBJECT: Review of ERI responses to peer review comments, "Analysis of In-Vessel Retention and Ex-Vessel Fuel Coolant Interaction for AP1000," ERI/NRC 03-202

I have reviewed the ERI responses to both my review comments, and comments of the other reviewers. The responses, in my opinion, fully address the questions, model suitability and applicability comments, and all possible concerns that were raised.

ERI has shown a marked degree of engineering depth, and also an openness to the responses of experts, that verifies underlying technical strength, and provides assurance concerning the overall path up to and including the conclusions reached in the study.

My comments mostly called attention to additional conservatisms that were already built into the study, requiring no further analysis unless marginal conclusions were reached. The ERI responses put these identified conservatisms into perspective.

Comments by the other reviewers led to several additional calculations, and the responses offered additional insights, strengthening the overall conclusions.

Yours truly,

Fred J. Moody
827 Larkspur Lane
Murphys, CA 95247
(209) 728-1616/1610 (phone/fax)
fmoody@goldrush.com

C.2 Additional Review Comments by Dr. M. Corradini and ERI Responses

NUCLEAR ENGINEERING and ENGINEERING PHYSICS
College of Engineering, University of Wisconsin, Madison
QuickTime™ a
GIF decompres
are needed to see this

Nuclear Engineering **Engineering Physics** **Engineering Mechanics** **Astrona**

November 14th, 2003

Dr. Moshen Khatib Rhabar
Energy Research, Inc.
P.O. Box 2034
Rockville, MD 20847

Dear Moshen,

I have reviewed the revised ERI report, ERI/NRC-03-202, entitled **Analysis of In-Vessel Retention and Ex-Vessel Fuel-Coolant Interactions for AP-1000.** In general, I found the report to be well written and quite comprehensive in providing a background to this technical issue. The report provides an excellent exposition for the analysis of the in-vessel retention and ex-vessel FCI explosion phenomena. I feel that you have incorporated my past comments adequately. I will be looking for open-literature data on CHF for various orientations.

Sincerely,

Michael Corradini

Michael Corradini, Chair
Wisconsin Distinguished Professor

C.3 Additional Review Comments by Dr. V. K. Dhir and ERI Responses

Adequacy of ERI Responses to Comments of Vijay K. Dhir

In general, the authors have given adequate responses to my comments and have appropriately revised the report ERI/NRC 03-202. However, a few deserve a better and/or more quantitative assessment and revisions by the authors. These are:

1. It is not appropriate to just state that Westinghouse did not provide an uncertainty band on CHF. This issue should have been raised with NRC in order to secure from Westinghouse a bound on uncertainty and variability. What is the basis for ±10% uncertainty? As acknowledged by the authors uncertainty in CHF can have marginal effect on probability of vessel failure.

2. In using Churchill and Chu correlation, a sensitivity calculation has been performed by arbitrarily increasing the heat transfer coefficient by 25%. The authors should note that in laminar natural convection heat transfer coefficient varies as negative ¼ power of distance from the leading edge. Theoretically, as one approaches the leading edge, the heat transfer coefficient goes to infinity?

3. Explanation with respect to the use of average temperature instead of maximum temperature in determining the heat transfer to the vessel wall appears to be circular. Energy to and from a layer is split three ways—top, bottom, and sideways. Each contribution needs to be evaluated in a consistent manner.

4. Mode size issue is still open. What happens if vessel fails all along the vessel circumference? Would the current results be bounding?

ERI Responses:

Note the following ERI responses correspond to the numerical order of Dr. Dhir's comments.

1. The ERI review of the AP1000 submittals has resulted in a number of Requests for Additional Information (RAIs), including one that specifically requested the CHF experimental data, including the uncertainties in CHF measurements. Since the initial peer review of the present report, the CHF data of Reference [28] for lower head configuration V has become available. Figure 2.2 shows the comparison of the correlation used in the present study (including an assumed ±10% variation shown as the dotted lines) and the experimental data. There is no discussion in Reference [28] regarding the uncertainties in the measured data.

2. Under laminar flow regime conditions, the heat transfer coefficient varies as negative ¼ power of distance from the leading edge of a flat plate and theoretically, as one approaches the leading edge, the heat transfer coefficient goes to infinity as stated by the reviewer. However, the present analysis uses an average heat transfer correlation for the entire surface rather than local values. Therefore, assuming constant properties, the local heat transfer can be integrated over the entire length of the plate with the result that the average heat transfer correlation is 4/3 of the heat transfer correlation for the entire plate. For turbulent flow regime, the heat transfer coefficient (not the Nusselt number) is constant because typically, the Nusselt number correlates with Rayleigh number to 1/3 power. The Churchill and Chu correlation includes contributions from both turbulent and laminar regimes for $Ra_L > 10^9$. In addition, because of the enclosed geometry of the present problem, a singularity at the leading edge as predicted theoretically, is not envisioned. Nevertheless, a series of sensitivity calculations are performed to examine the effect of the heat transfer enhancement to the sidewall in the metal layer (Churchill and Chu correlation).

Increase in Metal Layer Sidewall Heat Transfer	Metal Layer CFP	Metal Layer CFP (Without Decay Heat)
0%	0.27	0.15
25%	0.28	0.17
50%	0.29	0.18
75%	0.29	0.19
100%	0.30	0.20
150%	0.30	0.22
200%	0.31	0.23

For the case with decay heat in the metal layer, there is a 12% increase in CFP for a two-fold increase in the heat transfer coefficient based on the Churchill-Chu correlation, while there is 50% increase in CFP for the case without the decay heat in the metal layer. Ultimately, the heat transfer to the sidewall is controlled by the resistance to heat transfer from the top surface of the ceramic pool and the decay heat in the metal layer. These results are well within the uncertainties considered in Table 7.1.

3. For the molten ceramic pool, the pool temperature is now defined as the maximum pool temperature. The molten ceramic pool is bounded by a crust that is at the melting temperature of the ceramic pool. The energy balance yields the melt superheat, which is the difference between the maximum temperature in the pool and the melting temperature. Therefore, the definition of the melt superheat in the ceramic pool is consistent with the definition of the heat transfer correlations to the top and bottom surfaces of the ceramic pool. Note that this is just a matter of definition, and will not affect the results of the analysis at all. For the top metal layer, the heat transfer correlations are based on the bulk temperature, and the formulation of the energy balance is consistent with the definition of the heat transfer correlation as discussed in Section 2.

4. Circumferential failure and a total unzipping of the lower head will lead to a "fall" of the entire hemispherical part of the lower head including its molten debris content into the reactor cavity, thereby displacing most of the water from the lower cavity region. When the lower head drops directly into the cavity, then FCI can be postulated to occur via a stratified contact mode that severely limits the formation of a fuel-coolant pre-mixture and the steam explosion would be benign as observed experimentally [41-42]. Therefore, the current results are considered as bounding.

APPENDIX D: USER'S MANUAL FOR THE ERI IVR ANALYSIS MODULE

D.1 Description of the Graphical User Interface (GUI)

This appendix provides a user manual for the ERI IVR Analysis Module (ERI-IVRAM) GUI. This program was used to perform the IVR calculations in the main body of the report.

The modifications of the user-specified problem geometry, heat transfer correlations, etc. are easily accessible to the user through a number of control boxes as shown in Figure D.1. The main window is divided into 7 tabs that include the cavity, the vessel, heat transfer parameters, debris mass, material properties, decay heat, and the statistical properties.

At the bottom of the main window, there are 5 control buttons. A description of the control buttons is given below.

Load IVR Input File – This is used to load a previously saved input file. The input files have the extension "ivr".

Save IVR Input File – This is used to save the input file after changes are made to the input parameters. The input files have the extension "ivr".

Start IVR Calculation – This is used to start the IVR calculation. After the calculation is done, a message box appears indicating the end of the end calculation and the main window appears again.

Plot IVR Results – Clicking this button launches the plot module.

Cancel – Clicking this button exits the program.

A description of the various windows is provided in the following subsections.

D.1.1 Cavity

The cavity conditions are changed in this window as shown in Figure D.1. There are basically two variables that need to be specified, the cavity water temperature, and the polynomial representing the critical heat flux a function of the angular position (θ) along the vessel lower head (see Equation 2.29 in the main body of the report). A six-degree polynomial can be specified.

D.1.2 Vessel

This tab provides information regarding the vessel parameters as shown in Figure D.2, including the core Zr inventory, and the total structure area that is used to model radiation heat transfer from the top of the molten metal layer. The lower head thermal conductivity and the structure area shown here are used for the point estimate calculation. In the uncertainty calculation, uncertainty distributions can be used for these two parameters.

D.1.3 Heat Transfer Parameters

Figure D.3 provides the heat transfer parameters window. The heat transfer correlations are expressed in terms of the Nusselt Number (Nu), the Rayleigh number (Ra), the Prandtl number, and the pool height ratio (H/R) as explained in Table 2.1 in the main body of the report. In addition to the heat transfer correlations, the angular variation of the heat transfer correlation can also be specified. The Park correlation is specified in Table 2.1, and the UCSB correlation is the same as mini-ACOPO correlation in Table 2.1. A third option [17] can also be specified by the user that is of the form:

$$\frac{h_d(\theta)}{\overline{h_d}} = \left[-1.25\cos\theta_{tot} + 2.6\right]\sin\theta - \left[-2.65\cos\theta_{tot} + 3.6\right]\cos\theta;\quad 0.75 < \frac{\theta}{\theta_{tot}} \le 1$$

$$\frac{h_d(\theta)}{\overline{h_d}} = 1.17\sin^4\theta + 0.23;\quad 0 < \frac{\theta}{\theta_{tot}} \le 0.75 \qquad \text{(D.1)}$$

D.1.4 Debris Mass

Figure D.4 shows the debris mass window. The user should provide the point estimate masses for the ceramic pool (UO_2 and ZrO_2) and the metal layer (Zr and Steel) in the left frame. The right frame contains the dependence of the Steel on UO_2 for the uncertainty calculation. This table contains 6 entries and all should be filled.

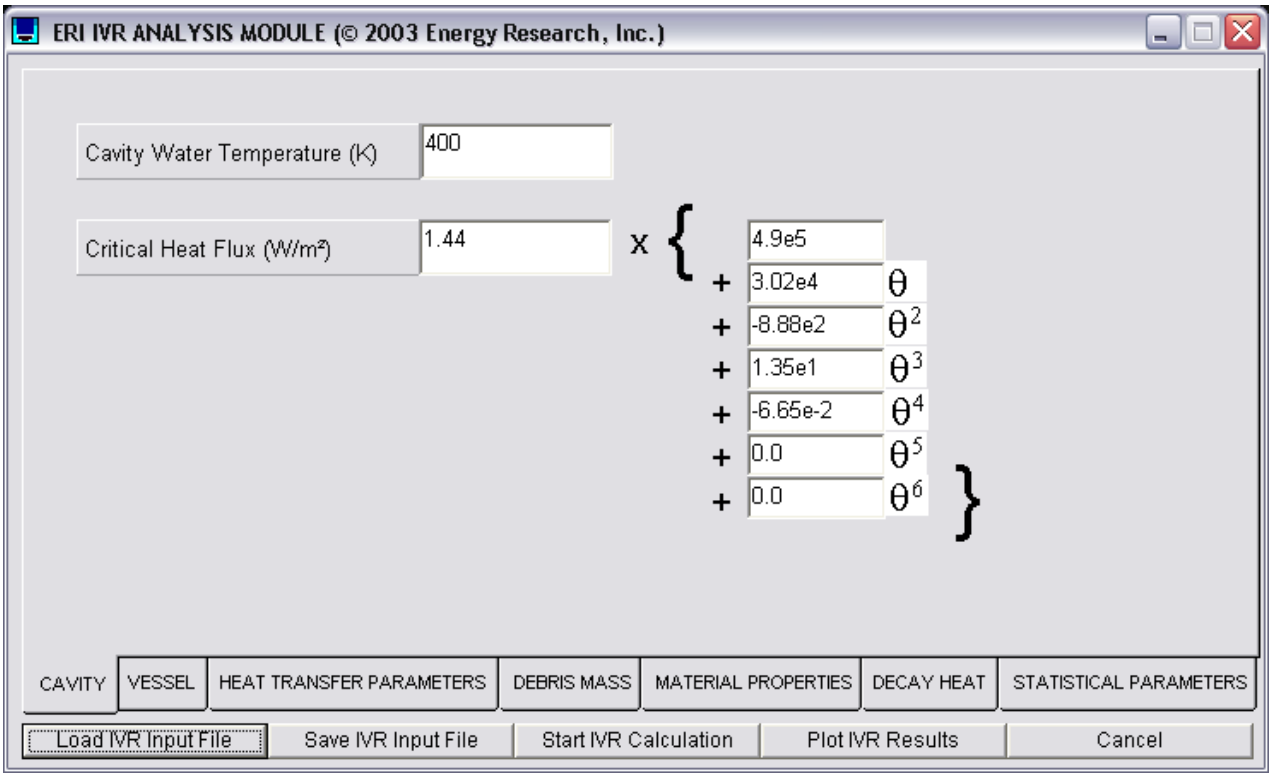

Figure D.1 ERI IVR analysis module main window

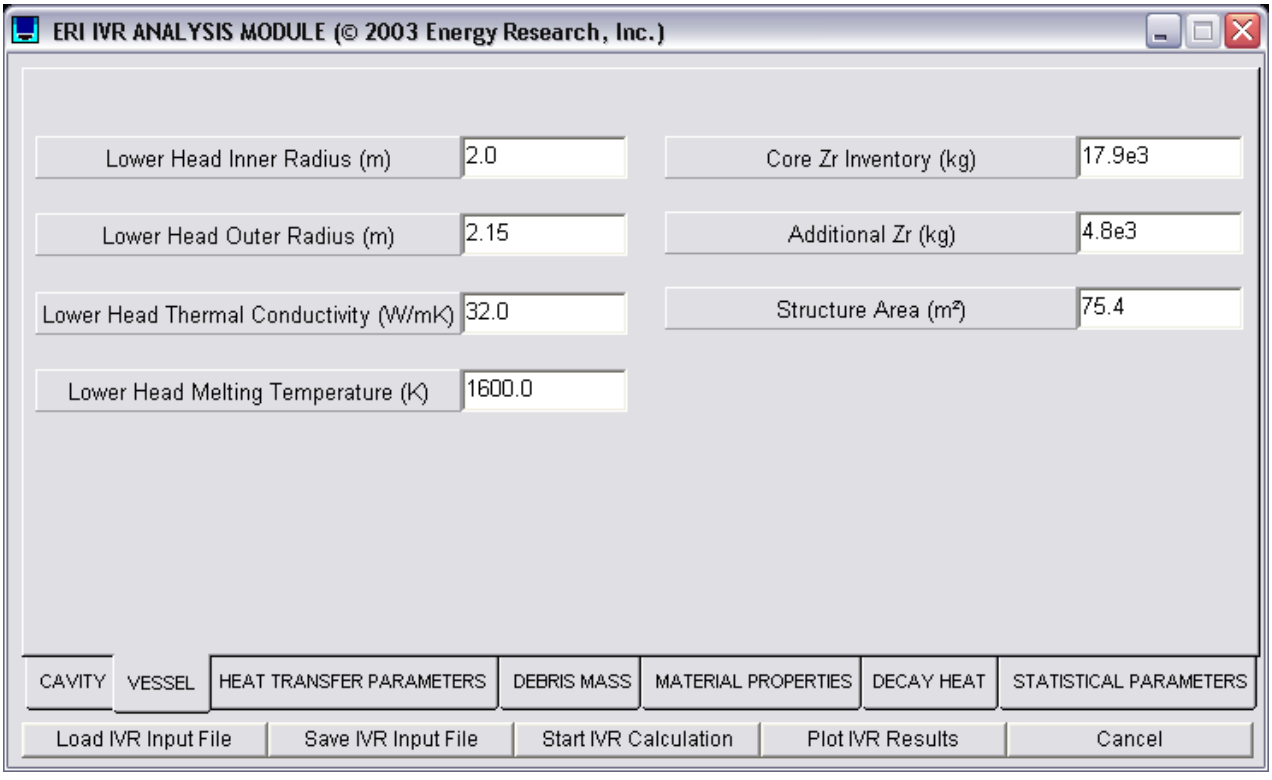

Figure D.2 Vessel parameters window

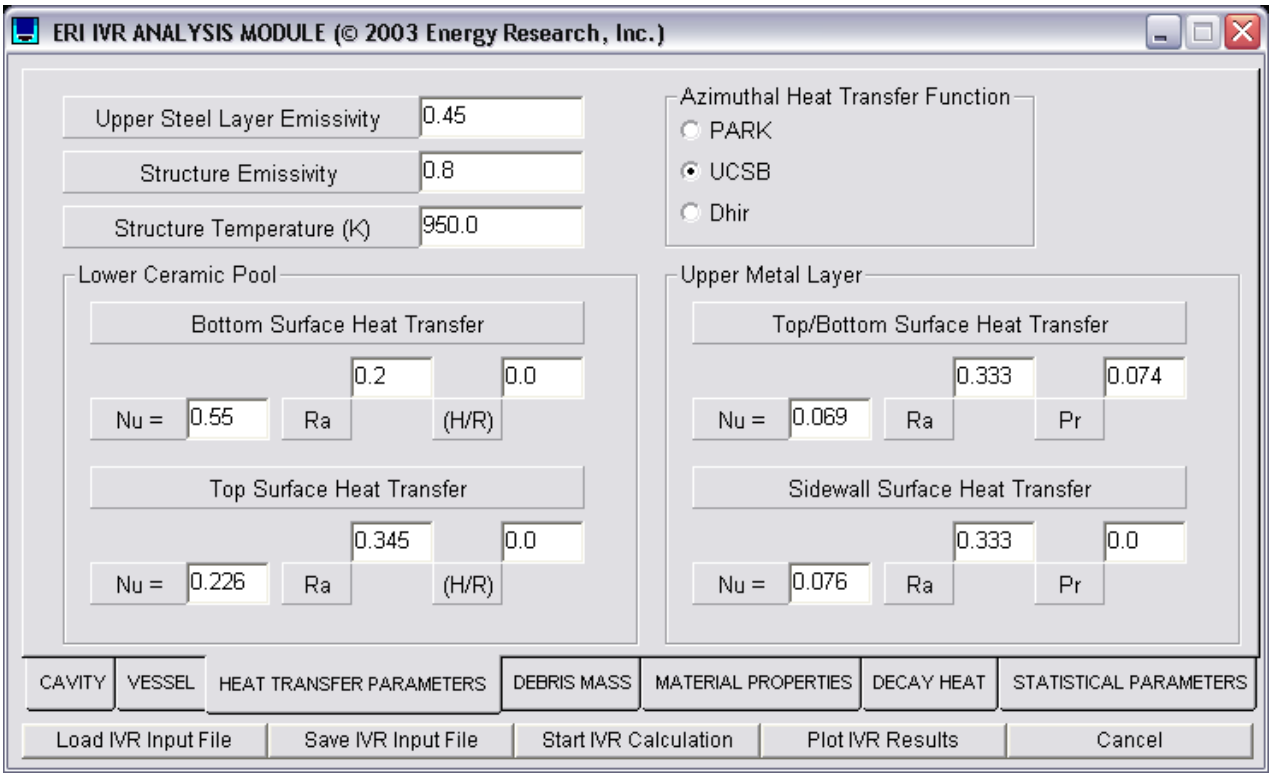

Figure D.3 Heat transfer parameters window

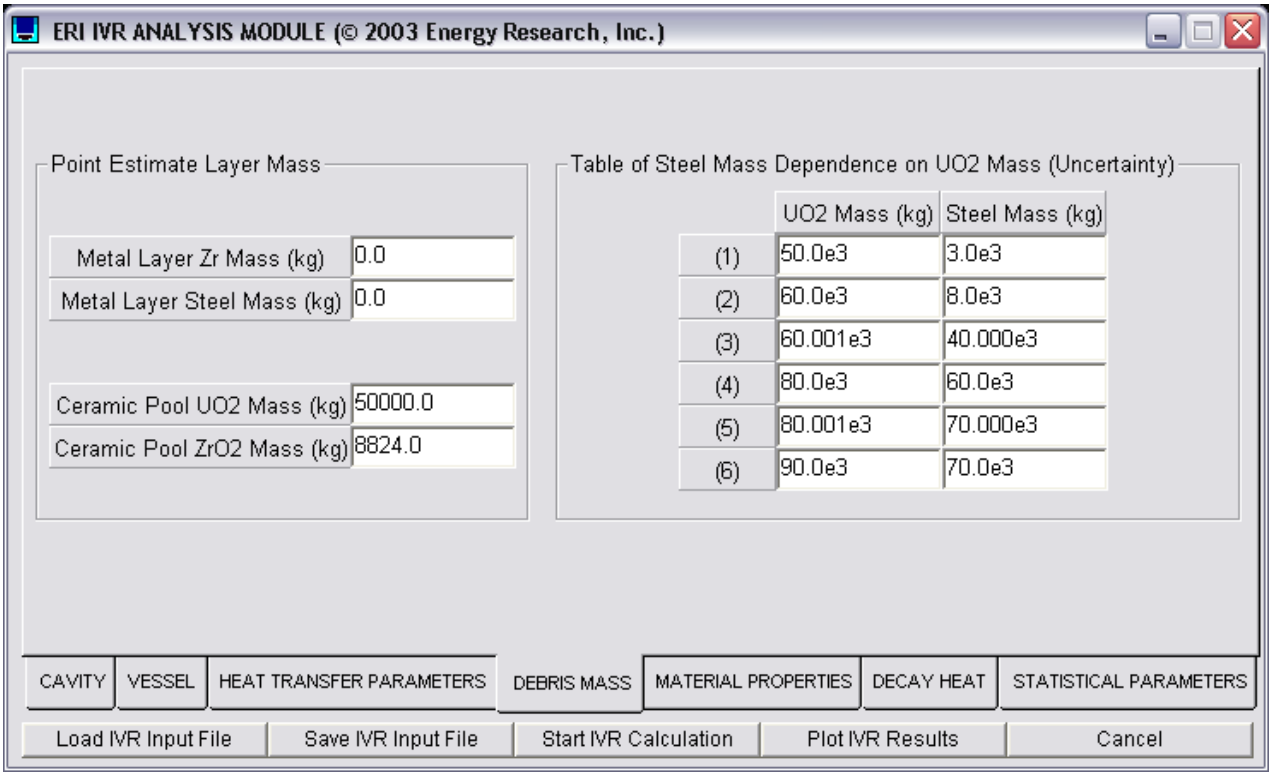

Figure D.4 Debris mass parameters window

D.1.5 Material Properties

The material properties window (Figure D.5) requires ceramic pool melting temperature, lower and upper crust thermal conductivities, and viscosities. These 5 values are point estimate. The point estimate material properties including thermal conductivity, specific heat, density, and coefficient of thermal expansion for UO_2, ZrO_2, U, Steel and Zr are provided in the bottom of the window. Note that the material properties of U are not currently used in the program because the layers do not contain U. Uncertainty distributions can also be associated with these material properties.

D.1.6 Decay Heat

The decay heat window only contains two variables as shown in Figure D.6. If the metal layer decay heat fraction is greater than 0 and is less than 1, then this fraction of decay heat is subtracted from the ceramic pool and is deposited in the upper metal layer. The time of release is required to calculate to total decay heat from the file "ivr.pwr".

D.1.7 Statistical Parameters

There are basically two modes of calculations, uncertainty calculation (Figure D.7), and point estimate calculation (Figure D.8). In the point estimate calculation, the user specifies the input parameters such as debris mass, decay heat, etc., and the code calculates the results as a function of the angular position. In the uncertainty calculation, the results are presented as a function of the cumulative probability.

For the uncertainty calculation, the user can specify the uncertainty distributions for each variable by clicking on the variable label. Four types of uncertainty distributions including normal, uniform, lognormal, and piecewise uniform can be specified. For the first three distributions, the lower and upper bounds of the distribution should be specified (see Figure D.9). For the piecewise uniform distribution, the number of intervals and the number of samples for each range should be specified (see Figure D.10). Once changes are made to the uncertainty distributions, the user can save the file and generate the samples. The user can also have the option of loading a previously saved file. The number of samples and the sample seed can be changed in any of the windows (Figures D.9 and D.10).

D.2 Management of Data Files and User Specifications

ERI-IVRAM uses a number of data files, and some records in these data files can be modified by the user as described below.

'ivr.pwr'

This file contains the table of core power as a function of time since the initiation of the accident. The value in the first row should always be 1. There are three values in the second row. The first record is the number of entries in the table of the decay heat as a function of time to be listed from the third row. The second record is the total mass of UO_2 in the core, and the third record is the decay heat multiplication factor. From the third row on, the first column is the time in seconds, the second column is the fraction of reactor thermal power after shutdown, and the third column is the multiplying factor (e.g., to account for loss of volatiles).

This file is used only for the point estimate calculation. The time of release (see Figure D.6) is used to calculate the interpolated value of the total decay heat.

'muplot.def'

This file contains the labels and setpoints for the plot module. The first column is the long label for the curve (if the number of curves is less than 4), and the 5^{th} column is for the short legend for the curves (if more than 4). The second and third columns are reserved for the Ymin and Ymax for each curve (if these fields are left empty, ERI-IVRAM scales the graph automatically). The fourth column is not currently used, but represents the order of the output data. The records in this file may be modified by the user, but the placement of the columns separated by vertical bars cannot be changed.

'ivr.grf'

This file contains the results of the calculation that are displayed using the ERI-IVRAM plot module. However, the user can also use this file to plot the results with any other plotting package. Tables D.1 and D.2 show the location of the variables for the uncertainty and point estimate calculations.

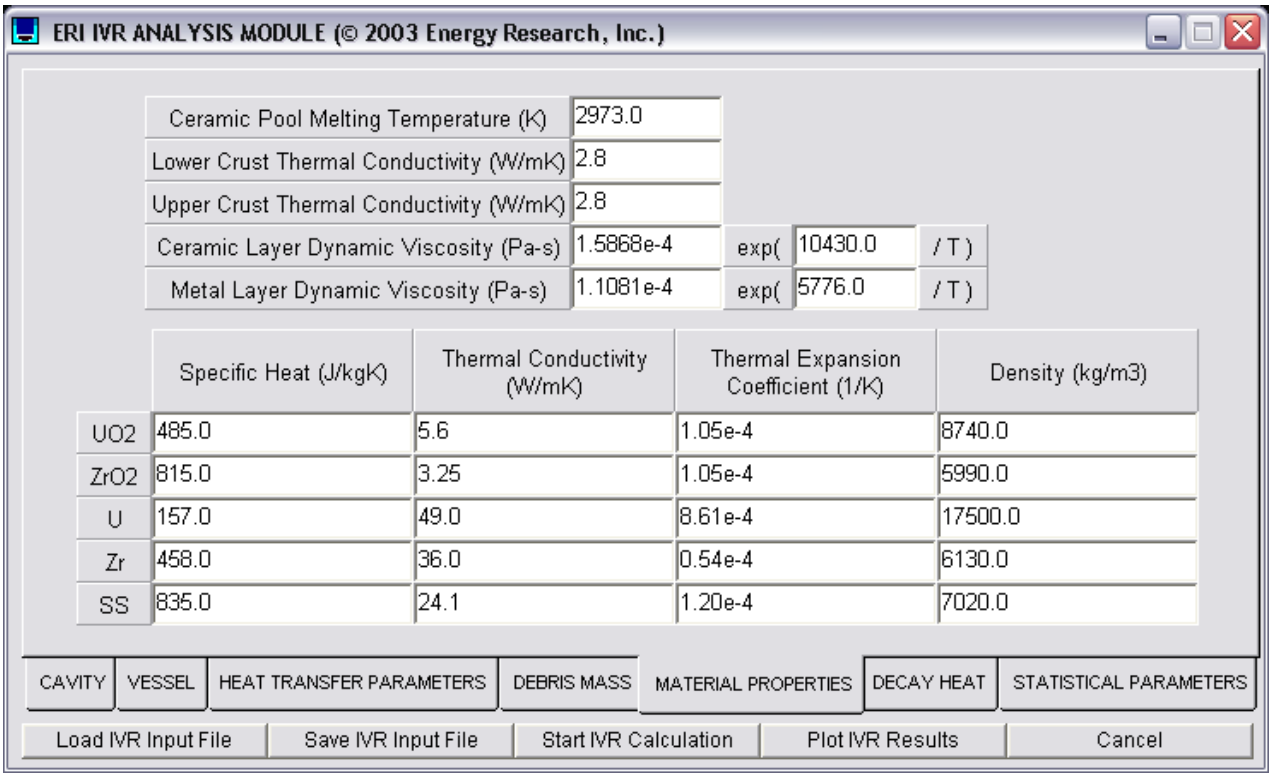

Figure D.5 Material properties parameters window

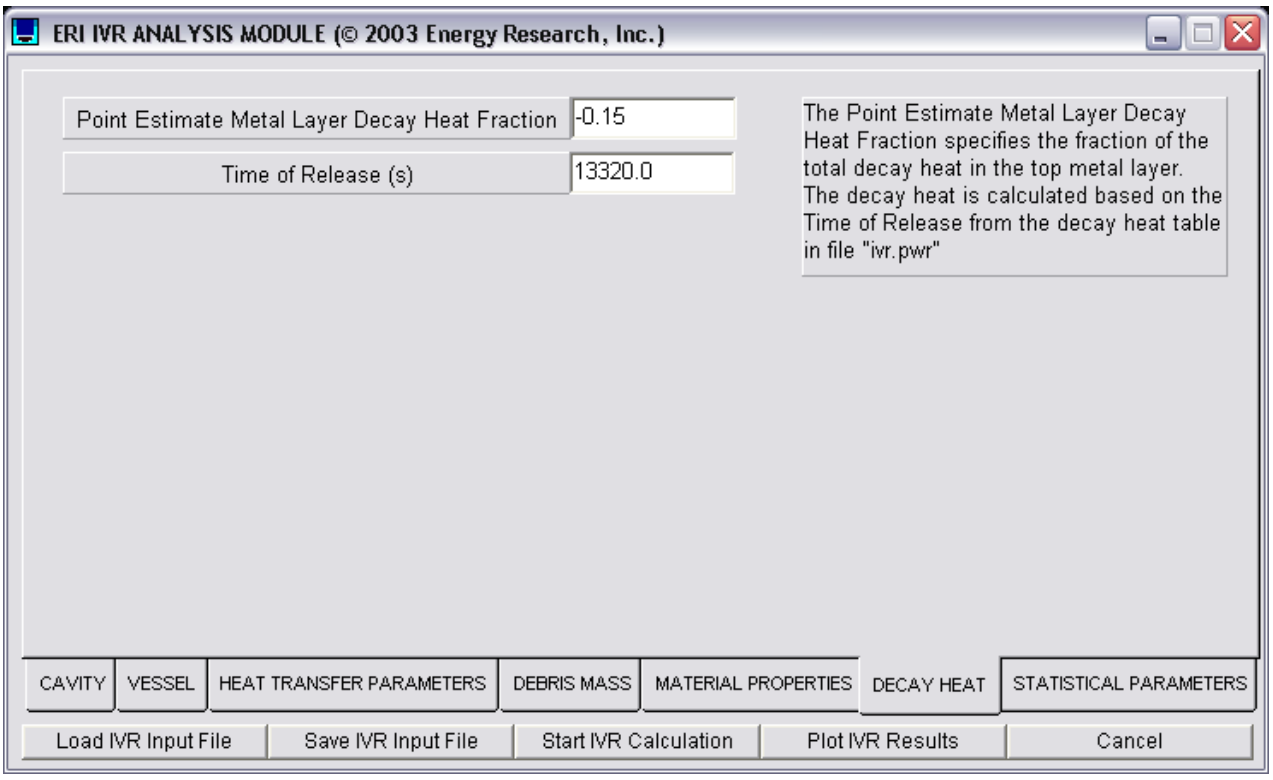

Figure D.6 Decay heat window

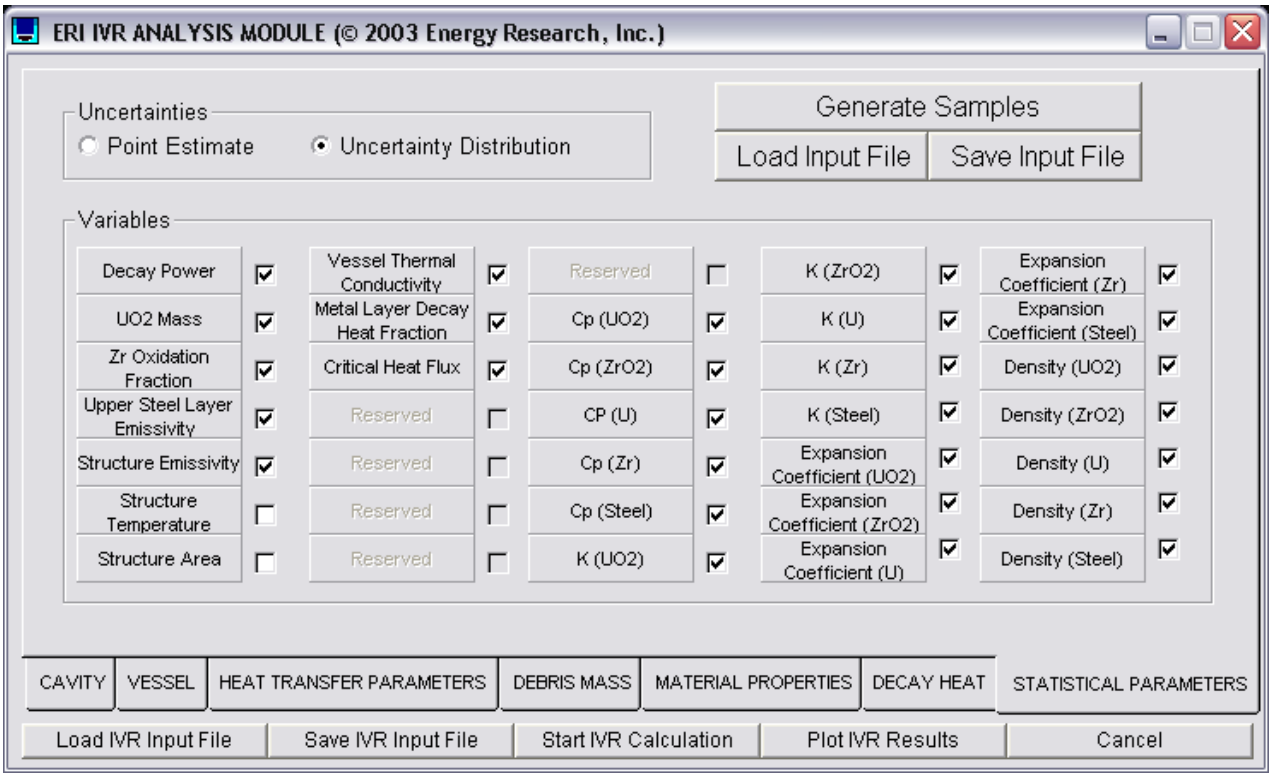

Figure D.7 Statistical parameters window for uncertainty calculation

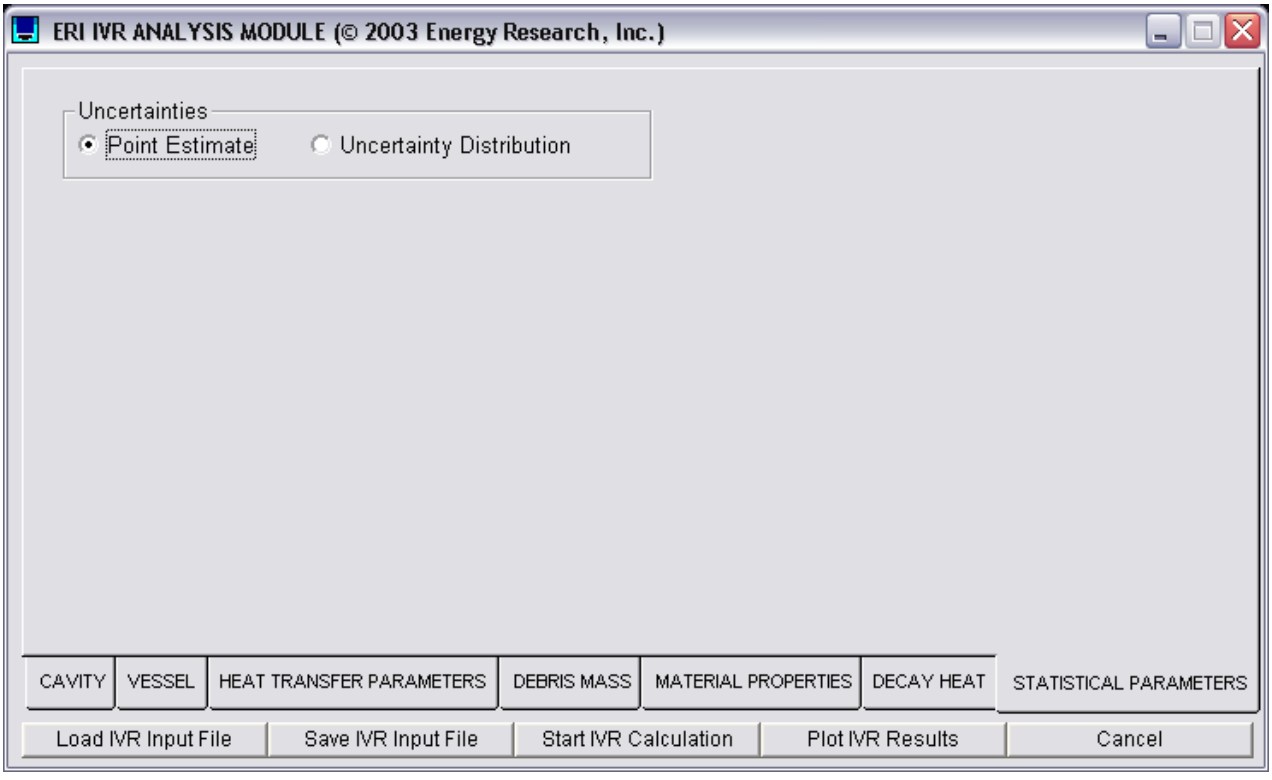

Figure D.8 Statistical parameters window for point estimate calculation

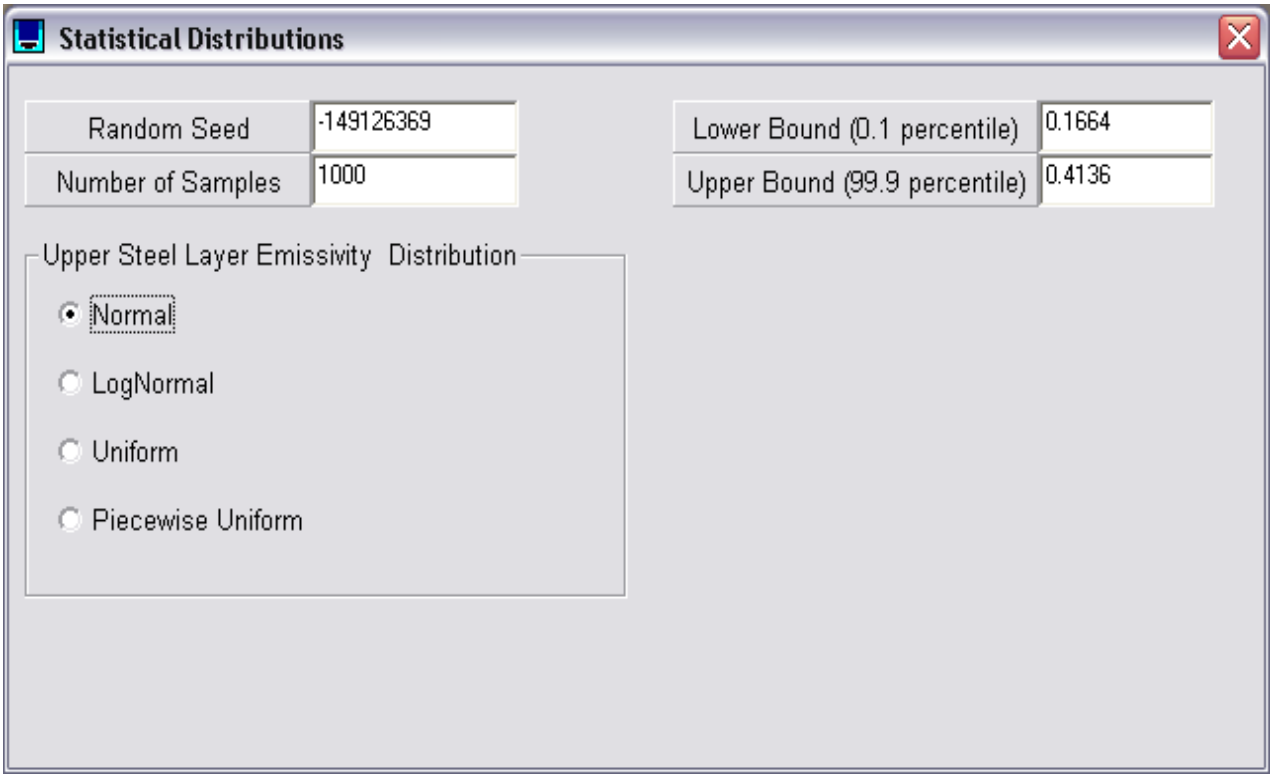

Figure D.9 Statistical distributions window for normal distribution

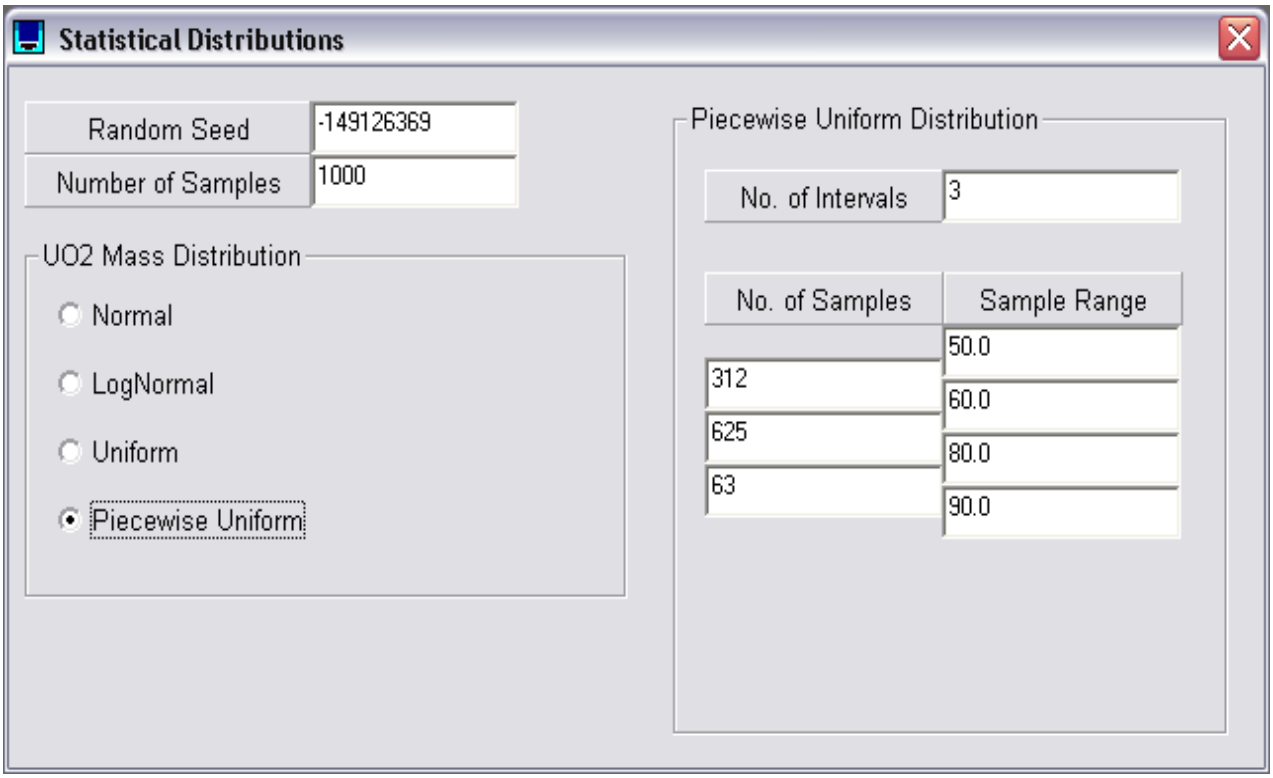

Figure D.10 Statistical distributions window for piecewise uniform distribution

Table D.1 List of ERI-IVRAM output variables for the uncertainty calculation

Variable	Column
Cumulative Probability	1
Twi (Bottom of Ceramic Pool) [K]	2
Two (Bottom of Ceramic Pool) [K]	3
Twi (Top of Ceramic Pool) [K]	4
Two (Top of Ceramic Pool) [K]	5
Twi (Metal Layer) [K]	6
Two (Metal Layer) [K]	7
Water Heat Flux (Bottom of Ceramic Pool) [MW/ m^2]	8
Water Heat Flux (Top of Ceramic Pool) [MW/ m^2]	9
Water Heat Flux (Metal Layer) [MW/ m^2]	10
Heat Flux Ratio (Bottom of Ceramic Pool)	11
Heat Flux Ratio (Top of Ceramic Pool)	12
Heat Flux Ratio (Metal Layer)	13
Lower Crust Thickness (Bottom of Ceramic Pool) [cm]	14
Lower Crust Thickness (Top of Ceramic Pool) [cm]	15
Lower Crust Thickness (Metal Layer) [cm]	16
Upper Crust Thickness [cm]	17
Lower Head Thickness (Bottom of Ceramic Pool) [cm]	18
Lower Head Thickness (Top of Ceramic Pool) [cm]	19
Lower Head Thickness (Metal Layer) [cm]	20
Corium Pool Superheat [K]	21
Corium Pool Heat Generation [MW]	22
Corium Pool Heat Generation Density [MW/ m^3]	23
Metal Layer Heat Generation [MW]	24
Metal Layer Heat Generation Density [MW/ m^3]	25
Corium Pool Azimuthal Angle [°]	26
Metal Pool Azimuthal Angle [°]	27
Corium Pool Height [m]	28
Metal Layer Height [m]	29
Total Decay Heat [MW]	30
UO2 Mass [mt]	31
ZrO2 Mass [mt]	32
Zr Mass [mt]	33
SS Mass [mt]	34
Critical Heat Flux (Bottom of Ceramic Pool) [MW/ m^2]	35
Critical Heat Flux (Top of Ceramic Pool) [MW/ m^2]	36
Critical Heat Flux (Metal Layer) [MW/ m^2]	37

Table D.2 List of ERI-IVRAM output variables for the point estimate calculation

Variable	Column
Lower Head Angle [°]	1
Twi [K]	2
Two [K]	3
Lower Crust Thickness [cm]	4
Upper Crust Thickness [cm]	5
Corium Pool Superheat [K]	6
Water Heat Flux [MW/m^2]	7
Heat Flux Ratio	8
Lower Head Thickness [cm]	9
Corium Pool Height [m]	10
Metal Layer Height [m]	11
Corium Pool Heat Generation [MW]	12
Corium Pool Heat Generation Density [MW/ m^3]	13
Metal Layer Heat Generation [MW]	14
Metal Layer Heat Generation Density [MW/m^3]	15

D.3 User Guidelines

In general, the ERI-IVRAM controls are simple to use and self-explanatory. However, in this section, a number of user guidelines are provided to assist the user in better utilization of the ERI-IVRAM controls and capabilities.

D.3.1 General

- For the uncertainty calculation, a distribution for a critical heat flux multiplication factor is specified. The leading 1.44 multiplication factor in the CHF correlation (shown in Figure D.1) is then multiplied by the sample value. For example, to represent a 10% uncertainty in the critical heat flux, a normal distribution with a lower bound of 0.9 and the upper bound of 1.1 can be used to generate the samples.

- For the normal distribution, uniform distribution, and the lognormal distribution, the lower and upper bounds are at 0.1 percentile and 99.9 percentile. If the mean and the standard deviation are known, they can be used to calculate the lower and upper bounds of the distribution.

- For the piecewise uniform distribution, the program requires the number of samples in each range. The total number of samples in each range should be equal to the total number of samples. The code automatically adjusts the number of samples in each range so that the total is equal to the number of samples. Therefore, the user can choose relative probability levels (e.g., 1, 0.1, etc.) for each range.

- Only the total decay heat is specified in both the point estimate and the uncertainty distributions. The decay heat in the ceramic pool is calculated as the ratio of the mass of UO_2 in the ceramic pool and the total core UO_2 inventory. The total core UO_2 inventory is specified in 'ivr.pwr' file.

- For all variables with uncertainty distributions (except the decay power), if the check box in Figure D.7 is not checked, the program uses the point estimate values. For example, if the check box for the UO_2 mass is left unchecked, the program uses the point estimate value from Figure D.4. The decay power distribution must always be specified (the check box must always be checked).

- The number of samples (limited to 5000), and the random seed are visible for all uncertainty distributions. These two variables can be changed using any of the uncertainty distributions windows (Figures D.9 and D.10).

- To change the number of intervals for the piecewise uniform distribution (Figure D.10), the user should **mark** the integer in the text box (with the mouse) and enter the new value. The minimum and maximum values are 2 and 6, respectively. The backspace and delete keys cannot be used to change the value.

D.3.2 Plot Module

1. The following are guidelines for the use of multi-plotting option that is activated by clicking on the "Plot IVR Results" button in the main window.

2. The user should **not** use the large font. In some cases, the large font along with the option for monochrome+symbol may lead to crash of the multi-plot module (this does not affect the main module). In this case, the user should simply delete the file "eriivr-plot.on" from the application directory where ERI-IVRAM is installed and restart the plot module.

3. Clicking on the right mouse button allows additional plot options. A help file is also available for these options. A comparison plot refers to the curve whose y-axis is shown on the right hand side. The numeric precision is only used for the table display of data on the bottom of the plot (by choosing Graph and/or Table option), and it does not affect the display of the y-axis.

4. It is strongly recommended to limit the number of curves to 4 (the plot legends are abbreviated for more than 4 curves).

5. In the "Plot Options" window, the list of plot variables is displayed. Checking the Min/Max button allows the user to manually modify the minimum and maximum y-axis values shown in the boxes (otherwise, they are automatically calculated). However, adding and removing curves to the plot list changes the order of the plots, and therefore, the manual modification of the minimum and maximum values should be set again.

6. For the uncertainty distribution, if only a single parameter is used, the y-axis is the cumulative probability. For more than one parameter, the x-axis is the cumulative probability in order to allow for comparison plots.

7. The program automatically calculates the probabilities of exceeding the critical heat flux in the metal layer and in the ceramic layer.

D.3.3 Program Installation

The program can be installed by double-clicking on the executable file "ERIIVR1.0.exe" found on the installation CD. The installation requires at least 2MB on the hard disk, and a Pentium™* processor. The following window appears, and the user should follow the instructions to install the program. The program should install easily on Windows-98™*, Windows-2000™*, and Windows-XP™*. Depending on the windows service pack update on individual computers, the user may get a warning that certain files cannot be installed. In this situation, the user should choose the "ignore" button option.

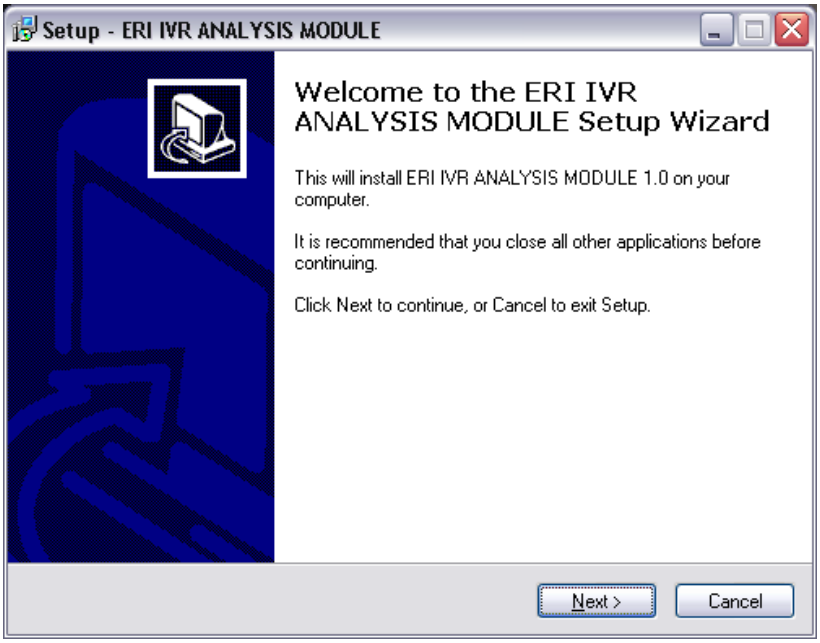

Figure D.11 ERI-IVRAM installation setup window

* Trademark of Microsoft Corporation.

NRC FORM 335 (2-89) NRCM 1102, 3201, 3202

U.S. NUCLEAR REGULATORY COMMISSION

BIBLIOGRAPHIC DATA SHEET

(See instructions on the reverse)

1. REPORT NUMBER (Assigned by NRC, Add Vol., Supp., Rev., and Addendum Numbers, If any.)

NUREG/CR-6849
ERI/NRC 04-201

2. TITLE AND SUBTITLE

Analysis of In-Vessel Retention and Ex-Vessel Fuel Coolant Interaction for AP1000

3. DATE REPORT PUBLISHED

MONTH: August | YEAR: 2004

4. FIN OR GRANT NUMBER

Y6696

5. AUTHOR(S)

Hossein Esmaili and Mohsen Khatib-Rahbar

6. TYPE OF REPORT

Technical

7. PERIOD COVERED *(Inclusive Dates)*

8. PERFORMING ORGANIZATION - NAME AND ADDRESS *(If NRC, provide Division, Office or Region, U.S. Nuclear Regulatory Commission, and mailing address; if contractor, provide name and mailing address.)*

Energy Research, Inc.
P. O. Box 2034
Rockville, Maryland 20847-2034

9. SPONSORING ORGANIZATION - NAME AND ADDRESS *(If NRC, type "Same as above"; if contractor, provide NRC Division, Office or Region, U.S. Nuclear Regulatory Commission, and mailing address.)*

Division of Systems Analysis and Regulatory Effectiveness
Office of Nuclear Regulatory Research
United States Nuclear Regulatory Commission
Washington, D.C. 20555-0001

10. SUPPLEMENTARY NOTES

S. Basu, NRC Project Manager

11. ABSTRACT *(200 words or less)*

The present study assesses the likelihood and potential location of the reactor pressure vessel lower head failure following low-pressure severe accident scenarios in AP1000, and subsequently, the energetics of ex-vessel fuel coolant interaction. The approach consists of the specification of initial conditions; determination of the mode, the size and the location of lower head failure based on heat transfer analyses; computer simulation of the fuel coolant interaction processes; and finally, an examination of the impact of the uncertainties in the initial conditions and the model parameters on the fuel coolant interaction energetics through a series of sensitivity calculations. The thermal analysis of lower head shows that the lower head failure probability at the side of the vessel due to the focusing effect of the thin stratified metal layer overlying the ceramic pool ranges from ~0.04 to ~0.30, depending on the uncertainties in late phase melt progression and the modeling parameters. On the other hand, the failure of the lower head due to thermal attack at the bottom location is assessed to be highly unlikely. Furthermore, two-dimensional ex-vessel fuel coolant interaction analyses show that the calculated impulse loads (and maximum pressures) for AP1000 remain below those that were estimated for AP600 using similar methods.

12. KEY WORDS/DESCRIPTORS *(List words or phrases that will assist researchers in locating the report.)*

Severe Accident Uncertainties
In-Vessel Retention
Molten Pool Phenomena
Lower Head Failure
Ex-Vessel Cooling
Ex-Vessel Fuel Coolant Interaction

13. AVAILABILITY STATEMENT

unlimited

14. SECURITY CLASSIFICATION

(This Page) unclassified

(This Report) unclassified

15. NUMBER OF PAGES

16. PRICE

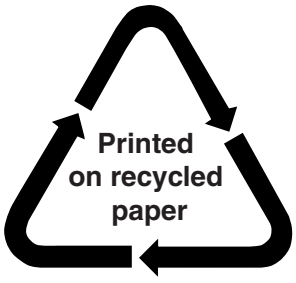

Federal Recycling Program